GaAs Radiation Detectors

Valentine O'Shea

Faculty of Engineering

University of Glasgow

Thesis submitted for the degree of Doctor of Philosophy

May 1998

ProQuest LLC.
789 East Eisenhower Parkway
P.O. Box 1346
Ann Arbor, MI 48106 – 1346

Abstract

This thesis presents the results obtained with radiation detectors made with Schottky barrier contacts to GaAs. Three types of detectors are investigated, namely pads, microstrips and pixellated detectors on both semi-insulating un-doped material as well as on epitaxial material. Tests, devised and carried out by the author, which use a variety of radiation sources to characterise the devices are described.

Read out electronics used in conjunction with these detectors are described as well as the tests performed in high energy particle beams at CERN, the European Centre for Nuclear Research. Irradiations of the detectors have also been carried out at CERN, in the Rutherford Laboratory and at a commercial site in France to measure the "radiation hardness" of these detectors. Their suitability for use in the High Energy Physics environment has not been proven due to the progress made in increasing the resistance of detectors made from silicon to the high radiation dose.

Initial work on pixellated detectors for HEP applications has turned to the field of X-ray imaging as a natural alternative where GaAs has much to offer. Measurements have been done to evaluate the imaging capabilities of GaAs detectors using read out electronics developed for HEP. A 320 X 240 array of bump bonded pixels each 38 μm square has been tested using a charge integrating readout with results indicating a performance of better than 10 line pairs per mm.

Epitaxially grown material has been investigated and shown to perform well as a detection medium. The purest material that has been tested still has a free carrier concentration that is at least an order of magnitude too high.

An initial investigation into a novel photonic detector read out scheme is presented. The idea involves the use of reflective optical modulators to readout the charge from the detector element. A modulator was designed and successfully tested in order to demonstrate that this is possible. The integrated detector/modulator did not perform as hoped and alternative directions have been suggested.

Preface

The development of GaAs radiation detectors has been undertaken by a large collaboration involving institutes from the U.K., Italy and Germany. The author has made specific contributions to this development as described in this thesis in the following areas:

1) Detector processing techniques. Substrate thinning and metallisation processes have been developed which replaced the initial manual polishing and evaporation through a brass shadow mask. These improvements are detailed in chapter 3.

2) Standardised test structures have been designed by the author as well as measurement procedures to characterise the detector performance as described in chapter 3. These structures and techniques have been used by the collaboration as a common reference set.

3) The author has designed, fabricated and tested a variety of microstrip detectors for use in High Energy Physics applications. The types of detector and results of tests, made in the laboratory and in particle test beams at CERN, are described in chapter 4. The author has carried out irradiation of test structures and an evaluation of detector performance before and after irradiation.

4) The author has adapted the processing of pixel detectors to enable them to be bump bonded to read-out electronics. A self-triggering technique has been developed by the author to enable images to be made efficiently with this type of read-out. Image evaluation techniques used by radiologists have been adapted by the author and used to evaluate the performance of pixellated GaAs detectors as X-ray imaging devices. An array of 38x38 μm pixels has been designed and fabricated by the author for use with a charge integrating read-out. This has been successfully tested with a dental X-ray set. Evaluation of high purity epitaxial material for radiation detection has also been carried out by the author. This work is detailed in chapter 5.

5) A reflective optical modulator has been designed by the author by adding an appropriately designed mirror to a transmission modulator designed and characterised by K. M°Ilvaney. The author has fabricated and tested the devices on wafers with epitaxial layers grown by CVD at Sheffield, this activity is described in chapter 6.

Acknowledgements

I would like to thank very many people for their help and encouragement during the preparation of this work. Carlo Del Papa and Liam Kelly were instrumental in kindling my first interest in this subject. Ken Smith and John Marsh, my supervisors, have been infinitely patient and ever ready with helpful advice. That this work was ever presented in its present form is entirely due to their persistent and gentle persuasion.

In the course of this study I have had the pleasure of working with several very talented teams, both in CERN and at Glasgow. Saverio D'Auria, Robert Bertin and Bohdan Lisowski were of enormous help to me at a time when the study was just beginning. When I came to Glasgow, Frank M'Devitt, Drew Meikle and Fred Docherty were of invaluable assistance. The use of the fabrication facilities in the Dept. Of Electronic and Electrical Engineering was made considerably easier with the helpful and patiently given advice of both Douglas McIntyre and Lois Hobbs.

A special word of gratitude must go to Colin Raine who has had to put up with my presence in his office for longer than he would care to remember. I also wish to thank Richard Bates and Spyros Manolopoulos for their advice and useful discussion.

During the course of this work there have been countless others who have been immensely helpful and shown considerable understanding and patience in the inevitable last minute rush that appears to be a hallmark of mine, I would like to take this opportunity to thank them for their kindness. Thanks as well to Michael and Mary Madden for tracking down Eoghan Ruadh.

When the time came to write up the work, I had very little appreciation of the effort that would be required to achieve this – had I known in advance, I don't think that you would be reading this. I thank my Mum and Dad for giving me the opportunity and encouragement I needed starting out.

Finally, none of this would have been possible without the encouragement of Pat, Áine and Eoghan who have had to put up with an ever absent husband and father for too long.

I would like to dedicate this work to my family.

Index

List of Figures and Tables

Introduction

The work described in this thesis started in 1989 with the inclusion of a project to develop GaAs radiation detectors for use in the next generation of particle physics experiments in a mega-project known as LAA. LAA, based at CERN, Geneva, was intended to develop the experimental technologies and techniques required for the operation of a particle physics experiment where the radiation environment would preclude the use of existing technologies and the anticipated data rate would render the then available acquisition systems inoperable.

The development of semiconductor tracking detectors made from GaAs was proposed based in the perception that the technology was more resistant to radiation and that integrated readout electronics might eventually be easier to achieve on GaAs. Radiation detectors made from high quality epitaxially grown layers had been investigated in the early 1970's producing good results for α and γ radiation. The quality of the as-grown material available at that time was such that radiation detection was not possible. Minimum ionising particles (MIP) had never been detected with GaAs detectors as the epi-layer was too thin to accumulate enough energy to give a detectable signal.

Advances in the growth technology over the following 15 years, driven by GaAs electronics industry, resulted in much improved material. Liquid Encapsulated Czochralski (LEC) material was chosen to make the first detectors for the LAA project as this growth technique produced large crystals normally used in the microelectronics industry. This technique involves pulling a high purity seed from a melt, which sits in a pyrolitic boron nitride vessel, through an encapsulating layer of boric oxide. The first detector structures were made in the National Microelectronics Research Centre (NMRC)in Cork, Ireland in 1988. The work described in this thesis covers work done by the author on development of GaAs radiation detectors from this time.

The first detectors produced by the NMRC with LEC material were mounted on chip carriers and could only be tested for α particles and γ-rays. Initial results showed that the response to irradiation produced pulse height spectra only for very high deposited energies and that they were much broader and smaller than expected. In hindsight, this was due to the fact that the devices had a very low breakdown voltage (around 100 V for 450 μm thick detectors) and so the charge collection efficiency was very low because of the presence of a high concentration of traps.

In parallel to this activity, a group in the Department of Physics at Glasgow University started to produce detectors on LEC material using the facilities available in the Department of Electronics and Electrical Engineering at Glasgow. Some of these samples

were tested at CERN in late 1989. The behaviour of the first devices was very similar to that of the diodes produced by the NMRC. One of the devices supplied had, however, been thinned to around 100 μm and did not break down with an applied bias of 120 V and signals from MIPs were seen on a GaAs detector for the first time. The detector was tested in a particle beam and shown to have a detection efficiency of greater than 96% even though 50% of the charge created in the detector was not collected at the electrodes. Irradiation tests carried out on these devices showed that the detectors were unaffected by γ irradiation up to 10 Mrad and that signals from MIPs were still resolvable after neutron doses of 5×10^{14} n cm^{-2}.

These encouraging results led to the approval of a research and development programme at CERN called RD8 which brought together groups from Bologna, CERN, Florence, Lancaster and Sheffield to work on GaAs particle detector development. The program of research undertook to develop and test microstrip detectors which were compatible with those being developed on the conventional silicon technology. It was also of considerable importance to demonstrate that these detectors could be made commercially so orders for detectors were placed with GEC Materials and Technology in Caswell, UK and Telletra SpA. in Italy. The results of tests on these detectors as well as the work that was done to develop a fabrication process for GaAs detectors at Glasgow is described in this thesis.

In the course of the detector development, a number of different detector configurations were designed, fabricated and tested. Results from double-sided strip detectors, microstrip detectors with 50 μm pitch, ac-coupled detectors and wedge shaped microstrip detectors are presented and discussed.

In parallel to the detector development, it was decided to start a program of irradiation of test structures in order to understand the degradation of detector performance after irradiation with various particles. The initial results from neutron and gamma irradiation were confirmed by further tests, however, more accurate simulation of the anticipated radiation environment close to the beam pipe in LHC suggested that most of the damage would come from irradiation by charged particles such as protons and pions. Irradiation with these particles created much more damage than had been expected. The reduced performance after charged particle irradiation, coupled with developments which increased the radiation hardness of silicon detector technologies, led to the latter being chosen as the technology that would be used for tracking in the LHC experiments.

GaAs pixel detectors were also developed to be compatible with OMEGA read-out chips, the connection between detector and read-out chip being made by a process known as bump bonding (flip chip bonding). The pixel detector work for High Energy Physics

(HEP) applications was extended to cover possible uses in the field of X-ray imaging for medical use and, in particular for intra-oral radiology.

Results from pixel detectors bonded to OMEGA type read-out and tested in particle beams at CERN are presented as well as measurements on the evaluation of the imaging capabilities of this system. In order to evaluate the use of much smaller pixels, detectors have been designed and tested with a charge integrating array of 38 μm square pixels bump bonded using an indium based process at IMC, Stockholm. A new photon counting chip, based on the same front-end used for OMEGA, is described; the electrical characterisation indicates that the noise performance of this chip is superior to any of its predecessors because of the use of a new technique for tuning the threshold on individual pixels.

In order to overcome the effects of native defects present in the LEC material, a study has been undertaken as part of an EU sponsored Brite-Euram program to use epitaxial techniques to grow thick (200 μm) layers of GaAs with a very low free carrier concentration. The concentration of native defects in this material is 2 orders of magnitude lower than the lowest values obtained in LEC material and this should permit the fabrication of very high quality detectors. Detectors have been fabricated from a 50 μm thick layer having a free carrier concentration of 10^{14} cm^{-3}; the test results from these detectors show that there is no measurable charge deficit and that the depletion of the device grows with the square root of the applied voltage. The most recent samples are capable of detecting MIPs – an indication that the layer is sufficiently thick and that the free carrier concentration is low enough to permit sufficient depletion in this layer.

The final section of this thesis describes the work done by the author to develop an all optical read-out for radiation detectors. GaAs, being a direct band gap material, is used extensively in the optoelectronics industry. It had been demonstrated that optical modulators could be made using multiple quantum wells (MQW) to alter the absorption of light in the structure as the electric field across the wells was changed. If the charge created in a GaAs particle detection element could be used to change the electric field across a modulator structure with a mirror underneath, the presence of the particle would be seen in the modulated light reflected from the device. A description of the design and fabrication of these devices is given, as well as details of the tests carried out and a discussion of the results

Chapter 1: Semiconductor Radiation Detectors.

1.1 Introduction

Radiation detectors which utilise semiconductor materials as their detection medium generally rely on a reverse biased diode structure to collect the charge created in the active volume of the detector. In order to illustrate the basic principles involved, the following sections explain the theory of various configurations which implement diode structures. The basic types of radiation and the way that they interact with material are then described. Following on from this, a review is given of the radiation detection mechanisms and other factors which influence particular detector performance characteristics.

1.2 Semiconductor Properties

A semiconducting material is, as its name implies, one which neither conducts electricity well nor acts as a good insulator. All of the commonly studied semiconducting materials (with the exception of amorphous silicon) are crystalline solids with a well defined lattice structure and energy bands which determine precisely the properties of each material. The treatment of the theory of semiconductors that is relevant to this thesis will be limited to the properties of silicon (Si) and gallium arsenide (GaAs). Reference will be made to other materials used for detection and read-out where appropriate.

The main semiconductors of interest all exist as variants of a tetrahedral form, (a diamond lattice for Si and zincblende for GaAs), in which each atom in the lattice is surrounded by four equidistant neighbours. The bonds between each atom and its neighbour are formed by electrons of opposite spin and are predominantly covalent although there is a slight ionic component in the bonds of GaAs. All of the outer shell electrons are bound for each atom of the lattice. The energy states of these electrons can, in principle, be found by solving the Schrödinger equation [1] using the boundary conditions imposed by the specific lattice:

$$[(-\hbar^2/2m)\nabla^2 + V(r)]\phi_k(r) = E_k\phi_k(r) \qquad (1.1)$$

where E_k is the energy of the electron in a particular state, $\phi_k(r)$ is the wave function for the electron and V(r) is the potential energy.

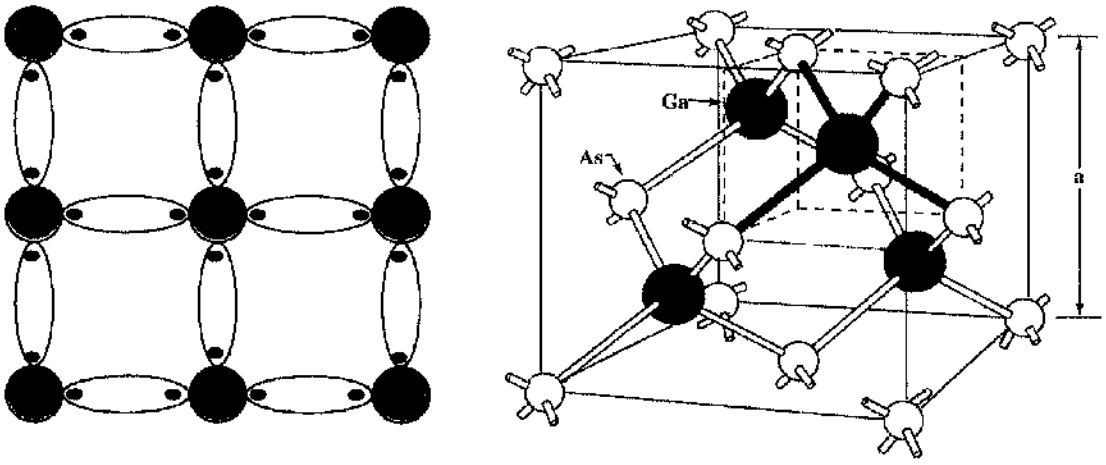

Fig 1.1. An illustration of the electron bonding between neighbouring atoms in a Silicon crystal lattice. Each Si atom is tetravalent and shares electrons with its neighbours as outlined on the right. The atomic arrangement in GaAs is shown on the right and is that of a zincblende lattice.

The solutions, known as Bloch functions, give the probability of a carrier existing with some energy in the periodic potential defined by the lattice

$$\phi_k(r) = e^{ik.r}U_k(r) \quad \text{for a periodic crystal lattice.} \qquad (1.2)$$

where $U_k(r)$ is periodic with the lattice and depends on the wave vector.

Si exists in its pure form as a crystalline solid with a tetrahedral structure. As it has four electrons in its outer electron shell, each one forms a bond to one of the four neighbouring atoms to make up one cell of the crystal lattice. One can use a 3-D co-ordinate system to define the position of all nodes on the lattice taking the lattice constant **a** as indicated in Fig 1.1. Any plane in the crystal can be defined by taking the intercepts of that plane with an orthogonal set of 3-D axes and dividing by the lattice constant **a**.

The solution of the Schrödinger equation assumes that the atoms fixed in the lattice are singly ionised, thus reducing the solution to that of the approximate one-electron problem. In reality the lattice is much more complex and this gives rise to solutions which allocate energy bands to electrons instead of discrete levels.

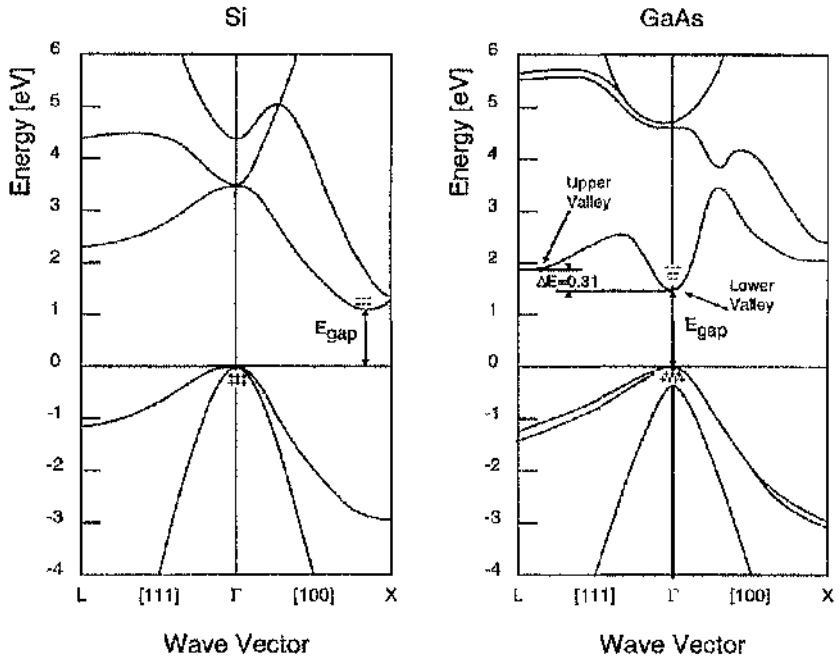

Fig.1.2. A representation of the energy band structure in Si and GaAs as a function of the wave vector [2].

The energy band structures of Fig. 1.2 illustrate a typical property of all semiconductors – a small energy gap between the allowed valence states, where the electrons are loosely tied to the lattice atoms, and the conduction band, where they move unhindered.

The energy between the highest energy of the valence band and the lowest energy of the conduction band is known as the band-gap of the material and has been measured as 1.12 eV for Si and 1.42 eV for GaAs at 300 K [3]. The operation of all semiconductor devices depends crucially on the fact that this gap is small. Metals have no band-gap and conduct electrons freely while insulators have very large band-gaps, which preclude conduction. At room temperature the thermal energy in the crystal lattice is enough to enable some of the electrons in semiconductors to leave the valence band and enter the conduction band when the band gap is small enough. The positive charge that is left behind as part of the broken covalent bond is known as a hole and may contribute to carrier movement in the opposite direction to the electrons in an applied field.

There are several differences in the properties of Si and GaAs which can be deduced from the energy-momentum diagram in Fig. 1.2. The most obvious is that the band-gap in

GaAs is larger than that of Si, which means that the number of thermally generated carriers is always lower in GaAs at a given temperature. This is an important property for radiation detectors as these free carriers generate electronic noise, which can obscure low level signals. The very important difference for GaAs technology is that the minimum conduction band energy and the maximum valence band energy occur at the same momentum value in GaAs and not in Si. This means that electron transitions in GaAs can be accompanied by the spontaneous emission or absorption of a photon, as there is no change of momentum required in going from one band to the other. The direct band gap in GaAs is the basis for the thriving optoelectronics industry in which GaAs is used to fabricate the optical devices which form the backbone of most modern high-speed telecom systems.

1.3 Conduction in Semiconductors

In a pure (intrinsic) semiconductor, there are no impurities. When there is a transition from the valence to the conduction band, both a hole and an electron are generated and consequently the hole concentration (p) and electron concentration (n) must be equal.

$$p = n = n_i \tag{1.3}$$

where n_i is the intrinsic carrier concentration of the material. Both holes and electrons contribute to the conduction process. The mobility of electrons and holes is different because scattering in the lattice depends on the effective mass. The subscripts p and n denote electron and hole values. In an applied electric field $\mathcal{E}$, these carriers move in opposite directions with mobility μ. As their charge is opposite, the current of each is in the same direction and the current density in an electric field $\mathcal{E}$ is given by

$$J = q(n\mu_n + p\mu_p)\mathcal{E} = \sigma\mathcal{E} \qquad A\ m^{-2} \tag{1.4}$$

where the conductivity is given by

$$\sigma = q(n\mu_n + p\mu_p) \qquad S\ cm^{-1} \tag{1.5}$$

Intrinsic material is almost impossible to grow reliably, as even small amounts of impurities (in the parts per billion range) can have a dramatic effect on the properties of

these materials. The intrinsic carrier concentration of Si is $n_i \approx 10^{10}$ cm^{-3}, at 300 K [3]. Since there are about 10^{22} Si atoms cm^{-3} which would require growth systems capable of purities better than one part in 10^{12}. To date these systems do not exist.

The technology does exist, however for routine control of impurity concentrations to one part in 10^8 and it is this controlled introduction of impurities into semiconducting materials (known as "doping") that has fuelled most of the major technological advances of recent decades. By selectively introducing either trivalent or pentavalent atoms into the crystal lattice, the properties of the crystal may be altered dramatically.

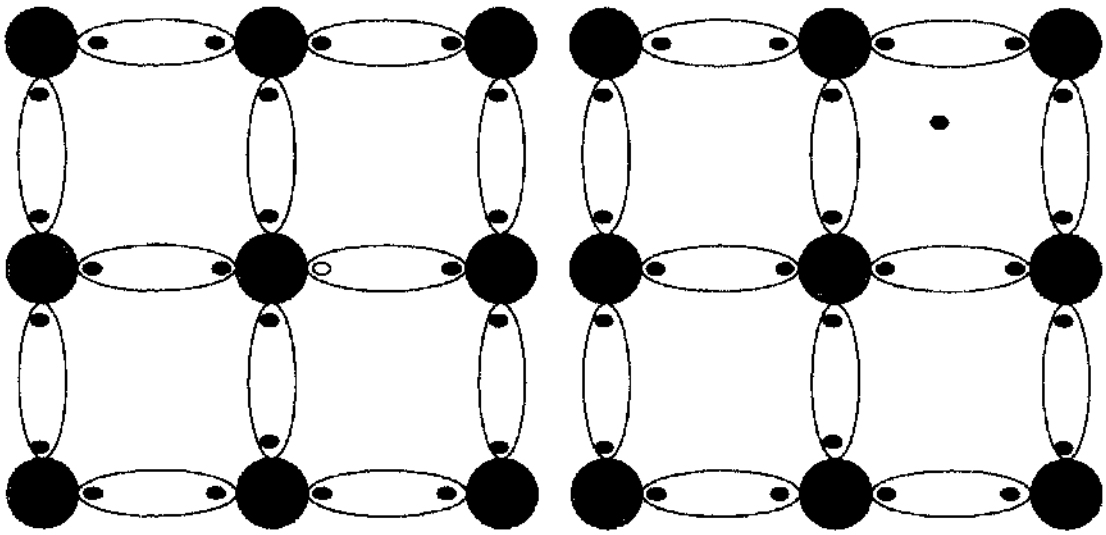

Fig.1.3. A schematic representation of doping atoms introduced in the lattice. On the left, the trivalent atom leaves a hole in the lattice as it only has 3 electrons available to bond to neighbours. The pentavalent atom introduced into the lattice on the right hand side donates an electron to the conduction band.

Semiconductors doped with pentavalent atoms are known as n-type and those doped with trivalent atoms are known as p-type semiconductors. In these materials the majority charge carriers are holes for p-type and electrons for n-type. The actual concentrations of minority carriers (electrons for p-type – holes for n-type) is suppressed to below the intrinsic level because the increased concentration of the majority carrier causes the rate of carrier recombination to increase.

For a fuller understanding of the way that doping affects carrier concentrations, it is necessary to study the energy band diagram more carefully. The Fermi Level is the energy level at which 50% of all the states available to electrons are occupied. In thermal

equilibrium, the distribution of filled energy states described by the Fermi-Dirac distribution:

$$f_D(E) = (1 + \exp[(E - E_f)/kT])^{-1} \qquad (1.5)$$

where E_f is the Fermi level, k is Boltzmann's constant, T is the absolute temperature and $f_D(E)$ is the probability that a state at energy E is filled by an electron – note that $f_D(E_f) = ½$. The Fermi-Dirac function represents the probability that an available state is occupied, it does not specify the electron population at a given energy as this also depends on the number of available states at a given energy. The density of available states is given by

$$g(E) = M_c\sqrt{2}(E - E_c)^{0.5}(m_n)^{1.5}/\pi^2\hbar^3 \qquad (1.6)$$

where M_c is the number of equivalent minima in the conduction band of the material, $\hbar$ is Planck's constant (h) divided by 2π and m_n is the density-of state effective mass for electrons [4]. The number of carriers in the conduction band can then be found by integrating the available state density – occupied state probability product over the conduction band energy.

$$n = \int f_D(E)g(E)\,dE \qquad (1.7)$$

In the case where the Fermi level is near the middle of the band-gap (non-degenerate), the integral yields the following solution.

$$n = N_c\exp(-[E_c - E_f]/kT) \qquad (1.8)$$

where N_c is the effective state density in the conduction band and is given by

$$N_c \equiv 2(2\pi m_n kT/h^2)^{1.5}M_c \qquad (1.9)$$

Similarly it can be shown that the hole concentration in the valence band may be calculated using the formula

$$p = N_v\exp(-[E_f - E_v]/kT) \qquad (1.10)$$

where

$$N_v \equiv 2(2\pi m_p kT/h^2)^{1.5} \qquad (1.11)$$

and m_p is the density-of-state effective mass of the valence band.

A typical solution of these functions is illustrated in Fig. 1.4, showing the case for an intrinsic material.

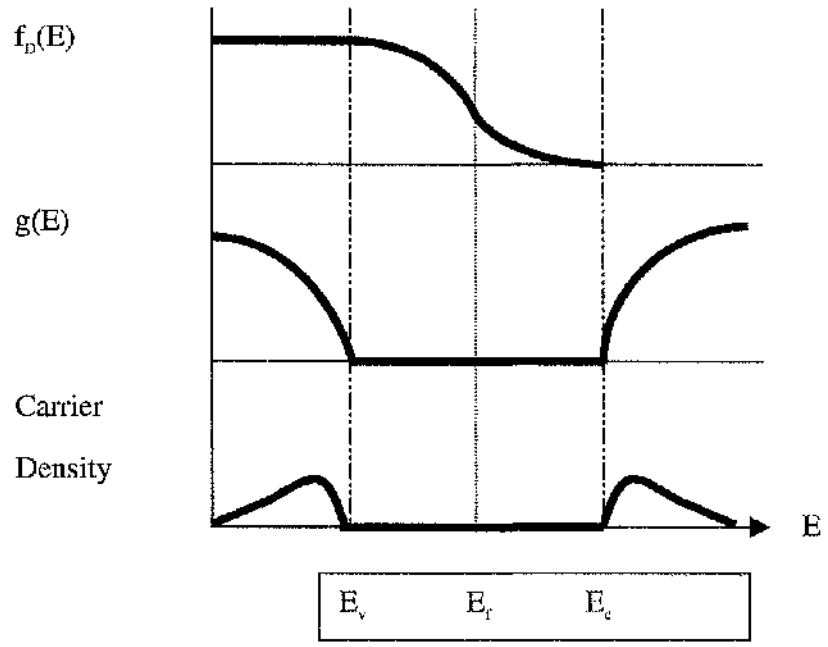

Fig.1.4. The Fermi-Dirac distribution of the probability of an electron occupying an available energy state. Also shown below are the distribution of allowed energy states for a semiconductor as a function of energy and the carrier probability distribution.

In an intrinsic material the carrier concentrations are equal and the Fermi level is given by

$$E_f = (E_c + E_v)/2 + (kT/2)\ln(N_v/N_c) \qquad (1.12)$$

and the intrinsic carrier density is

$$np = n_i^2 = N_c N_v \exp(-E_g/kT) \qquad (1.13)$$

This relation also applies to moderately doped materials. The effect of altering the doping concentration in the material is to move the Fermi level up or down from the mid-gap level depending on the type of doping that is introduced. This has a very important significance when it is applied to two neighbouring regions where the doping concentrations are substantially different as the Fermi level has to be continuous through the transition. It is this property which is responsible for the interesting properties of junctions which are central to the operation of semiconductor radiation detectors.

1.4 Junctions in Semiconductors

Two principal types of junctions in semiconductors will be considered in this section. The most common type used in Si technology, formed by contacting areas with doping of opposite polarity is known as a p-n junction and was first analysed by Shockley [5]. The second type, normally used in GaAs technology, is formed at the interface between the semiconductor and a deposited metal film. This is known as a Schottky contact and also acts as a rectifying junction [6]. An analysis of the electrical behaviour of these junctions will show that they have many similar properties but are sufficiently different to warrant individual treatment.

The p-n junction can be represented as outlined in Fig. 1.5, the junction being formed from two adjacent areas in a single crystal, one doped with acceptors (p-type), the other with donors (n-type). This is known as the abrupt junction model and provides a good understanding of junction behaviour in the case of alloyed, shallowly diffused and implanted junctions. Because of the carrier concentration gradient at the boundary there is a diffusion of holes to the right and electrons to the left across the boundary. The fixed atoms in the crystal which provided the holes initially are now negatively charged and so there is a net local negative charge on the p side of the boundary. Similarly, there is a net positive charge on the n side of the boundary.

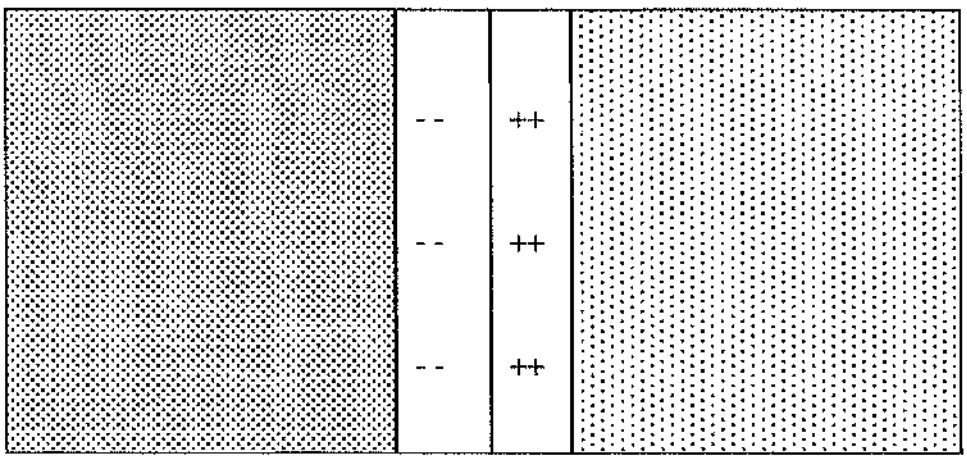

Fig. 1.5. Schematic representation of an abrupt p-n junction which shows the carrier distribution after diffusion.

There are no mobile charges in this "depletion region" and a dipole exists across the boundary as a result of the carrier diffusion.

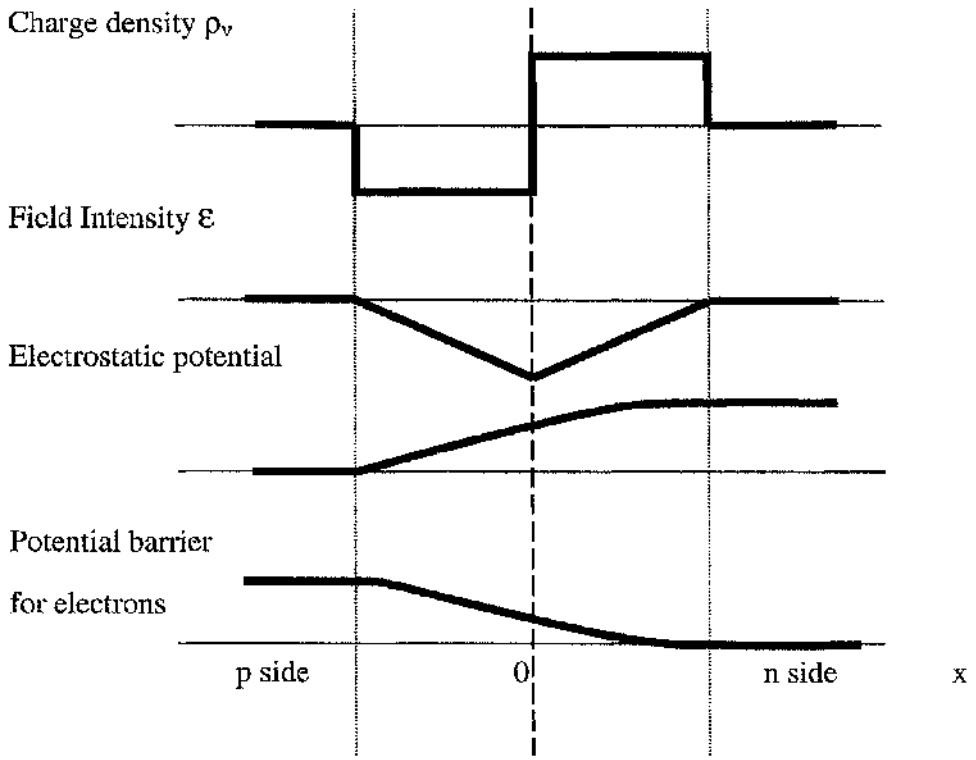

Fig. 1.6. A diagram showing the charge distribution in the depletion zone, the electric field gradient, the built-in potential and the barrier potential.

In order to preserve charge neutrality, the total negative charge per unit area on the p side must be precisely equal to the total positive charge on the n side:

$$N_A W_p = N_D W_n \tag{1.14}$$

From Poisson's equation we may write

$$-\partial^2 V/\partial x^2 \equiv \partial\varepsilon/\partial x = (q/\varepsilon_s)(p(x) - n(x) + N_D^+(x) - N_A^-(x)) \tag{1.15}$$

which reduces to

$$-\partial^2 V/\partial x^2 = qN_D/\varepsilon_s \qquad \text{for } 0 < x \le W_n \tag{1.16}$$

and

$$-\partial^2 V/\partial x^2 = -qN_A/\varepsilon_s \qquad \text{for } -W_p \le x < 0 \tag{1.17}$$

Integrating, we obtain the electric field

$$\varepsilon(x) = (qN_A/\varepsilon_s)(x + W_p) \qquad \text{for } -W_p \le x < 0 \tag{1.18}$$

and

$$\mathcal{E}(x) = -\mathcal{E}_m + qN_D x/\varepsilon_s$$

$$= (qN_D/\varepsilon_s)(x - W_n) \qquad \text{for } 0 < x \leq W_n \qquad (1.19)$$

where

$$|\mathcal{E}_m| = qN_A W_p/\varepsilon_s = qN_D W_n/\varepsilon_s$$

If we integrate again we obtain the potential distribution V(x) and the barrier potential ϕ_B for the junction.

$$V(x) = \mathcal{E}_m(x - x^2/2W) \qquad (1.20)$$

and

$$\phi_B = \tfrac{1}{2}\mathcal{E}_m W = \tfrac{1}{2}\mathcal{E}_m(W_n + W_p) \qquad (1.21)$$

Substituting for $\mathcal{E}_m$, we can obtain an expression for the depletion depth as a function of doping concentration and barrier height in an abrupt junction as shown in Fig. 1.6.

$$W = ((2\varepsilon_s\phi_B/q)(N_A + N_D)/N_A N_D)^{1/2} \qquad (1.22)$$

which reduces to

$$W = (2\varepsilon_s\phi_B/qN)^{1/2} \qquad (1.23)$$

for an abrupt one-sided junction where $N = N_A$ or N_D, depending on which far exceeds the other.

It is now appropriate to look at the properties of the Schottky barrier type of junction in the same fashion as we have analysed the p-n junction. This type of junction is a metal-semiconductor junction and is widely used in the manufacture of devices on GaAs. The principal metal characteristic that is required for this analysis is the work function of the metal, $q\Phi_m$, which is defined as the energy required to liberate an electron from the surface of the metal. The energy diagram in Fig. 1.6 shows the densities of available and filled states in the metal and semiconductor in isolation.

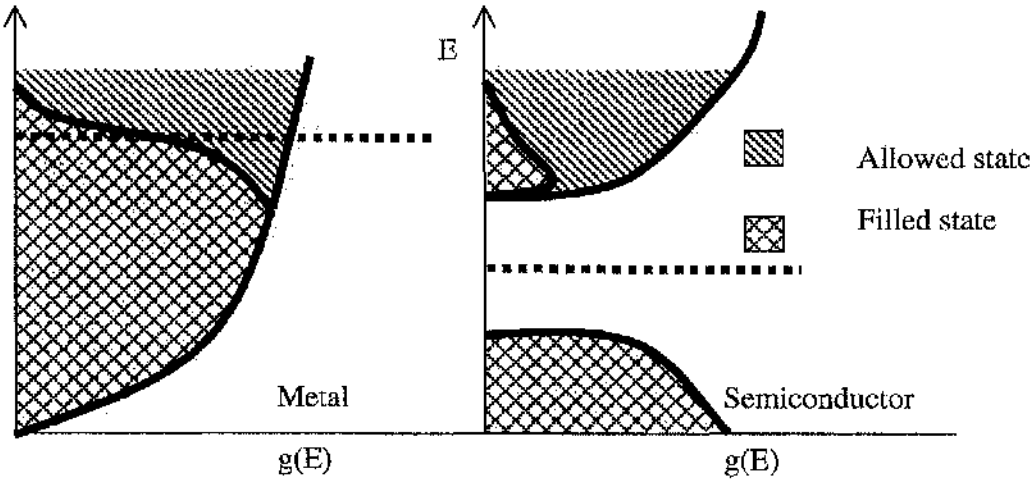

Fig. 1.7. A representation of the available and occupied states in a metal and a semiconductor. In the metal, the states have a continuous distribution and the Fermi level is at the point where 50% of them are occupied. The semiconductor has a forbidden energy gap where there are no states available for occupation.

The energy band diagrams of the metal and semiconductor as separate entities are sketched in Fig. 1.8 for Gold and GaAs.

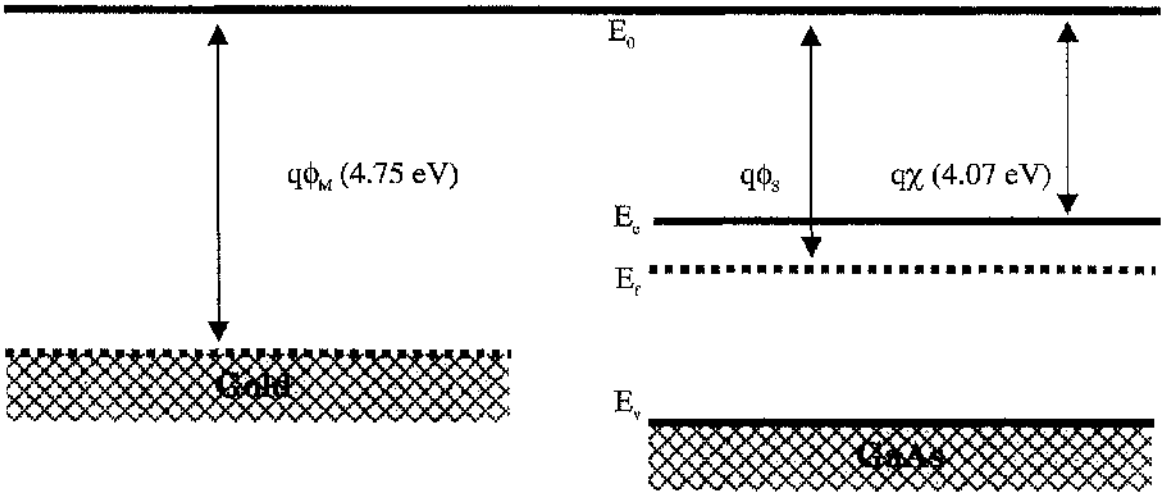

Fig. 1.8. The significance of the work function of Au and the electron affinity of GaAs relative to a fixed external energy level which is known as the vacuum or free-electron energy.

The free-electron energy is the energy, E_0, which an electron would possess were it just free of a given material. It is obvious that the absolute energy this electron has is

independent of the material from which it escaped and so E_0 is a continuous quantity. The amount of energy required to free the electron differs for each material. In Fig. 1.8 Φ_M is greater than Φ_S and so electrons in the semiconductor have more energy than those in the metal, on average. When an intimate contact is established between the two materials, the disparity in average energies can be expected to cause a transfer of electrons from the semiconductor into the metal. The Fermi level must also be continuous through the junction. Because of the charge transfer, the valence and conduction energy bands are curved as they approach the junction. A general shape for the band diagram can now be drawn as in Fig. 1.9.

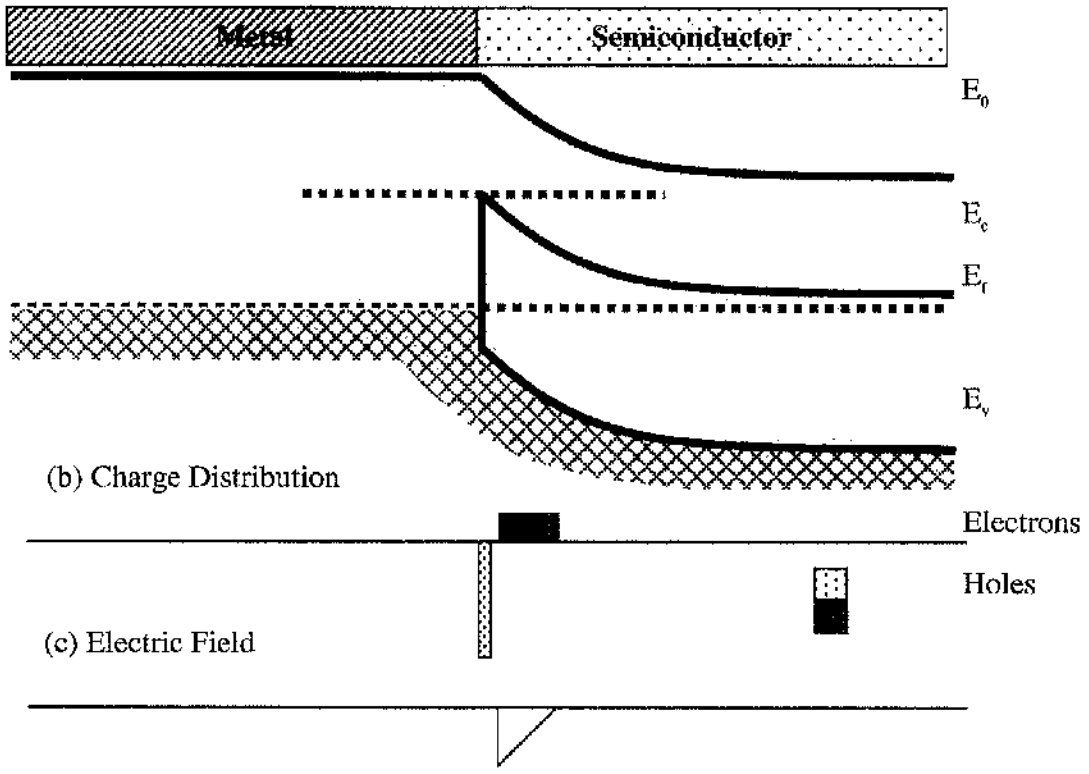

Fig. 1.9. The energy band diagram for an idealised metal semiconductor contact where Φ_M is greater than Φ_S. The resulting flow of charge is distributed about the junction as described in (b) and gives rise to the Electric field shown in (c).

It is evident from the band diagram that there is a sharp discontinuity in the density of allowed energy states at the interface. The magnitude of this step is $q\Phi_B$, where

$$q\Phi_B = q(\Phi_M - \chi) \qquad (1.24)$$

The metal may be considered to be a perfect conductor and therefore the charge transferred to it from the semiconductor exists on a plane at the interface. If we assume that the free hole concentration is so small everywhere that it may be neglected and that

the electron density in the space charge region is much less than the donor density, then we can approximate the behaviour of the junction using the depletion model developed for p-n junctions. Although the assumptions are not exactly correct, they are generally sufficiently valid to permit a useful analysis. The depletion depth is equal to the space charge region in the semiconductor as all the space charge in the metal lies at the interface and the field is a linearly changing function of position in the semiconductor (for a uniformly doped material). The maximum value of the electric field is given by

$$\varepsilon_{max} = -qN_D W_d/\varepsilon_S \qquad (1.25)$$

where ε_s is the permittivity of the semiconductor, N_D the carrier concentration and W_d the depletion width. It is evident from the behaviour of the junction that its characteristics are broadly similar to those of p-n junctions and, indeed, one can derive a similar formula for the behaviour of junction capacitance with applied bias for the stored charge Q_s,

$$Q_s = (2q\varepsilon_s N_D(\phi_i - V_b))^{1/2} \qquad (1.26)$$

then we can write

$$C = \partial Q_s/\partial V_b = (q\varepsilon_s N_D/2(\phi_i - V_b))^{1/2} = \varepsilon_s/W_d \qquad (1.27)$$

as the capacitance per unit area for a Schottky diode with an applied bias V_b– it has the same form as the expression for the capacitance of an abrupt p-n junction where the doping level on one side is negligible compared to the other (See formula 1.23).

1.5 Current flow in semiconductor junctions

Current flow due to either carrier has two principal components in semiconductors, one due to any electric field that might be present and the other due to carrier diffusion. The component due to an electric field is known as drift current. If we look at a free electron in a crystal lattice with a small electric field, it will be accelerated along the field direction. It will be involved in collisions with atoms and phonons of the lattice, which will perturb the path of the electron so that it is randomly scattered by the lattice but has an overall motion parallel to the applied field.

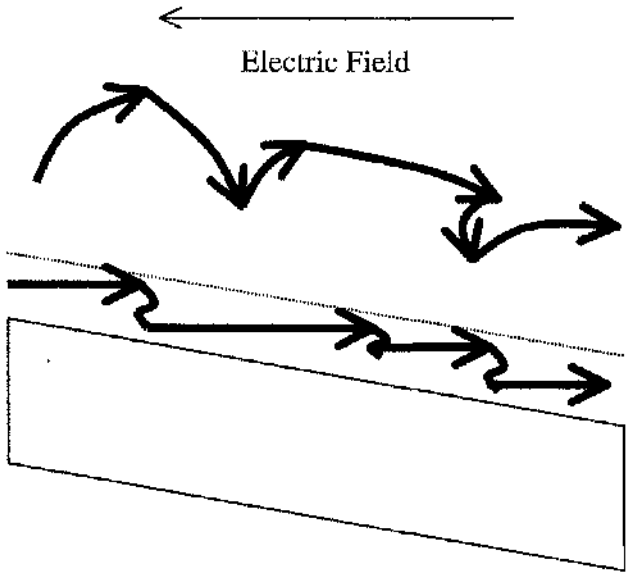

Fig. 1.10. A representation of the motion of an electron through the lattice under an applied electric field. The energy bands of the semiconductor vary linearly with the field and the electron loses energy at each collision.

The drift velocity υ_d of the carriers is proportional to the electric field so that

$$\upsilon_d = -\mu\varepsilon \tag{1.28}$$

where μ, the mobility of the carrier, is determined by the properties of the lattice through which the carrier is travelling. The drift velocity can be determined from the net gain in momentum of the carrier due to impulses from the electric field between collisions, which gives

$$-q\varepsilon\tau_{cn} = m^*\upsilon_d \tag{1.29}$$

where τ_{cn} is the mean scattering time for the carrier.

It follows from this that $$\mu = q\tau_{cn}/m^* \tag{1.30}$$

The current per unit area, denoted by J is the number of carriers per unit time per unit area traversing a surface

$$J_n = \sum_{i=1}^{n} -qv_i = -nqv_d = nq\mu_n\varepsilon \tag{1.31}$$

for electrons as and similarly

$$J_p = pq\mu_p\varepsilon \tag{1.32}$$

for holes. The total current flowing J_t is the sum of these quantities and the conductivity of the material, σ can be seen to be given by

$$J_t = \sigma\varepsilon \qquad \text{where} \quad \sigma = nq\mu_n + pq\mu_p \tag{1.33}$$

This component exhibits the behaviour described by Ohm's Law as the resistivity is independent of the field. In semiconductors, local variations in carrier density give rise to diffusion and thus a current. Consider a section of material having a carrier concentration gradient as illustrated in Fig. 1.11, assuming that the density varies in one dimension only and that the carrier energy is constant across the section. If the mean free path of a carrier, λ, is defined as the product of the thermal velocity of the carrier and its mean time between collisions (with the lattice and other carriers) we have

$$\lambda = v_{th}\tau_{cn} \tag{1.34}$$

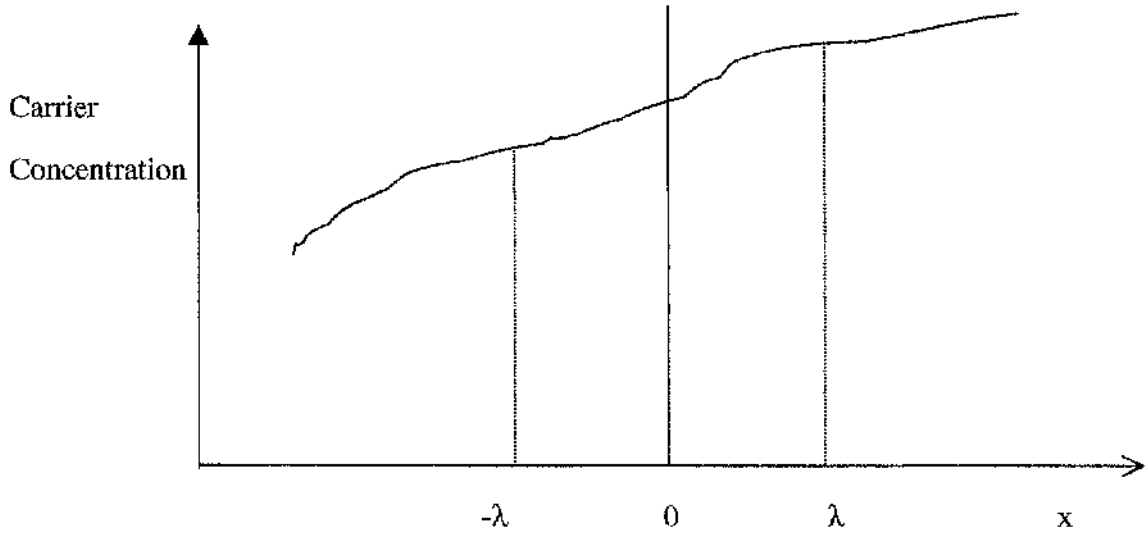

Fig. 1.11. Carrier concentration n versus distance x in a hypothetical one dimensional semiconductor. The collision mean free path length is indicated by λ.

The number of carriers which crosses the plane at x = 0 from the left, on average is $\frac{1}{2}n(-\lambda)v_{th}$ as carriers at $x = -\lambda$ will diffuse equally in either direction. Similarly the number crossing from the right is equal to $\frac{1}{2}n(\lambda)v_{th}$, so that we have a net flow across x = 0 of

$$F = v_{th}[n(-\lambda) - n(\lambda)]/2 \tag{1.35}$$

For small variations in both density and x, we can approximate the carrier concentrations at λ and $-\lambda$ by the first two terms of a Taylor expansion to get

$$F = \tfrac{1}{2}v_{th}\{[n(0) - dn(\lambda)/dx\ ] - [n(0) + dn(\lambda)/dx]\} = -v_{th}\lambda(dn/dx) \qquad (1.36)$$

Taking the kinetic energy of the carrier for a one-dimensional case,

$$\tfrac{1}{2}m^{*}v_{th}^{2} = \tfrac{1}{2}kT \qquad (1.37)$$

we can now consider the diffusion current as

$$J = -qF = q\lambda v_{th}(dn/dx) = q[(kT/q)\mu](dn/dx) = qD(dn/dx) \qquad (1.38)$$

D is known as the diffusion constant and the equality $D = (kT/q)\mu$, known as the Einstein relation, relates the two important quantities which characterise free-carrier transport in a solid. When an electric field is present in a semiconductor, the current has contributions from both drift and diffusion and the total current density may be expressed as

$$J = q\mu n\varepsilon + qD(dn/dx) \qquad (1.40)$$

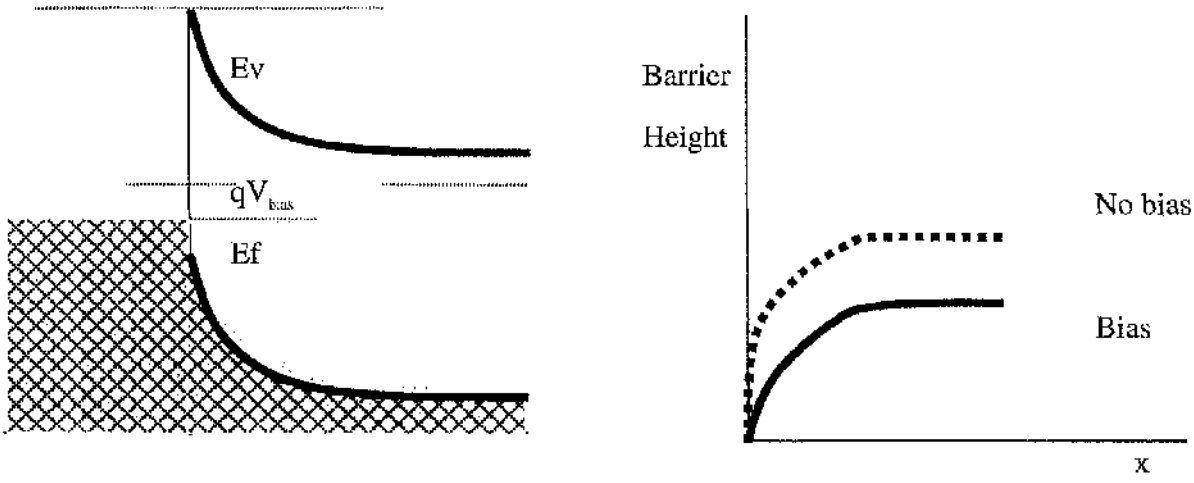

Fig. 1.12. Energy band diagram for a rectifying Schottky contact under forward bias. The applied voltage V_{bias} displaces the Fermi levels. Also shown is the decrease in barrier height across the depletion layer.

The current–voltage characteristic for a Schottky junction under bias (as shown in Fig. 1.12) is found by substituting μ to get

$$J = qD[(-qn/kT)(d\phi/dx) + (dn/dx)] \qquad (1.41)$$

where ϕ is the barrier potential. Using the boundary conditions for $x = 0$ and $x = W_d$ namely

$\phi(0) = V_{bias}$, $\phi(W_d) = (\phi_i - V_{bias})$, $n(0) = N_c\exp(-q\phi_B/kT)$ and $n(W_d) = N_d = N_c\exp(-q\phi_n/kT)$ and the fact that

$\phi(x) = (qN_d x/\varepsilon_s)(W_d - (x/2))$ yields a solution of the form

$$J = J_s[\exp(qV_{bias}/kT) - 1] \qquad (1.42)$$

with

$$J_s = A^* T^2 \exp(-q\phi_B/kT)$$

where A* is the effective Richardson constant for thermionic emission. This is normally modified to the more useful

$$J = J'[\exp(qV_{bias}/nkT) - 1] \qquad (1.43)$$

in which J′ is taken as a constant and the "ideality factor"n is experimentally determined.

A more rigorous treatment of the properties of rectifying junctions can be found in references [7], [8], [9] and [10].

1.6 Radiation Detection

Having discussed the theory of rectifying junctions in semiconductors we are now in a position to look at how a radiation detector actually works. The basic mechanism relies on the fact that all radiation deposits energy in the medium through which it passes. In the case of semiconductor detectors, this energy creates electron-hole pairs along the trajectory of the particle or, in the case of photons, as they interact with the detection medium. If an electric field is present in the semiconductor these carriers will move and create a current in the external contacts of the device. This can be amplified to form a signal which is proportional to the charge created in the active volume of the device. In order to detect signals at an extremely low level, the background current that flows in the device must be minimised. The active thickness of the detector is also very important for the detection of very penetrating types of radiation as the deposited energy depends on the path length and higher energy photons, as it determines the detection efficiency for these photons. The requirements for a detector structure are satisfied by a reverse biased diode where the active layer is provided by the depletion region. The reverse biased leakage current is extremely low and, by using a material with very low free carrier concentrations, large depletion depths can be obtained.

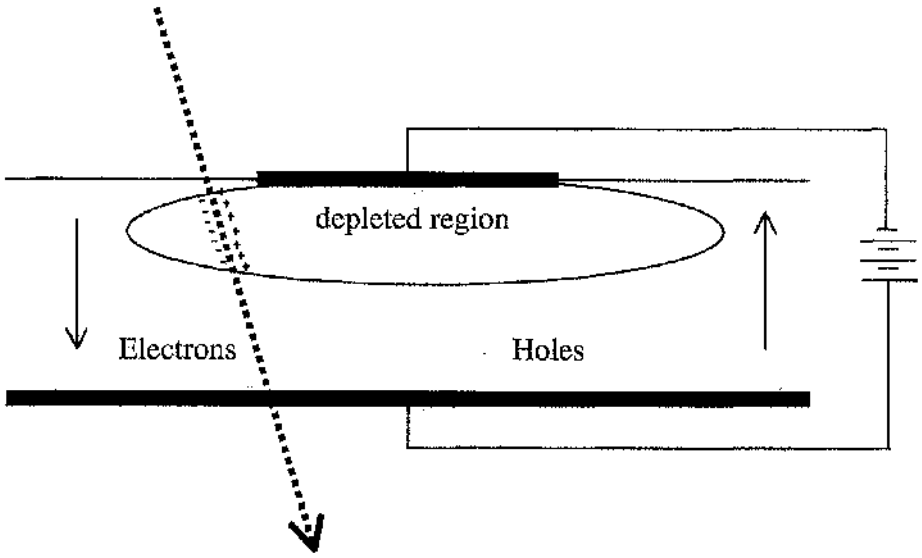

Fig. 1.13. Schematic of basic detection mechanism for a semiconductor radiation detector. In this case the particle passes completely through the material but any energy in the depleted volume of the detector can be detected.

At this point it is important to examine the basic types of radiation that we are interested in measuring with this type of detector to understand how they interact with matter and the effect that this has on detector operation.

1.7 Charged Particles

Charged particles interact with the surrounding material primarily through electromagnetic scattering by the electrons in the atoms of the material and by the nuclei of these atoms. Inelastic scattering by electrons is the dominant mechanism as the mass of the nucleus is large in comparison to the mass of the particle. The amount of energy transferred in each collision is generally a small fraction of the energy of the particle but there are very many such collisions per unit path length. The energy loss per unit path length is known as the specific energy loss, symbolised by dE/dx . The Bethe-Bloch formula [11], most commonly used to describe dE/dx, gives

$$\frac{dE}{dx} = 2\pi N_a r_e^2 m_e c^2 \rho \frac{Z}{A}\frac{z^2}{\beta^2}\left[\ln\left(\frac{2m_e\gamma^2 v^2 W_{max}}{I^2}\right) - 2\beta^2 - \delta - 2\frac{C}{Z}\right] \qquad (1.44)$$

where: r_e = classical electron radius — ρ = density of absorbing material

m_0 = electron mass — z = incident particle charge in units of e

N_a = Avagadro's constant — $\beta = v/c$ for the incident particle

I = mean excitation potential — δ = density correction

Z = atomic number of the absorber — 2C/Z = shell correction

A = relative atomic mass of the absorbing material

W_{max} = maximum energy transfer in a single collision

$\gamma = (1 - \beta^2)^{-\frac{1}{2}}$ — q = unit electronic charge with $q^2/m_0c^2 = r_e$

The Bethe-Bloch formula is not valid for very low particle energies where other effects not included in the formula tend to dominate. The specific energy loss to the medium falls steeply with increasing particle energy until $\beta = 1$ and the particle becomes relativistic. At this point the energy loss passes through a broad minimum where the dE/dx is said to be that of a "minimum ionising particle" (MIP) before rising slowly and saturating due to screening effects introduced by the "density correction" [12]. This behaviour is shown in Fig. 1.14.

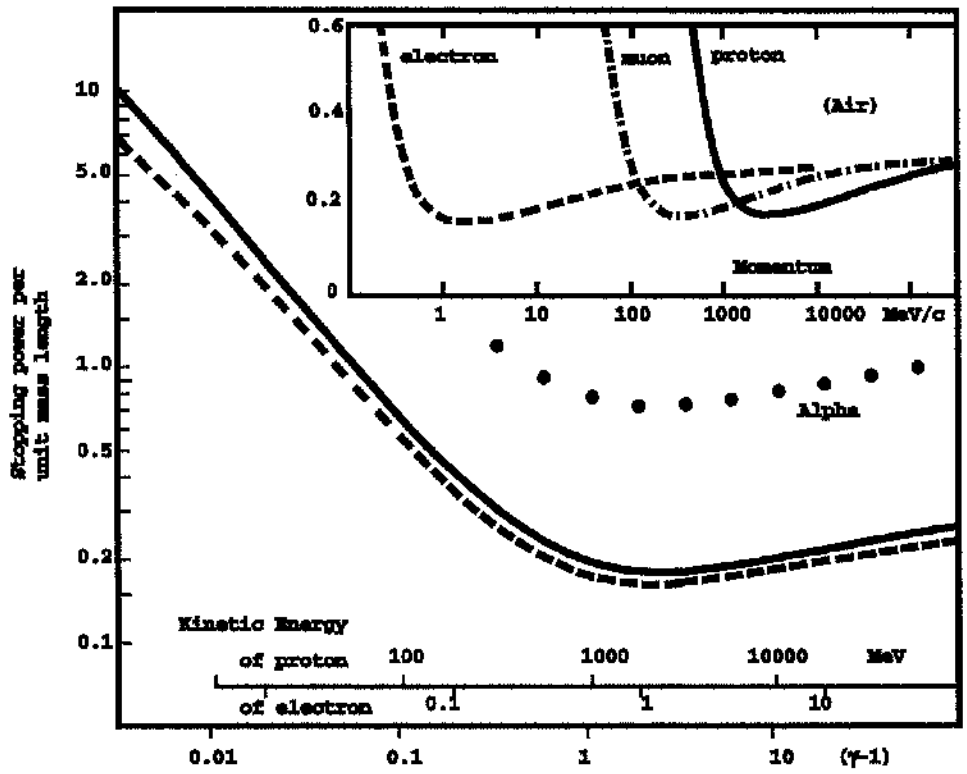

Fig.1.14. dE/dx versus incident particle energy for some different particles.

The dE/dx of a particle is a function of the energy of the particle, and so particles which lose energy quickly in a material deposit an increasing amount of energy along their path through the material. At this point it is useful to consider two possibilities for the energy loss along the path of the particle as it traverses a material. In the first, the particle has insufficient energy to pass through the material completely and its dE/dx increases as it loses energy progressively to the medium. After it has travelled a distance in the material, equal to the range of the particle, it comes to rest, having lost all its energy to the material. The distance it has travelled in the material is known as the range of the particle and it loses most of its energy close to this distance according to the Bragg curve [13] (Fig. 1.15)

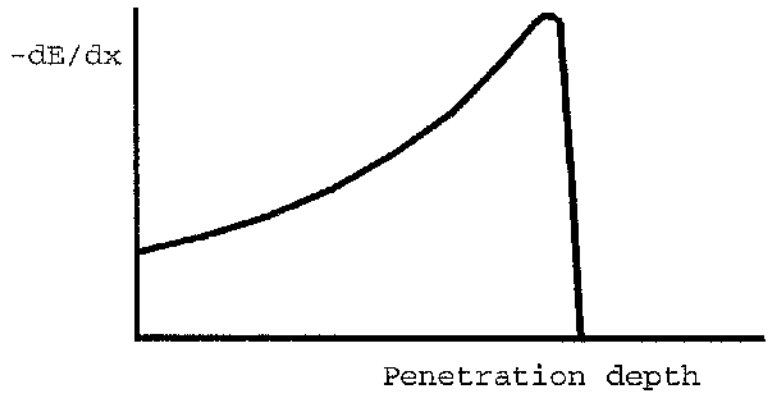

Fig. 1.15. The characteristic Bragg curve which plots the change in specific energy loss with distance travelled in a medium.

This type of energy loss is typical of heavy particles, for example alpha particles from Am^{241}, with an energy of 5.4 MeV, have a range of about 22 μm in GaAs. Protons of 3 MeV, travel about 55 μm in the same material [14]. This limited range is very useful if one wants to look at the contribution of one carrier to the extracted charge, as illumination by the source from one side or the other of the detector changes the type of carrier that contributes to the output signal. It is important to note that the total energy loss is the sum of very many small energy exchanges between the particle and the medium and so there is a statistical variation associated with each quantity. Individual particles will not always be involved in the same number of atomic collisions, nor lose the same amount of energy in each one.

In the second case, the particle has enough energy to traverse the detection medium and emerge on the far side. If the detector is thick enough, the number of collisions is sufficiently large to eliminate the bias of more common low energy depositions and the energy deposition has a Gaussian distribution about the mean energy value. If the detector

is thin, however, the energy loss distribution is no longer symmetric, with a high energy tail caused by rarer, high energy transfers that are lost in the distributions for thicker detectors. The characterisation of energy loss in thin detectors was carried out by Landau [15] and the characteristic energy distribution, known as a Landau distribution, has the form

$$f(s,\Delta) = \frac{1}{\xi}\phi(\lambda) = \frac{1}{\xi}\frac{1}{2\pi i}\int_{\sigma-i\infty}^{\sigma+i\infty} e^{(u\ln u+\lambda u)}du \qquad (1.45)$$

where $\xi = ks$ s being the thickness of the detector and $k = \frac{2\pi z^2 q^4 N_a Z}{m_e c^2 \beta^2 A}$

with these parameters as defined for Eq. 1.44. The function $f(s,\Delta)$ represents the probability that a particle loses an amount of energy Δ while traversing a layer of thickness s. A more complete treatment of this topic may be found in the reference [27, 115].

This distribution has the shape shown in Fig. 1.16 and is characteristic of the signal distribution from MIP's in all of the detectors discussed in this thesis. The distribution is characterised by a most probable value of deposited energy which is significantly lower than the mean value.

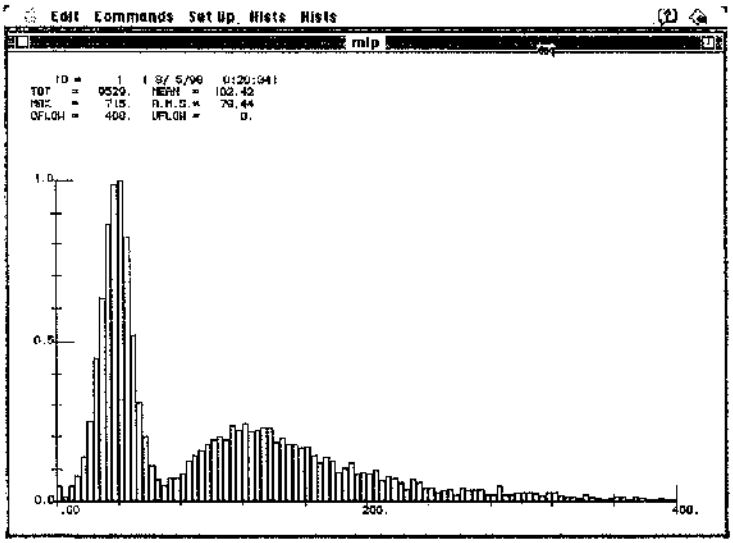

Fig. 1.16. The Landau distribution of deposited energy in a thin detector is the asymmetric distribution to the right, the peak on the left is the noise. The high energy tail in the distribution, arising from delta electrons in the detector, can limit the ultimate position resolution in very finely segmented detectors. The frequency of counts in each channel is plotted on the vertical axis, while the horizontal axis represents the magnitude of the sampled signal.

1.8 Photons

The photons which we will discuss in this section are typically X- and gamma rays, where the energy is much higher than that found in the photons of light. These interact with matter by three basic processes:

1) Photoelectric effect.
2) Compton Scattering.
3) Pair Production.

The photoelectric effect involves the absorption of the photon by an atomic electron. In the case of photoelectric conversion a bound atomic electron absorbs all of the photon energy and is ejected from the atom. It then loses energy to the detector as a classical charged particle would and the detector sees all of the initial photon energy, assuming that the x-rays or Auger electrons from the subsequent atomic rearrangement are also absorbed. If the interaction is with a quasi-free electron which does not absorb all of the photon energy, the Compton scattered photon continues on a different path. In this case the energy deposited in the detector is some fraction of the incident photon energy.

Pair production can only occur if the photon energy is above the critical energy of twice the rest mass of the electron (1.022 MeV). The spectra of deposited energy for photons typically show all of the above features at the same time as a particular photon, may interact with the detecting medium through any of these several modes of interaction. On the other hand, the photon may pass through the material without an interaction. Each photoelectric conversion in the material deposits the full energy of the photon except in the case where an X-ray generated in filling the vacancy left by the escaping photo-electron itself escapes from the detector, leading to a lower peak called an escape peak.

A Compton scattered photon can emerge from the detector, giving rise to a low energy Compton electron continuum in the deposited energy spectrum, which extends from the lowest energies to a maximum energy, the Compton edge, corresponding to 180° scattering.

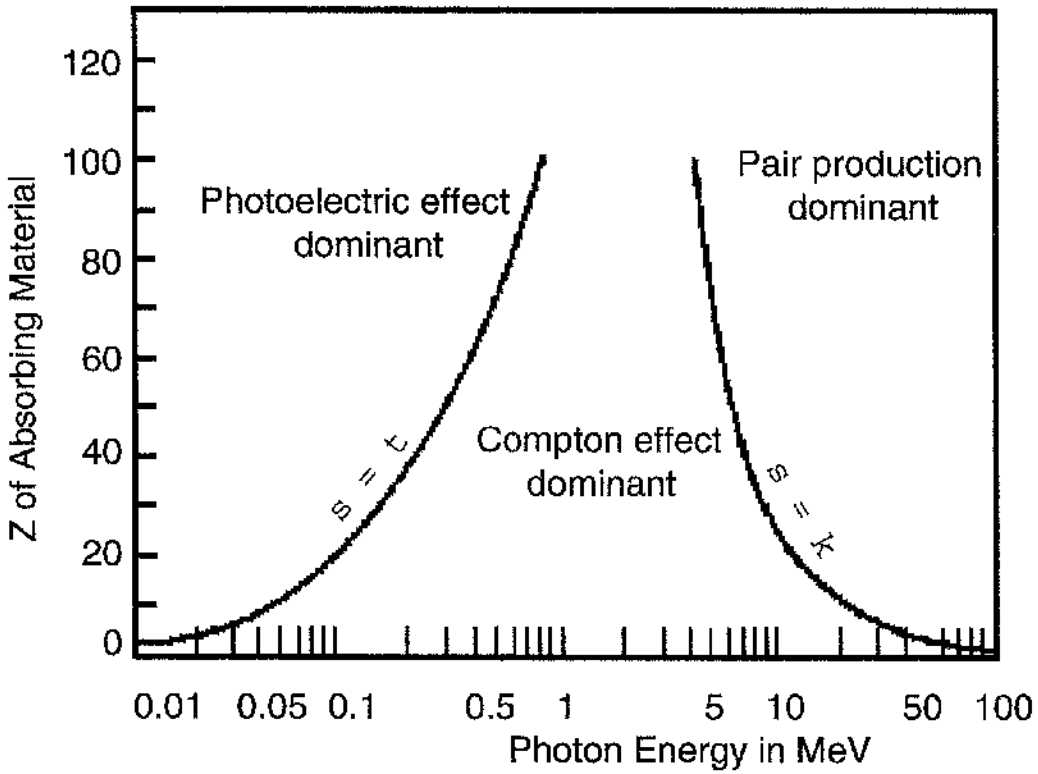

Fig. 1.17. A figure showing the interaction processes for photons as a function of incident photon energy and atomic number of the target material [16].

All of these different possibilities give rise to much more complex energy deposition distributions for high energy photons in a detector material. A typical spectrum for a mono-energetic photon spectrum in GaAs is shown in Fig. 1.18 illustrates some of these features [17].

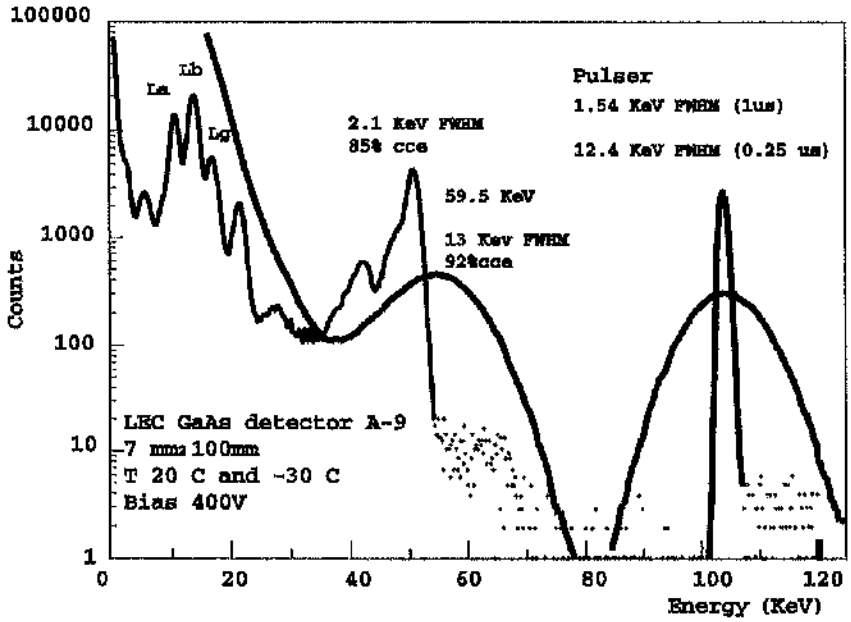

Fig. 1.18. The spectrum of 60 keV gamma rays from Am^{241} as detected by a GaAs detector at 20°C and -30°C.

The preceding sections permit a basic understanding of the properties of semiconductors and how these can be used to implement a device which can function as a radiation detector. The discussion of how radiation of different types interacts with matter to create a detectable signal also provides sufficient detail for an understanding of the tests and characterisation of the detectors that have been fabricated during the course of this study. A table of the properties of some semiconductors used to make radiation detectors is included after the references. In order to appreciate the detector operation fully it is necessary to consider what happens to the signal created in the detector. The following chapter is devoted to the explanation of the operation of the system, taking into account the read-out electronics, noise generation and signal processing.

Chapter 2: Electronic Noise and Readout Electronics.

2.1 Noise in Radiation Detector Systems

The charge signal created in a detector can vary due to fluctuations in the deposited energy, as discussed in chapter 1. The detector itself generates a "noise" signal which has a finite distribution in charge even when there is no signal present due to ionising radiation. The noise depends on the detector properties, the read-out amplifier and the signal processing used after the amplification stage. In the analysis of the performance of the system, it is possible to define the noise at the output of the amplifier completely in terms of the properties of the detector and the input transistor followed by a noiseless read-out chain.

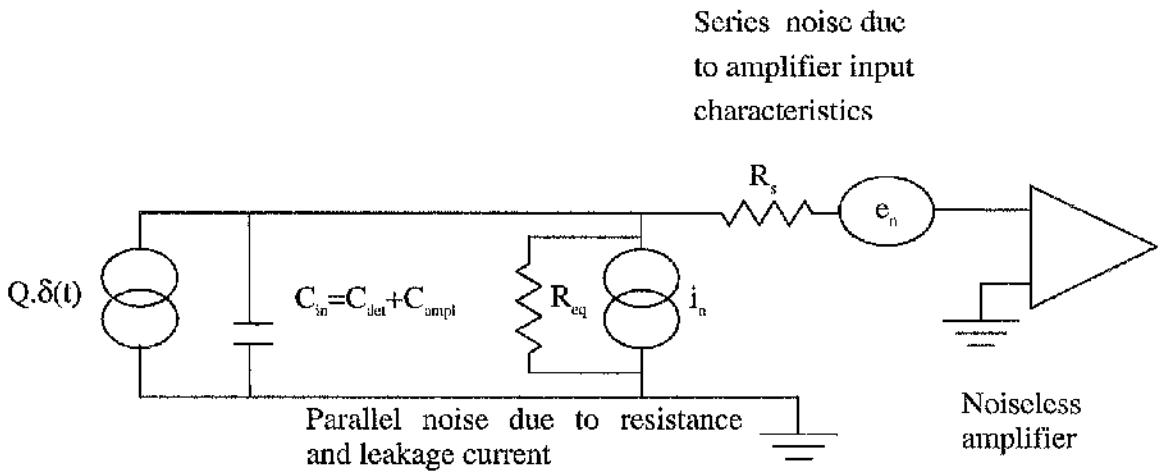

Fig. 2.1. A schematic representation of a detector and the principal sources of noise in a typical readout chain. R_s and R_{eq} are the series input resistance of the amplifier and the equivalent resistance of the detector and biasing circuit.

The principal sources of noise that can be attributed directly to the detector are illustrated in Fig. 2.1. These can be separated into a parallel current noise source, which includes contributions from Johnson (thermal) noise in resistors as well as shot noise from leakage current, and a series voltage noise which arises primarily from the properties of the input transistor of the pre-amplifier. In evaluating the contributions of the various noise sources to the accuracy of a particular measurement it is convenient to employ a quantity known as the equivalent noise charge (ENC), as discussed in the

following section. Each detector element is usually read out by a charge sensitive amplifier (Current/voltage amplifiers are not normally used for this purpose as they generally add much more noise to the measurement chain). The charge amplifier integrates the current that flows in the detector element for a predetermined period of time. The charge amplifier is normally followed by a circuit which shapes the signal with a time constant which can be optimised to reduce the noise from a detector to a minimum for any given detector parameters. This signal is then shaped with a suitable weighting function W(t), which produces an output signal proportional to the integrated charge.

2.2 Noise Spectral Density

The analysis used to determine the noise performance of a detector system uses the concept of noise power spectral density to evaluate the variance σ of the output of the measurement system in terms of an equivalent noise charge ENC at the input. The parallel current generator gives rise to a series of current impulses which contribute to the output of the system. The series noise voltage can be transformed to a series of current 'doublets' using the total input capacitance of the system. It is this transformation that allows one to optimise the noise performance of a charge amplifier/shaping system so that the noise may be minimised. If $\bar{n}$ is the mean rate of impulses in a time interval dt, then the variance of the number of impulses in the interval is equal to $\bar{n}dt$. The total mean-square noise charge is obtained by integrating over the time interval where the shaping function is non zero. The ENC for such a system [19] can be shown to be:

$$\overline{ENC_p^2} = \frac{1}{2}\overline{i_n^2}\int_{-\infty}^{\infty}[W(t)]^2 dt \qquad (2.1)$$

$$\overline{ENC_s^2} = \frac{1}{2}\overline{e_n^2}\int_{-\infty}^{\infty}[W'(t)]^2 dt \qquad (2.2)$$

The leakage current can be defined as the total current at a particular point in time, made up of very many small contributions from each electron that is moving in the bulk of the semiconductor. There is a statistical variation in the current which is related to its amplitude. This so-called "shot noise" is characterised by a mean square current given by

$$\frac{d\overline{i_n^2}}{df} = 2q_0 I_L \tag{2.3}$$

where q_0 is the electronic charge and I_L is the leakage current of the detector. This "shot noise" has a Poisson distribution which is approximated to a Gaussian distribution for the purpose of the following analysis. This type of noise is one of a number of 'white noise' sources whose spectral density has no frequency dependence. There is no frequency component in the noise spectral density only if the carriers are randomly generated in time and if, in addition, the recombination of these carriers is not characterised by any time constants. This is normally the case for perfect lattices, however in the case of poor quality GaAs a large fraction of the leakage current is normally generated due to the presence of traps (imperfections) in the crystal lattice. These traps are characterised as permitted energy levels within the forbidden gap and have time constants determined by the nature of the individual trap.

The thermal fluctuation in the feedback resistor of the amplifier or the de-coupling resistor in the detector bias supply contribute thermal or 'Johnson' noise according to the formula:

$$\frac{d\overline{i_n^2}}{df} = 4kT\frac{1}{R_p} \tag{2.4}$$

where R_p is the total parallel resistance seen at the input of the amplifier.

The contributions to the series voltage noise depend strongly on the parameters of the input transistor. In the case of a bipolar transistor, the base spreading resistance and the transconductance of the device determine its noise performance according to [19]:

$$\frac{d\overline{e_{ns}^2}}{df} = 4kT(r_{bb'} + \frac{1}{2g_m}) \tag{2.5}$$

The corresponding expression for an amplifier with a FET input device can be shown [29] to be:

$$\overline{e_n^2} = \frac{2}{3} \cdot \frac{4\,kT}{g_m} \qquad (2.6)$$

With a relatively simple shaping function, the effect of changing the shaping time for a particular detector becomes immediately obvious. Consider, for example, a uni-polar triangular shaping function, with equal rise and fall times, peaking at t_m and unity gain as illustrated in Fig. 2.2.

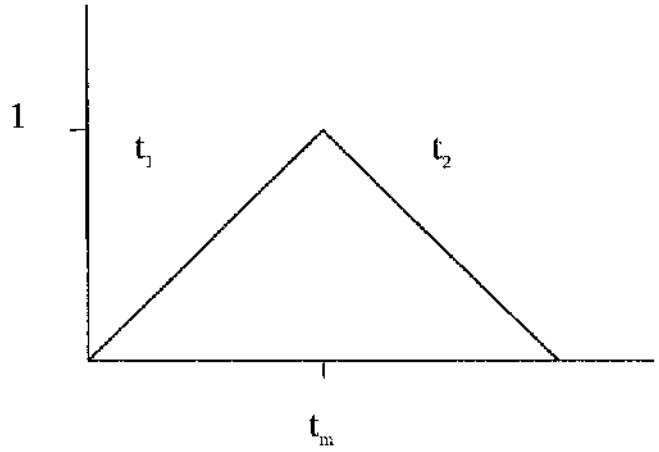

Fig.2.2. A representation of a shaping function which can be used to analyse the noise performance of a circuit.

If the shaping function is shifted in time by $-t_m$ then the function w(t) defined by:

$$w(t) = \left(1 + \frac{t}{t_m}\right) \qquad -t_m \le t \le 0 \qquad (2.7)$$

$$w(t) = \left(1 - \frac{t}{t_m}\right) \qquad 0 \le t \le t_m \qquad (2.8)$$

has integrals of $w(t)^2$ and $w'(t)^2$ of $(2/3)t_m$ and $2/t_m$ respectively. Since the parallel and series noise sources are un-correlated and assumed to be Gaussian, the total ENC for a detector and read out circuit is given by:

$$ENC_{tot} = \sqrt{ENC_p^2 + ENC_s^2} \qquad (2.9)$$

The interesting property of t_m is that the ENC has components which vary, both in proportion and in inverse proportion, to the shaping time. There is a minimum ENC for any particular set of system parameters, which can be achieved by tuning the shaping time to t_{opt} which gives the minimum noise. τ is normally used to denote the shaping time of filter circuits used with charge amplifiers as illustrated in Fig. 2.3. The system noise performance as a function of τ is characterised by

$$ENC_{tot}^2 = A\tau + \frac{B}{\tau} + C \qquad (2.10)$$

This gives rise to the type of curve shown below in Fig. 2.3, which is characteristic of the noise performance of a typical detector and read out system. The constant term C is due to noise sources which are independent of τ and are lumped together under the generic term of "1/f noise". The principal sources are dielectric losses in capacitors, frequency dependence of resistive elements and crystal imperfections in the lattice of the detector material which give rise to trapping centres. In the investigation of GaAs detectors, the presence of traps in the material causes a large 1/f component in the noise of the detector and also gives rise to a very much increased leakage current. In reality, however, the total noise measured is always less than that calculated using the measured value of leakage current, as the 'white noise' component is caused by a small fraction of the leakage current. The rest of the leakage current contributes to the 1/f noise which is small within the bandwidths which are of interest for typical detector measurements.

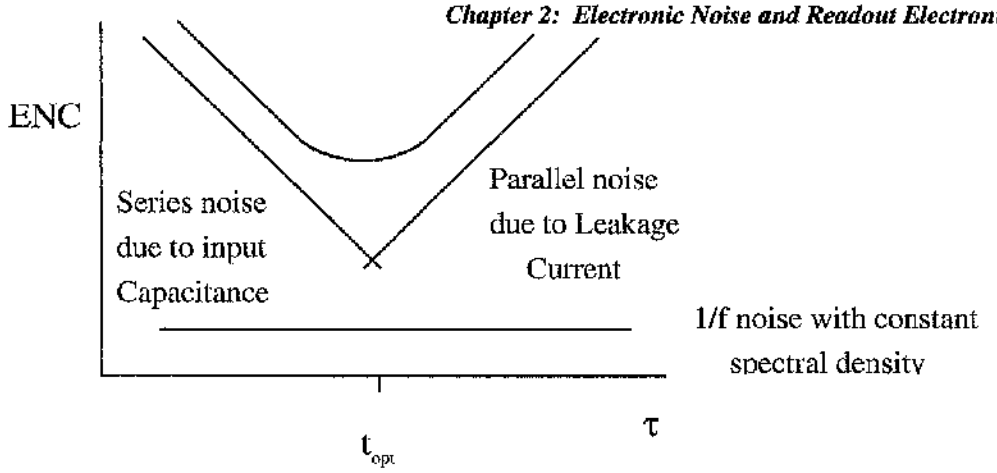

Fig.2.3. A typical noise vs. shaping time graph, showing the contributions from the various sources of noise.

The noise for any particular amplifier/shaper/detector configuration can be calculated and measured with reasonable agreement, when only the white noise sources are present. In reality, it is almost impossible to realise a triangular shaping circuit and keep the component count in the circuit to a reasonable level. The most common form of shaping used in modern semiconductor detectors is based on variations of RC-CR differentiation and integration stages, as these circuits are easily combined with amplifier stages and read out registers. The designs are then produced as VLSI circuits on silicon which are relatively easily bonded to the detector elements with minimal addition of capacitance to give an optimised read out circuit. Each circuit is normally optimised for its particular application in terms of shaping time and output format. A more complete description of each type of read out chip will be given when the results obtained with it are discussed.

2.3 Signal-to-Noise Ratio and 'Excess' Noise

Whether a particular signal resulted from the passage of a particle through the detector or from a random noise pulse is determined with a certain level of confidence using a figure of merit known as the "signal-to-noise ratio", S/N, where S is the most probable value of the signal and N is the rms value of the noise.

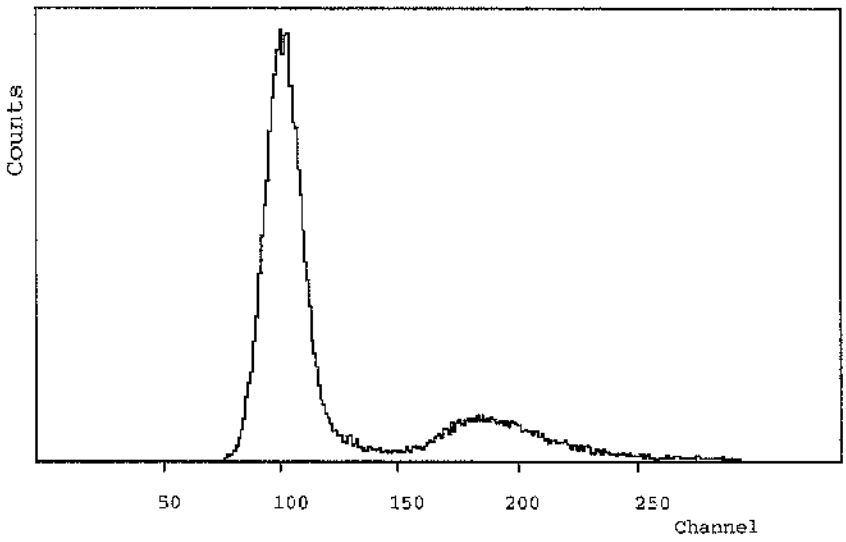

Fig.2.4. A typical spectrum of a MIP energy loss distribution and a gaussian noise pedestal.

In the detectors used for this study, signal spectra like that shown in Fig. 2.4 were obtained using "minimum ionising particles" from a radioactive source (usually Sr^{90} or occasionally Ru^{106}). These sources produce beta particles with a continuous energy spectrum which has an end point energy characteristic of the isotope (β- decay). The end points for ruthenium and strontium are 3.5 and 2.2 MeV, respectively, and those beta particles in the high energy portion of the spectrum are classed as minimum ionising particles (MIP's). As shown in the previous chapter, the energy loss of traversing MIP's is described by a Landau distribution. In detector characterisation tests the measured signal height as a function of applied bias determines the amount of signal charge extracted from the detector.

The ratio of this charge to the total charge created in the detector gives a measure of the charge collection efficiency of a particular detector. In GaAs this rarely reaches 100%. The charge deficit is due to the presence of traps in the material which prevent all of the free carriers from reaching the collecting electrodes of the detector within the integration time of the amplifier. It has never been possible to explain exactly how this occurs but it is thought to be a mixture of trapping/de-trapping and a modification of the internal electric field of the detector which leads to low field regions and inactive areas in the total 'depleted' width. This question will be dealt with in greater detail in the next chapter.

The observed incomplete charge collection leads to the question 'Is it uniform?' The general detector test uses 3 mm diameter pads with guard rings and so very small localised differences in performance could easily be averaged out. Indeed, this was noted

in early tests by M^{c}Gregor et al. [20] who observed a variation in performance of diodes of various sizes. Nava et al. [21] also showed recently that the collection efficiency varied as a function of illumination position when samples were probed with a proton micro-beam. Until recently the smallest pixel size that could be read out in any reasonably large array was 50x500 μm^2. The variation in performance at this pad size does not appear to be a problem. Recently, however, a 240x320 array of 38x38 μm^2 pixels has been designed and fabricated in Glasgow by the author. Using uniform illumination from an X-ray source, it seems that there are very localised variations in the charge collection efficiency shown in Fig. 2.5.

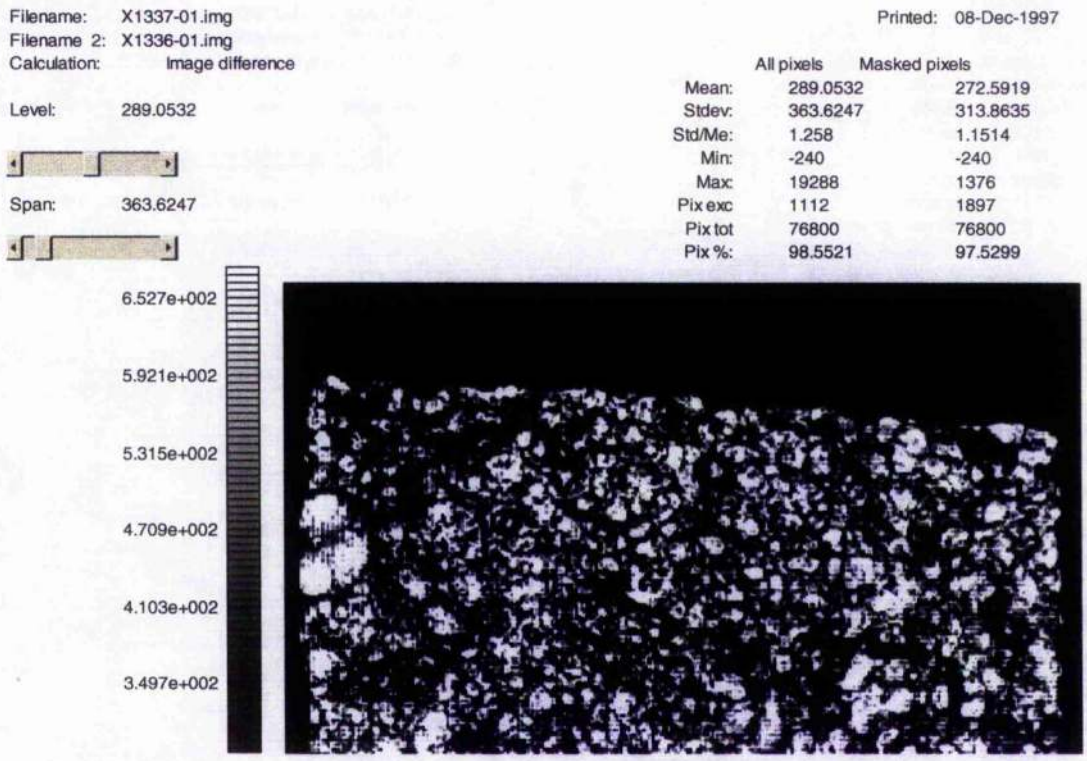

Fig.2.5. Image obtained using a 38 μm square pixel array fabricated on a 200 μm thick LEC GaAs wafer and read out with a charge integrating circuit on each pixel. The array was illuminated with a uniform flux of X-rays from a 70 kV dental X-ray set with a lead sheet placed across a fraction of the array giving the black region at the top.

The portion covered by the lead sheet in the image above shows that the leakage current is not responsible for the variations in the image. There is, however, a variation of a factor of 2 in the charge collection across very localised areas in the crystal when illuminated with X-rays which would be difficult to see in tests of larger area pixels.

This localised variation in charge collection efficiency leads to a type of 'excess' noise in spectroscopic measurements using GaAs. If illuminated with a mono-energetic source, for example, the output from the detector will depend on the particular region of the

detector in which the particle/photon created its charge. The output will be smeared by this variation of charge from area to area and peaks in the pulse height spectra will be broader than they would be with 100% charge collection as seen in Fig 2.6.

The width of peaks in spectroscopic measurements can be very accurately predicted once one knows the energy of the peak and the rms width of the Gaussian "pedestal" noise distribution when there is no charge deficit. Bertuccio et al. [22] have demonstrated that there is indeed an excess in the peak widths seen in spectroscopic measurements even when all the relevant parameters have been taken into account.

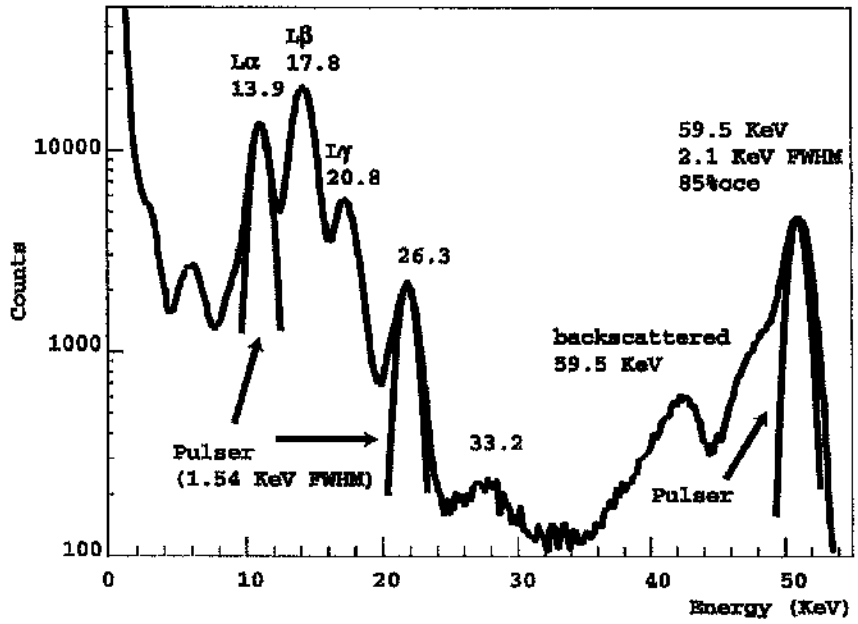

Fig.2.6. A spectrum of Am241 gamma-rays in a 100 μm thick, 3 mm diameter pad detector with 85% charge collection efficiency showing the absolute noise width as determined with a pulser as well as the predicted peak width and the excess noise.

2.4 Read-out Electronics Used in Testing Pad and Microstrip Detectors

For evaluating GaAs diodes a variety of amplifying circuits has been used in pursuit of various goals. In what follows, an outline is given of the types used at different stages of this study, why they were used and some of the difficulties encountered.

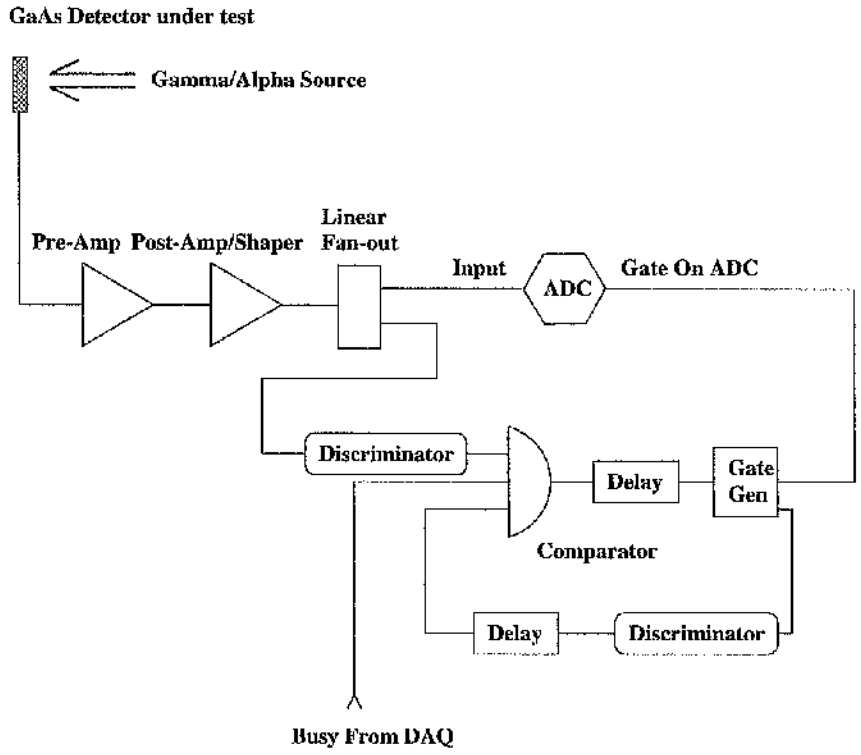

Fig. 2.7. Standard test set-up for measuring response of detectors to alpha and gamma sources. MIP tests were done with a slightly modified set-up.

All of the testing on standard 3mm diameter pads was carried out using an Ortec 142 pre-amp followed by an Ortec 485 amplifier/shaper which is normally set up with a shaping time of 500 ns. The pre-amp is made of discrete components and sits inside a shielded box. This is the set-up best suited to testing large numbers of relatively large structures which are mounted on standard test jigs for easy connection. The performance of the test set-up, with a typical ENC of 650 electrons rms for the test pad, is perfectly adequate for the accuracy required in the bulk of our measurements. The set-up is as shown in Fig. 2.7 and is used to read out the CAMAC ADC to a Macintosh computer using a software package called MACDAQ written by Federico Cindolo [23].

The first micro-strip detectors in a test beam were read out with the AMPLEX chip [24], a 32 channel charge amplifier/shaping circuit with a sample-and-hold circuit on each channel connected to a parallel in / serial out analogue shift register. The AMPLEX had, as a design feature, the possibility of reading out any particular channel as an un-sampled analogue stream. This facility was to prove extremely useful. (The read-out chips were given to us by Pierre Jarron and Giorgio Stefannini and the read out driver was loaned to us by Claus Gößling.) The AMPLEX was a type of "half-way house", in terms of read-out density for tests of microstrips with strips of 500 μm pitch for use in a proposed

preshower/tracker for the EAGLE [25] experiment. The strips were bonded onto kapton 'cables' and thereafter onto a printed circuit board which contained the read-out chip. While this arrangement did not lead to the minimal noise performance for our GaAs detectors it did provide an opportunity for a direct comparison with silicon detectors, which was one of our objectives. The first results for GaAs double-sided detectors, also taken with this set-up, will be discussed in more detail later.

As ever higher density of read-out electronics became necessary for smaller pitch micro-strip detectors, the read-out evolved to use, firstly, the MX3 chip and later its successors the MX5, 6 and 7 [26]. These chips were designed at RAL and have been used successfully to read out 3 of the 4 LEP experiments' silicon vertex detectors. Each chip has 128 channels and uses the principle of auto-correlated double sampling [29] in which 2 samples separated by a fixed time interval are used to optimise the noise performance. Both samples are then read out using two analogue shift registers as shown below in Fig.2.8.

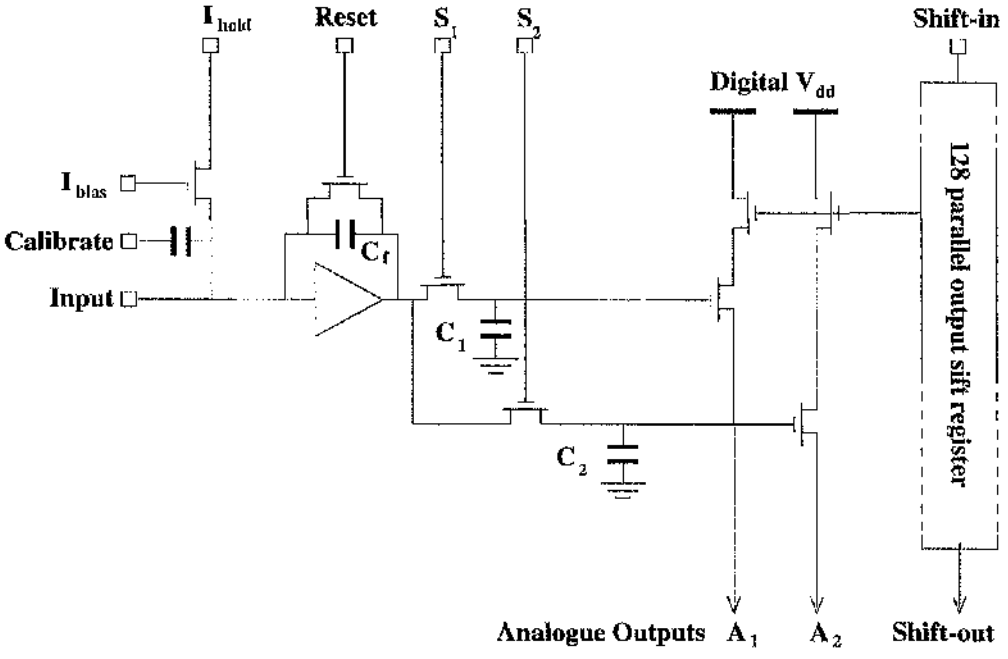

Fig.2.8. A schematic representation of the configuration of the MX series read-out chip.

The timing is adjusted so that one of the samples occurs at the peak of the signal and the second occurs after the signal. Subtraction then yields a signal which has a much

improved immunity to common-mode noise. The MX7 chip had excellent noise performance, (ENC = 320 e- + 20 e-/pF rms [30]), but it was extremely difficult to use where the S/N was low as there was no facility to observe the analogue signal from the detector. The correct adjustment of the timing was extremely difficult. In our test beam experience the data obtained with the MX variants were never optimised and usually obtained by painful and time-consuming scanning of the timing parameters. For this reason we changed our read-out to incorporate a read-out chip that offered the possibility of observing the analogue signal.

This type of read-out circuit, called the VIKING and a derivative series of devices known as the VA family [31] offered similar performance to the MX series. The chip consisted of 128 channels, each with a charge amplifier and RC-CR shaping followed by a read-out shift register as shown in Fig. 2.9. The shaping time was variable between 500 ns and about 3 μs and it was possible to look at the analogue signal on each channel for diagnostic purposes. This read-out chip was used predominantly to read out the high precision silicon micro-strip telescopes developed for test-beam work at this time and was therefore a logical choice for our GaAs detector tests. The noise performance of the VA series is markedly superior to any other commonly available system that operates at the same speed.

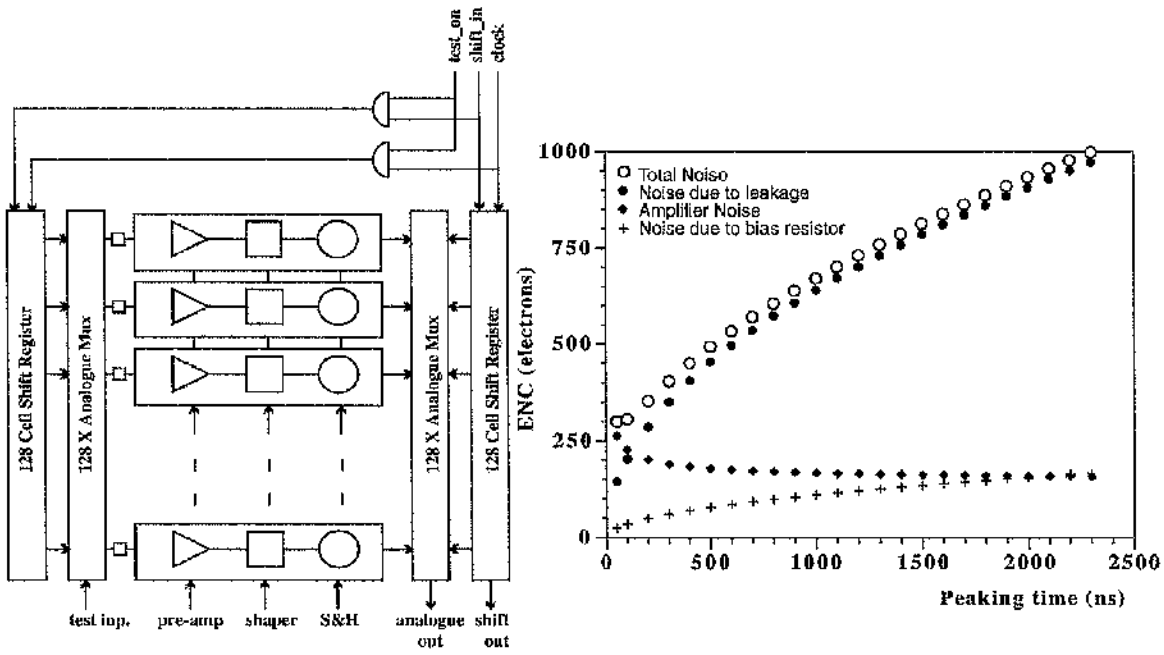

Fig.2.9. A schematic of the VIKING circuit on the left, as well as an illustration of its noise performance as a function peaking time for a 1.5 pF load capacitance and a 50 MΩ bias resistor.

2.5 Pixel Detector Read-Out Electronics

The final type of read-out electronics to be discussed in this section differs fundamentally from those previously described. All of the above circuits were used to read out long, closely spaced micro-strips. These elements have a high definition along one co-ordinate axis only and each element is, in general, wire bonded to the read-out channel. As part of the LAA project funded by the Italian Government [32], (which also funded initial work on GaAs detectors), a sub-project was initiated on the study of "micropattern detectors". From this work a whole range of pixel detectors for HEP applications has emerged [33].

The principal difference in these pixel detectors is that the detection element is relatively small in two dimensions but does not necessarily have to be square. In High Energy Physics (HEP) it is usually the case that there is a need for high resolution in one dimension only, due to the configuration of a magnetic field. In this case rectangular pixels with a fine spatial definition along one axis and a coarser one along the other are exceedingly useful. A number of technological difficulties needed to be resolved in order to make these pixel detectors feasible. The principal problem was the connection between the read-out channels and the detection elements. The bump-bonding, or 'flip-chip', process had been developed by IBM [34] in the 1970's and then abandoned as there was little demand for the technology at the time. This was the ideal interconnection method for pixellated detectors as it was a truly two-dimensional interconnect that lent itself easily to the processing of large, very regular arrays. In the late 1980's, the development of the Multi-Chip Module technology brought the use of bump-bonding back into demand. The principal difficulty remaining was that the minimum pitch used by the majority of commercial processes was far too large for HEP detectors. The pixels dimensions required for HEP were 75x500 μm^2 and bumps of the order of 20 μm diameter were then required to implement a successful process. It is obvious that, in this technology, the size of the detector element can be no smaller than the size of the read-out element that sits on top.

A flip chip process existed at GEC-Marconi Materials & Technology (GMMT) Caswell Laboratories [35] which could be adapted to meet the HEP requirements. The process involved depositing a thick layer of solder on concentric rings of wettable and non-wettable metals. When the solder reflowed the surface tension of the liquid solder pulled the liquid away from the non-wettable metal into a hemi-spherical shape sitting on top of the wettable metal. This process was easily implemented for large arrays using a machine that was capable of aligning the chips to be bonded with satisfactory accuracy.

The first read-out chip to be designed for a pixellated detector was known as the OMEGA chip [36]. The cell size was 75x500 μm^2 and the array was organised as 16 columns, each of 64 rows, giving 1008 read-out elements per array. One cell from each column was used to sense the average leakage current of the cells in that column and adjust the biasing of the amplifier to provide minimal offset. Each cell was organised to give a digital 'hit' in response to a signal above an externally set threshold. This 'hit' was then stored in a register and could be read out upon receipt of a suitable trigger. The circuit schematic is shown in Fig. 2.10.

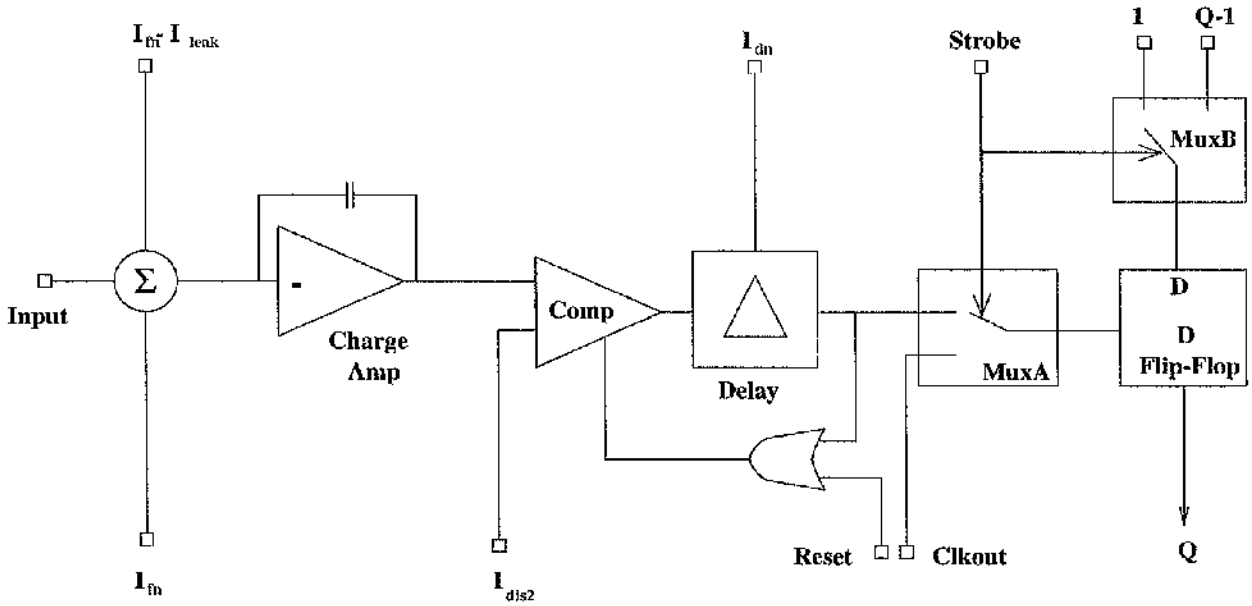

Fig.2.10. Electrical schematic of the cell design for the Omega chip.

The type of strobe required for the OMEGA meant that it could not easily be used for measuring radiation that did not traverse the detector to produce an external trigger. After discussion with Saverio D'Auria, we proposed to obtain a trigger from the back contact that could be used to run the chip in an asynchronous mode and enable efficient photon counting. This proved a very successful method for measurement of gamma-ray spectra and led to the proposal for a photon counting chip (MEDIPIX) which has recently been brought to fruition.

The OMEGA family has undergone several iterations to refine the design and correct undesirable effects such as threshold variation across the chip. The latest design, known as the LHC1, has a cell size of 50x450 μm^2 and is capable of running at the 40 MHz speed required for the latest HEP accelerator, known as the Large Hadron Collider (LHC) [37], now being constructed at CERN. The threshold variation has been reduced so that the minimum useful threshold is now ~ 2500 e^- (previously ~ 4500 e^-). Despite considerable study, however, the bump-bonding process has remained somewhat inconsistent and is a source of continuing concern.

The triggering requirements of the OMEGA family and the pixel shape do not lend themselves readily to imaging in any conventional application. In order to address such applications, the MEDIPIX chip design uses the amplifier/shaper and discriminator cells from the LHC1 and has a 15-bit counter instead of the registers used for HEP read-out applications. The chip is organised as an array of 64x64 cells each 170x170 μm^2 giving an active area of about 1 cm^2. The threshold variation has been further reduced to ~ 1500 e^- rms by the addition of the facility to adjust individually the last 3 bits of an 8 bit comparator threshold on each cell. First prototypes of the chip were delivered and tested during the summer of 1997. A more detailed description of the chip and of potential improvements that might be realised with it, is given in Chapter 5.

The last type of read-out chip to be described has been developed for Infra-Red imaging using QWIPS (Quantum Well Infra-red PhotodetectorS) [38]. It is made up of an array of 320x240 cells each 38x38 μm^2 in area. The design has been realised at IMC, Stockholm and the read-out principle uses a current integration over a certain time interval for each pixel. This is much more easily realised than the requirements for a true photon counter as the former needs just a capacitor and some switching transistors as shown in Fig. 2.11. It is for this reason that such a small pixel size can be achieved. A potential problem arises with an integrating read-out if the leakage current of the detection element is large. The leakage current uses up the charge storage in the read out circuit. This reduces the amount of storage that is available for charge created by the radiation. Compatible detectors were designed and fabricated on LEC material by the author in early 1998. They were bump-bonded to their read-out circuits by IMC, using indium bumps and successfully tested with X-rays recently. These results are described in Chapter 5.

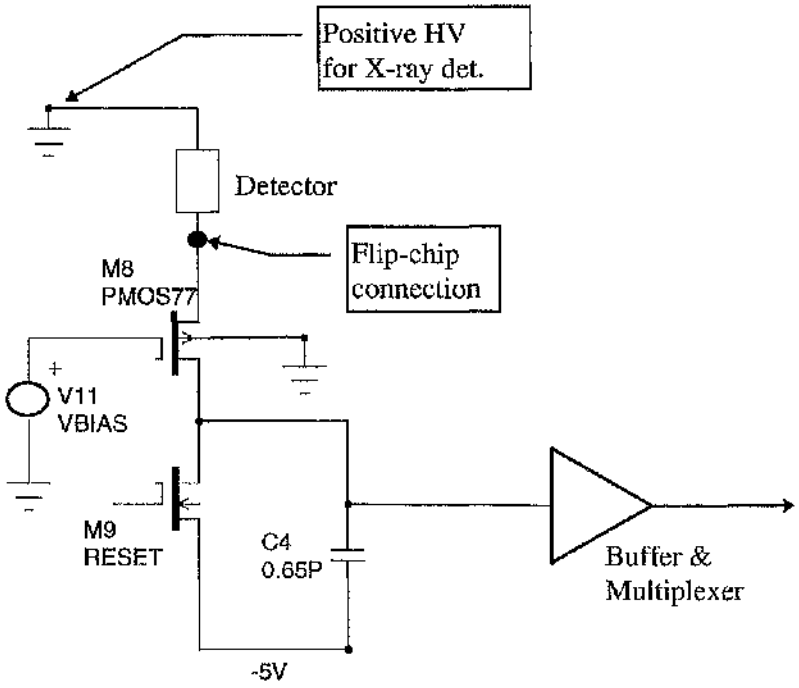

Fig.2.11. Basic configuration for an integrating pixel readout cell.

Chapter 3: GaAs Detector Fabrication and Characterisation.

3.1 Introduction

In this chapter a description is given of the work that has been done in developing the processing and testing of pad detector structures at Glasgow by the author. There follows a discussion of the test results and their impact on the models being proposed to explain the observed phenomena.

3.2 Detector Design

The features that are important for the optimum design of detectors depend very strongly on the processing steps to be carried out and the fabrication facilities available. The first detectors were made in Glasgow by evaporating contacts through a shadow mask cut from a sheet of brass. The design and processing of detectors has subsequently been developed in Glasgow by the author to the point where 3 μm feature sizes are routine and there is the possibility of a second metal layer as well as air bridges.

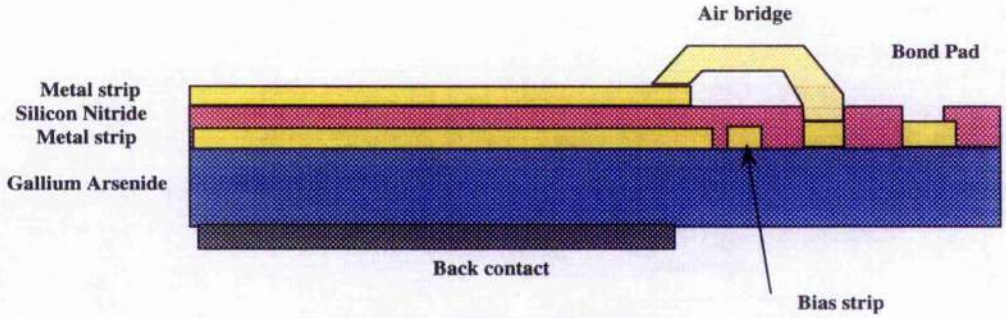

Dielectric: Silicon Nitride

Air bridge

Punch-through biasing structure

Fig.3.1. A cross-section of an AC-coupled microstrip detector using punch-through biasing and air bridge technology to avoid high field potential breakdown regions when reading out the second metal.

The cross-section shown in Fig. 3.1 illustrates the structure complexity. Although not obvious from the illustration, it should be noted that both sides of the material are patterned and the alignment must be maintained through the material. The design requires up to 7 mask layers to implement the most complex patterns, the air bridge using 2 masks. It must be said at this point that the design of GaAs detectors is relatively simple in comparison to those in silicon as there are no implantations or diffusions. There are, therefore, no doping profile changes to worry about as a consequence of thermal treatments at later stages of the process.

The mask layout for all the detectors designed at Glasgow has been carried out using Wavemaker, a software design package developed by Barnard Microsystems Ltd. [39]. This software permits the layout of multiple layers with a spatial precision of a nanometer (our minimum feature size is 3 μm). The design is stored in a format known as GDSII, which is compatible with the input format required by the electron beam-writer, which is then able to interpret the layout and write a mask for each level. The beam-writer that we use in Glasgow is a 10MHz Philips EBPG5-HR machine which is capable of writing with a 12.5 nm beam spot over a 1.6 mm square and "stitching" adjacent squares together with an accuracy of about 15 nm. The pattern can be written over a 4x4 inch area but the machine can take mask plates up to 6 inches square. The designs we use for detectors do not require this accuracy but this is the standard machine used for mask writing.

Initially devices were processed on sections of wafers but as the complexity of designs grew and there was a requirement to use material that had been thinned and polished to 200 μm it was eventually decided that only complete wafers should be processed. This meant that it was possible to have a standard set of test devices that would be processed on every wafer, providing a means of comparison from run to run and between different materials.

Our standard structures for characterising performance consist of a series of 3 mm diameter diodes, a structure comprising an array of gaps with different aspect ratios to determine the punchthrough voltage and a series of strips with 50 μm pitch, having different length and separation which permit one to measure the interstrip capacitance. Aspects of the design of these structures are shown in Fig. 3.2.

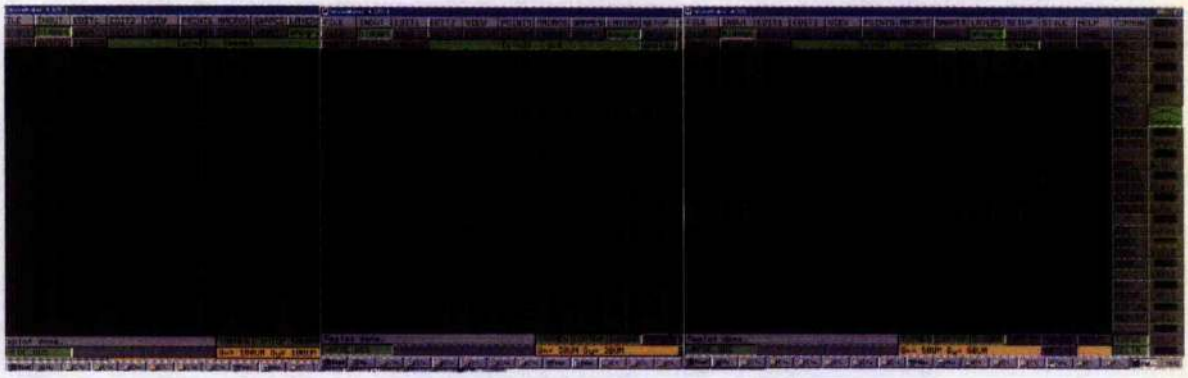

Fig.3.2. Details from the designs for test structures from l to r. a) 50 μm pitch strips of 3 different lengths and separated by 10, 25 and 40 μm. b) design of air bridge structure with a punchthrough bias structure running underneath. c) detail from the test structure used to evaluate punchthrough.

Once a design has been produced for a particular structure or series of structures, the patterns are then laid out so that they cover an entire wafer. For day to day processing in Glasgow 2 inch wafers are preferred but detectors have been produced on 3 and 4 inch wafers when needed. A layout for a 2 inch wafer is shown in Fig. 3.3:

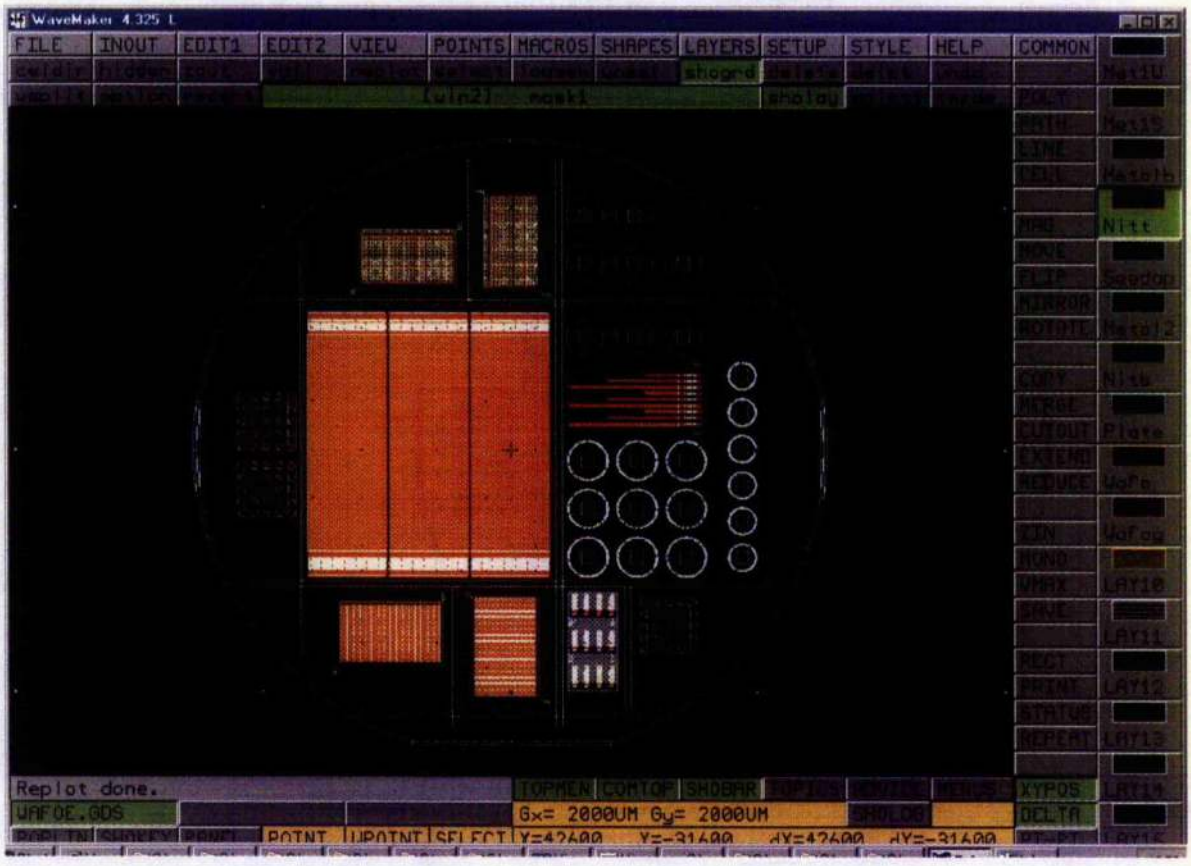

Fig.3.3. Layout of a 2 inch wafer of microstrip detectors, a variety of pixel detectors and a series of test structures.

It is important to note that the masks used for either side of the detector must be written as mirror images as there is an image inversion when looking through the detector material. In the lab it is much easier to align multiple stages using ferric oxide masks as it is possible to see through them. Most of our mask sets are written on a chrome plate and then copied onto ferric plates which is another mirroring stage.

3.3 Thinning and Polishing of GaAs Wafers

The wafers used for internal processing are bought from our preferred supplier, Wafer Technology Ltd., "as cut" and we specify that they should not come from the first or last 100 slices of the boule as we have found that these specifications give the most reproducible detector results. The wafers are bought as cut because we polish both faces chemically in the same way. The standard thickness for a 2 inch wafer is 450 μm. The conclusion of a study of various strategies for polishing the wafers to a final thickness of 200 μm is that the best method is to remove 220 μm with a precipitate of 0.3 μm powdered Al_2O_3 in de-ionised water. The wafer is waxed onto a flat quartz plate and its thickness measured with a Mitutoyo micrometer. It is then placed under a calibrated load on a LOGITECH PM4 polisher with a speed about 30 rpm. This setting removes about 8 μm per minute on a 2 inch wafer.

When the mechanical stock removal is complete, a chemical polish is performed on the same machine using a solution of H_2O_2/NH_4 with a pH of 7.8 +/- 0.1. It has been found that if we remove 15 μm and achieve a good mirror like surface, all the lattice damage that has been caused by the aggressive mechanical polish has been removed. Detector fabrication and performance on material that has been prepared in such a way has been found to be both satisfactory and repeatable. The leakage current of contacts made on material prepared in this way can be reproduced consistently while the charge collection efficiency improves from ~ 60% for devices made from material as-supplied, to almost 100% [116]. This recipe evolved from work carried out in conjunction with Logitech and the Dept of Chemistry [40].

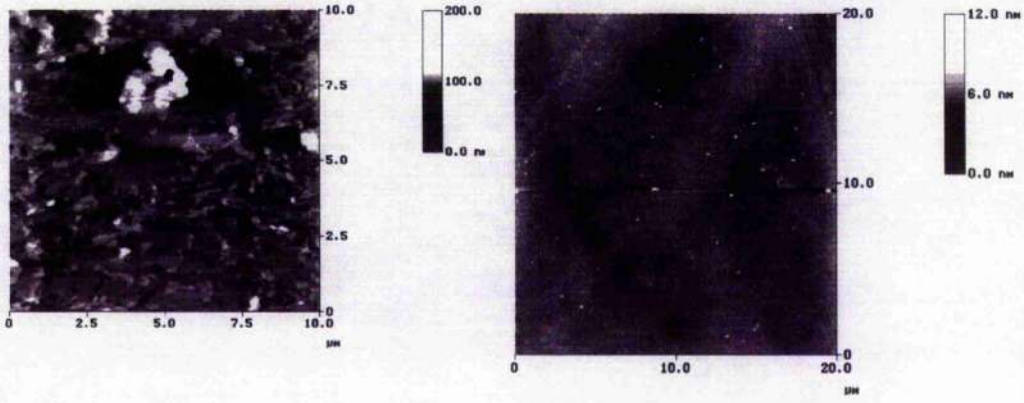

Fig.3.4. Surface smoothness of a section of an as-supplied polished wafer on the left and a Glasgow polished wafer on the right as seen by an Atomic Force Microscope [41].

3.4 Detector Fabrication

The thinned wafers are transported to the clean room and cleaned according to a standard procedure as follows:

1 minute ultrasonic bath in each of the following in order – opticlear – acetone – methanol – De-ionised (D.I.) water.

This procedure is used prior to every application of photoresist. The wafer is then placed on a Headway Research Inc. photo-resist spinner and some drops of primer are spun on at 4,000 rpm for a few seconds. It is especially important to use primer in the present clean room as there is not enough humidity control and humidity can have a deleterious effect on the adhesion of the photoresist. The photoresist is then applied in drops so that there is a uniform film over the wafer surface and is then spun at 4,000 rpm for 30 seconds. The resist normally used for simple metallisation and aperture definition in insulators is Shipley S-1818, which is a positive resist formulated to give a film thickness of 1.8 μm for the spinning conditions described here.

The wafer is then baked in an oven at 90°C for 30 minutes. For a lift-off metallisation process step, the wafer is removed from the oven after 15 minutes and soaked in Chloro-benzene for 15 minutes and then returned to the oven for the final 15 minutes. This soak hardens the outer skin of the resist film so that on the developed pattern there is a slight overhang of this outer skin which prevents the evaporation of a continuous metal film and therefore aids the lift-off [42]. The wafer is now ready for exposure and the desired mask

is placed in the mask aligner. The wafer is offered up to the mask, the alignment is made and then hard contact is made between the mask and the wafer. A further check is made to ensure that the alignment is correct and the resist is exposed. In the case of the S-1417, 12 seconds is the correct exposure time for this machine.

The wafer is now placed in a 50:50 mixture of water:developer for 75 seconds after which the pattern should be fully developed. It is optically inspected at this point to ensure that the pattern has been satisfactorily transferred from the mask to the wafer. If this is not so, the wafer is rinsed in acetone and the procedure starts again. The wafer is now ready for metallisation. It is rinsed for 30 seconds in a 50:50 D.I.:HCl solution to deoxidise it and then quickly placed in the vacuum chamber of the evaporator.

The preferred evaporator for all of our standard recipes is a Plassys MEB 450. In the vacuum chamber it has an electron beam cannon and a rotating crucible with a choice of 6 metals. The process is fully automated and once a recipe has been formulated it can be implemented thereafter at the press of a button. The standard top and bottom contacts used for simple diode processing are shown in Fig. 3.5.

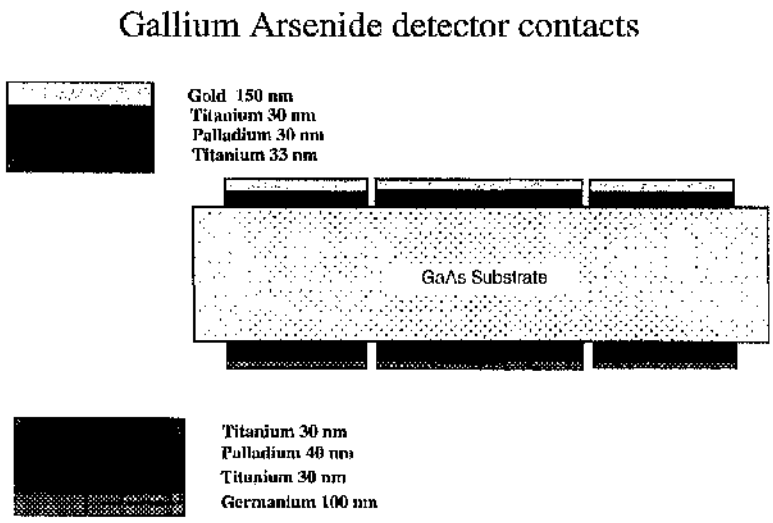

Fig.3.5. A cross-section of a pad detector showing the annular guard ring on the outside as well as the metal layers that make up each contact.

After the metal deposition, the wafer is removed and gently washed in acetone until all the resist has dissolved and the metal from the evaporation on top of it washed away – this is the lift-off. The metal that has been evaporated onto the substrate through the apertures in the photoresist remains on the substrate surface. When the lift-off is complete the wafer is rinsed in D.I. and gently blown dry with filtered air. Directly after each

is placed in the mask aligner. The wafer is offered up to the mask, the alignment is made and then hard contact is made between the mask and the wafer. A further check is made to ensure that the alignment is correct and the resist is exposed. In the case of the S-1417, 12 seconds is the correct exposure time for this machine.

The wafer is now placed in a 50:50 mixture of water:developer for 75 seconds after which the pattern should be fully developed. It is optically inspected at this point to ensure that the pattern has been satisfactorily transferred from the mask to the wafer. If this is not so, the wafer is rinsed in acetone and the procedure starts again. The wafer is now ready for metallisation. It is rinsed for 30 seconds in a 50:50 D.I.:HCl solution to deoxidise it and then quickly placed in the vacuum chamber of the evaporator.

The preferred evaporator for all of our standard recipes is a Plassys MEB 450. In the vacuum chamber it has an electron beam cannon and a rotating crucible with a choice of 6 metals. The process is fully automated and once a recipe has been formulated it can be implemented thereafter at the press of a button. The standard top and bottom contacts used for simple diode processing are shown in Fig. 3.5.

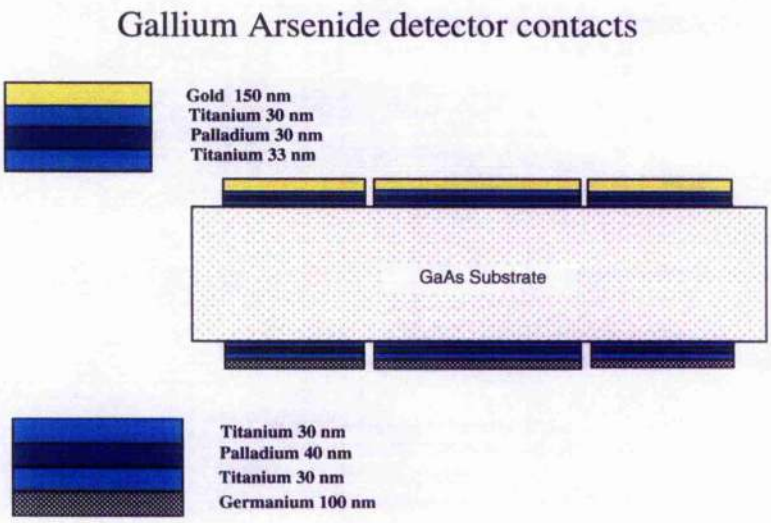

Fig.3.5. A cross-section of a pad detector showing the annular guard ring on the outside as well as the metal layers that make up each contact.

After the metal deposition, the wafer is removed and gently washed in acetone until all the resist has dissolved and the metal from the evaporation on top of it washed away – this is the lift-off. The metal that has been evaporated onto the substrate through the apertures in the photoresist remains on the substrate surface. When the lift-off is complete the wafer is rinsed in D.I. and gently blown dry with filtered air. Directly after each

metallisation is completed, the wafer is given a 200 nm thick cap of Silicon Nitride which serves to protect the surface as well as acting as an insulator for any other metal layers that might be required in the process. Even when there is only one metal layer, the nitride is still deposited as an encapsulant. The nitride layer is deposited using plasma enhanced chemical vapour deposition (PE-CVD) in an Oxford Plasmalab PD80 at a temperature of 320°C. A layer of 200 nm takes approx. 20 minutes to deposit.

The procedures outlined above are repeated for the other side of the wafer in the minimal device configuration. If no further layers are required, apertures are opened in the nitride using reactive ion etching in the following manner. The nitride surface to be etched is patterned in the manner described above and the exposed surface is etched by free radicals (chemically reactive ions) produced in a plasma. This is done in a Plasmatech BP80 using CHF_3, which etches nitride at a rate of about 30 nm per minute. The procedure is repeated for the other side and the wafer is then ready to be scribed and separated.

In only two instances to date has there been a requirement to add more metal layers to the device. In one case, where the device was a pixel detector intended for bump-bonding, the outer layer of gold is susceptible to leaching by the solder bumps. If the gold is totally leached away, the underlying layer of titanium is not wettable and so the contact may be lost. In order to reduce this possibility another layer of gold is evaporated over the aperture in the nitride. In the second instance, AC-coupled strip detectors had a read-out electrode deposited on top of the nitride and an air bridge fabricated from this second level metal down to external bond pads, as shown in Fig.3.1.

3.5 Air Bridge Fabrication

Reliable air bridges require two layers of resist separated by a thin skin of metal which provides the electrical continuity for an electroplating process to build up the bridge. The first step uses a different resist which gives a much thicker film when spun, as this will define the height of the "legs" of the bridge. The resist used is a Hoechst AZ4562, which gives a 6 μm film with a standard spin. This resist is baked in the normal fashion and then exposed for 20 – 25 seconds using a mask which defines the positions of the legs of the bridges required. The uncertainty in the exposure time is because it is necessary to overexpose slightly such a thick layer of resist and also it is necessary to over-develop the pattern so that the side walls of the legs have a shallow slope. This is a vital part of the

resist patterning as the bridges can only be successfully plated if there is a good electrical contact between the legs and the seed film.

The next step is to evaporate a thin seed layer over the whole surface of the wafer. This layer consists of 30 nm of titanium for adhesion and 20 nm of gold. It has been found that electroplating is not very successful on evaporated layers of gold and so a 10 nm layer of gold is sputtered on top of the evaporated metal. The seed layer is now ready to be prepared for plating. A layer of resist S-1818 is spun on top of the seed layer, baked for 30 minutes at 90°C and the bridges between the legs are exposed and developed. The wafer is then connected to the cathode and immersed in a gold-plating solution. A calculation based on the total volume of gold required, (surface area of each bridge times thickness required times no. of bridges), gives the current and the immersion time needed. For the bridges made in Glasgow, we aim for a thickness of 10 μm for bridges that are 100 μm long which gives good results.

After the plating has been completed, the upper layer of resist is gently dissolved in acetone. The seed layer may then be etched away with gold (potassium iodide) and titanium (hydrofluoric acid) etches. The underlying resist may then be washed away with acetone and the air bridges inspected visually. Fig. 3.6 shows some that have been used to decouple microstrips.

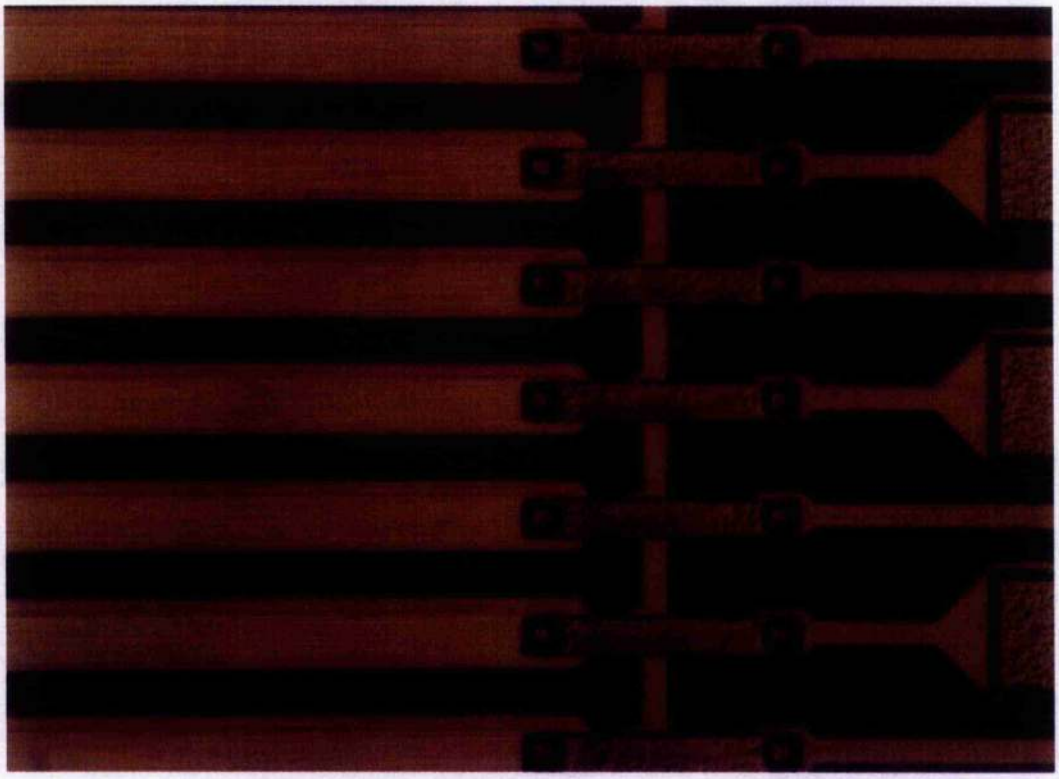

Fig.3.6. Airbridges used to read out ac-coupled strips on a GaAs detector.

3.6 Basic Device Characterisation

Each wafer has a number of pad diodes which are characterised as standard test pieces. Measurements are made of I-V and sometimes C-V characteristics over a range of frequencies and also of cce (charge collection efficiency) vs. applied bias. The I-V and C-V measurements use a Macintosh, using Labview to run a Keithley 237 for the I-V, as well as an HP-8137 for the C-V, both via a GPIB interface as outlined in Fig. 3.8. The C-V is a full 4-wire measurement, while the 237 has a guard output which is connected to a guard ring structure incorporated in the test devices. The space between the guard ring and the pad metal is 10 μm and the ring prevents surface leakage and also straightens the field lines underneath the pad, thus preventing lateral growth of the depleted region. The net effect of the guard ring may be seen in Fig. 3.7. The guard rings have provided a great improvement in the accuracy of the leakage current measurement

The information gleaned from the I-V and C-V data gives a qualitative comparison between diodes from different processes and/or different material. The barrier height can be extracted from the I-V characteristic and is a good indication of the quality of the contact metallisation. The C-V data are especially important when investigating supposedly high purity material such as epitaxial layers, as this measurement is used to observe how the depletion depth grows. The behaviour of the C-V characteristic at different measurement frequencies provides a qualitative indication of the presence or absence of traps in the material. The leakage current density for the standard diodes which we process normally has a value of around 10 nA per mm^2 but can vary by an order of magnitude for reasons that are not yet fully understood. This leakage current is two orders of magnitude larger than in silicon diodes. It is important to bear in mind that this leakage current does not all contribute to the shot noise in the devices [43]. The current generated by trapping/detrapping of carriers contributes to 1/f noise, and so the noise performance is better than expected from a straight-forward comparison of leakage currents.

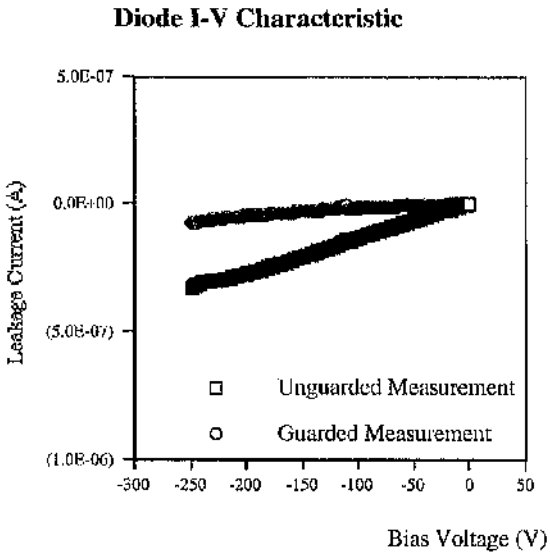

Fig.3.7. I-V characteristic measured with and without guard ring on a 3 mm diameter pad with a 10 μm separation from a guard ring. The brackets on the leakage current axis represent negative vales of current.

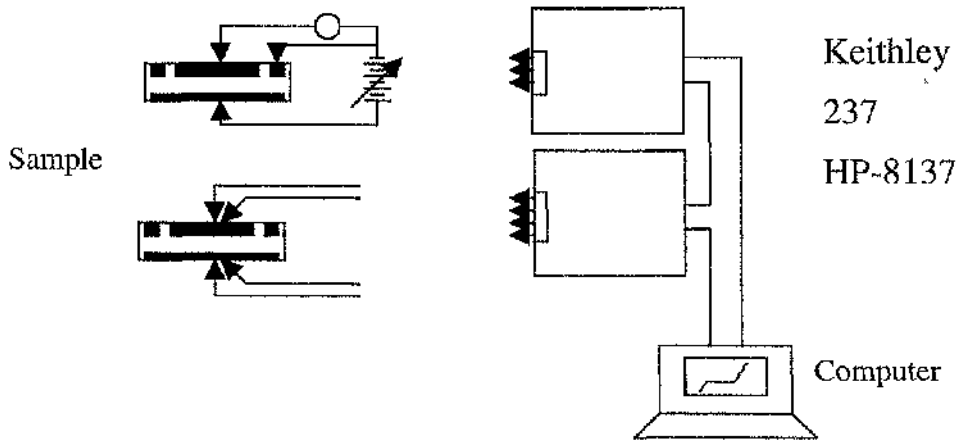

Fig.3.8. Outline of the measurement system and connections for I-V and C-V measurements.

The most informative of the standard tests for our detectors is a measurement of the charge collection efficiency as a function of applied bias. This measurement is carried out with alpha, beta and gamma illumination. Each deposits its energy differently in the crystal and therefore gives different information about the detector performance. The measurement with a beta source is performed using a silicon detector behind the test piece to trigger on the traversing particles and open an ADC gate with the appropriate delay. The acquisition is controlled by a software package called MacDaq and interfaces

to a CAMAC crate using a MacVEE [44] interface card. The ADC is a LeCroy 2259B with only one of the 12 channels normally used.

The test set-up is shown diagrammatically in Fig.3.9. The spectrum is both displayed on screen and saved to a data file for further analysis, if required. Typical spectra for MIPs and gammas are shown in Fig. 3.10 as they are measured by this set-up. For the acquisition of gamma spectra, the Si trigger is not used and the set-up is self-triggered from the GaAs detector by feeding its output through a linear fan-out and splitting it so that it triggers the ADC at some predefined threshold level. The only disadvantage of this method is that the pedestal is cut by the discriminator and must be added externally with the help of a pulser. This is the narrow peak that appears above the photopeak in the gamma spectrum. A similar arrangement is necessary for alpha particles as they are stopped in the first 30 μm of detector material.

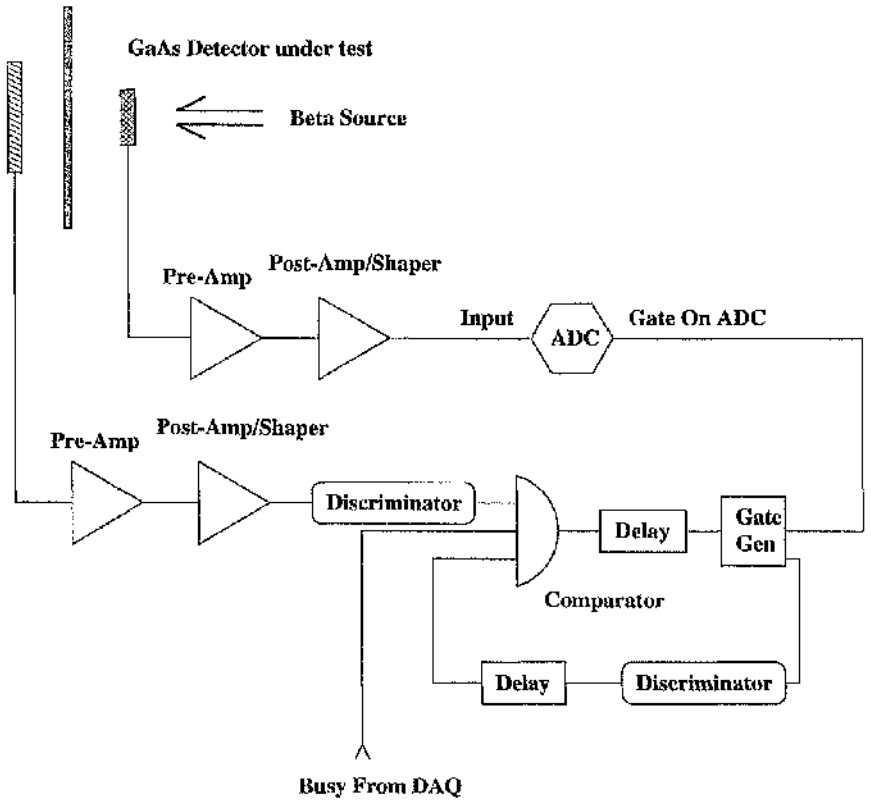

Fig.3.9. Triggered DAQ system for measurement of charge collection efficiency. The ADC values are readout to a computer via a CAMAC interface.

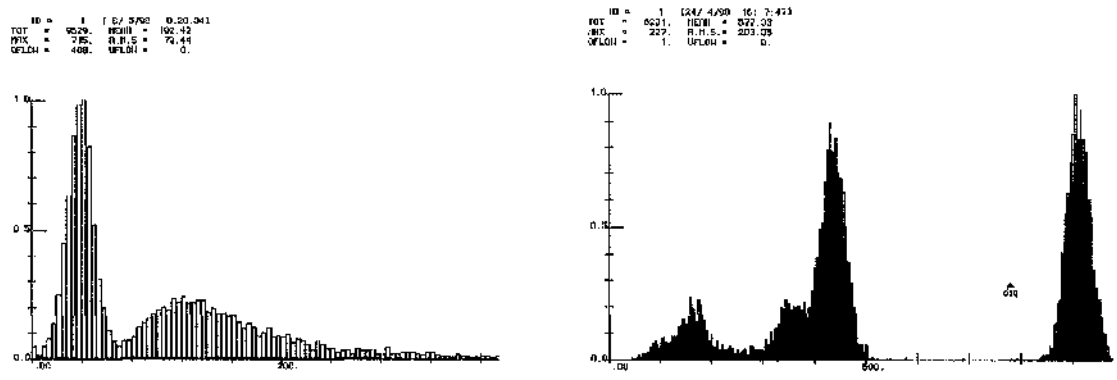

Fig.3.10. Spectra from beta and gamma measurements on a test diode. The pedestal is not included in the gamma measurement but a pulser is added to obtain a measurement of the noise.

3.7 Background and Results of Test Device Characterisation

Much work had already been carried out on GaAs as a detector material in the 1970's by Tavendale [45] et al, primarily for alpha and gamma detection with detectors made on a very high quality LPE epi-layers. The performance of these detectors was exceptional and material as good has not been produced again until quite recently. The development of detectors on LEC material began as part of the LAA project, initiated at CERN by the Italian government in 1987. The objective of the programme was to develop detection technology which would be suitable for use in future HEP accelerators, where it was foreseen that the high data rates and harsh radiation environment would render the technologies of the time unusable. One of the projects approved for LAA was the development of GaAs microstrips for use in the highest radiation, forward regions of new experiments [46]. The goal of the project was to develop these devices on the cheapest material available at the time, which was Liquid Encapsulated Czochralski (LEC). Previously LEC material had never been used to detect MIPs, which are difficult because of the low specific energy loss.

Initially the detectors were fabricated at the National Microelectronics Centre (NMRC) [47] in Cork, Ireland. The first detectors worked very well as alpha detectors but did not have a sufficiently high breakdown voltage to be able to look for MIPs. In the summer of 1989 we received sample diodes that had been fabricated in the Dept. of

Electrical and Electronic Engineering of Glasgow University. One of these samples, (KS10) had been thinned to 100 μm and held a bias of 120 V. Signals were obtained with a beta source but initially it was unclear whether the signals were from MIPs or from the lower energy particles also given off by the source. Using a plastic absorber and particles from both Sr^{90} and Ru^{106} it was established that the spectra obtained were indeed from MIPs. This is shown in Fig. 3.11 where it is clear that the peaks from Sr^{90} and from Ru^{106} lie in the same channel, even though the end point energies for these two sources are very different. The shape of the peak shows the Landau tail which is characteristic of the energy deposition expected from a minimum ionising particle. This was the first observation of MIPs in any kind of GaAs detector [48]. The much higher quality epi-layers were too thin to absorb enough energy from the traversing particles and so MIPs could not be detected above the noise.

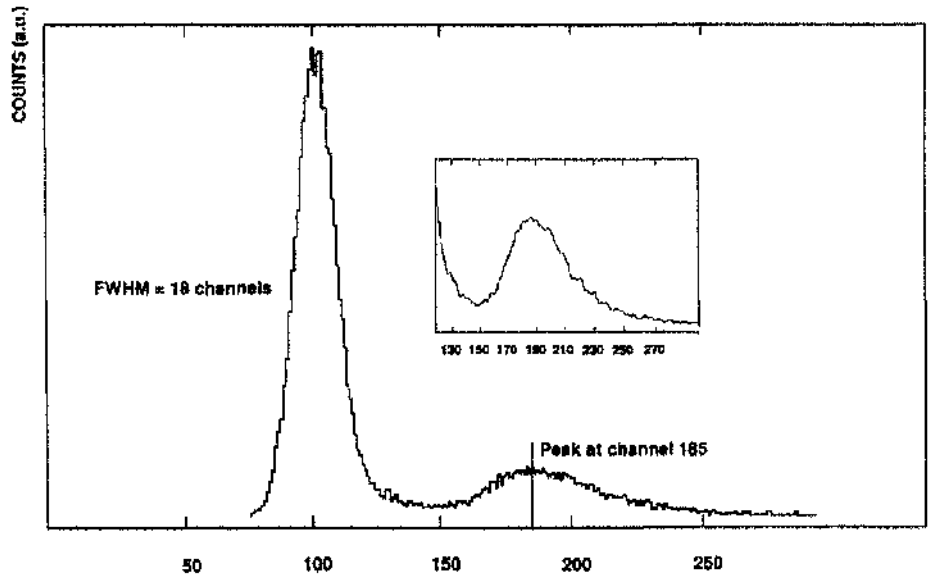

Fig. 3.11. Pulse height spectra in diode KS10, (100 μm thick, 120 V bias), from beta particles from Sr^{90} and Ru^{106} (inset), showing similar peak channels.

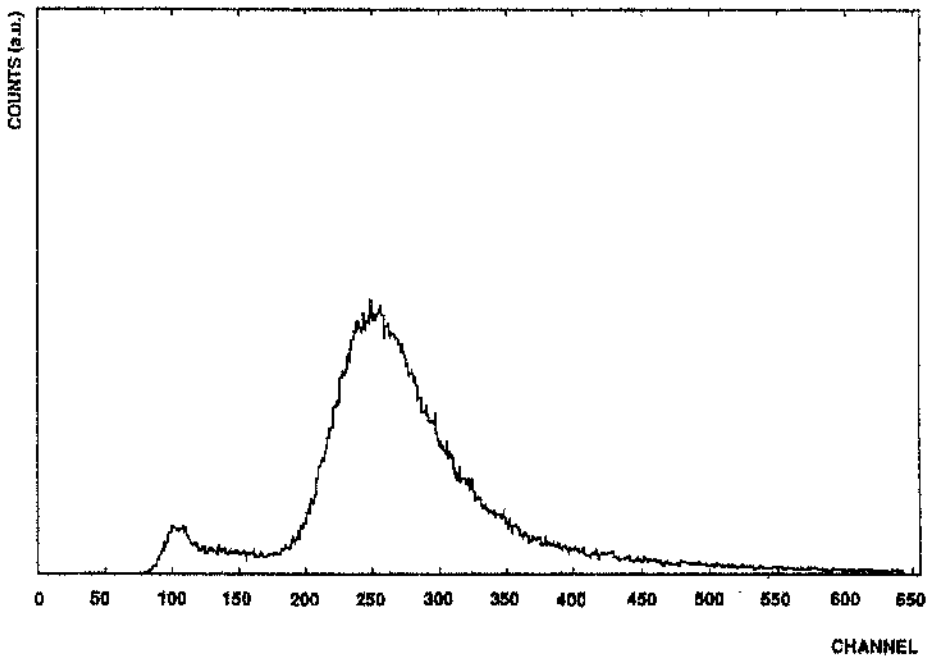

Fig. 3.12. The energy deposition of a 6 GeV/c beam of pions from the PS at CERN in a GaAs detector KS10 at 120 V bias. The Landau curve is typical for MIPs and the measured detection efficiency is greater than 96%. Any inefficiency is probably geometric in origin.

In the next step, the detector was exposed to a beam of high energy particles at CERN to confirm its detection of MIP's and to determine its efficiency. The pulse height spectrum shown in Fig. 3.12 is from the diode KS10 in a 6 GeV/c pion beam at the Proton Synchrotron, CERN. The trigger for this spectrum was implemented using a fragment of another diode which had similar properties. The data collected from the test beam confirmed that, although these detectors could see the MIPs, the charge signal collected by the detectors appeared to be only a fraction of the charge that should have been generated by the deposited energy.

A MIP should leave 56 keV (most probable value) for each 100 μm of GaAs [49]. The energy required to create an electron-hole pair in GaAs had been measured to be 4.2 eV [50]. When the electronics chain was calibrated, it appeared that only 50% of the liberated charge was collected. Measurements of the variation in charge collection efficiency showed that it had an almost linear dependence on the applied bias as seen in Fig. 3.13. This was not the behaviour predicted by the classical theory [51] and a thorough investigation of the possible causes was set in train (and is still going on).

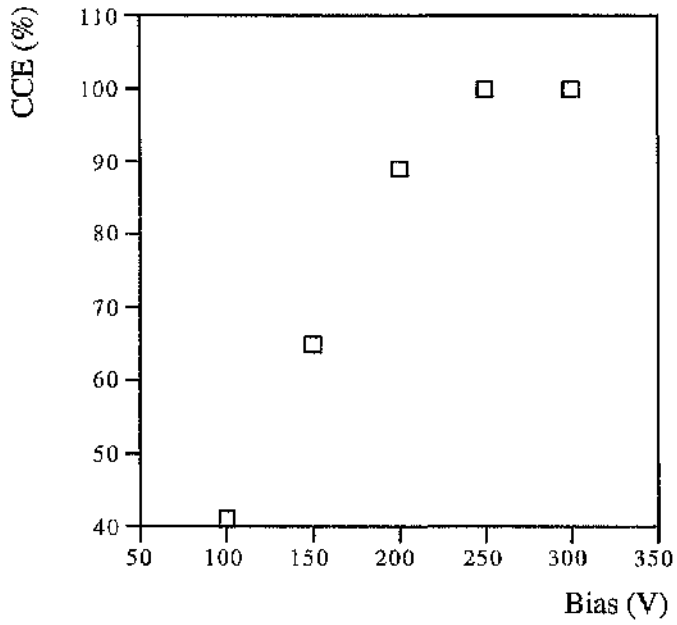

Fig. 3.13. The behaviour of charge collection efficiency (CCE) with applied bias. The linear increase indicates the presence of traps in the material.

The next problem was to isolate the many effects that contribute to creating a signal in the detector. The presence of traps in the crystal lattice means that there is practically no hope of simulating the electric field in the bulk for a realistic cocktail and concentration of expected traps. It was not obvious whether the material was depleting classically with the charge being linearly attenuated, or the growth of the depletion layer was modified by the presence of traps. It seemed that there were too many parameters and not enough methods to isolate each and therefore solve the problem. It became obvious that the 'standard' tests performed in the characterisation of "classical" semiconducting radiation detectors would be inadequate for the characterisation of LEC GaAs.

The use of differing types of radiation proved to be of paramount importance in unravelling this puzzle. It is useful, therefore, to review at this point some of the properties of different sources which could be of use. The energy deposition from alpha radiation is very intense over a very short range (22 μm in GaAs for 5.4 MeV alpha particles from Am^{241}). This distance is a small fraction of the total thickness of the detectors normally used. This means that illumination with an alpha source on a particular side of the detector determines the type of carrier that contributes predominantly to the signal -- if the detector is fully depleted.

The photoelectric conversion from X- or gamma-radiation is essentially constant over the entire detector volume. The total energy of the photon is deposited within a few μm's of the conversion point. This provides us with a measure of depletion depth which is

independent of any assumptions on the electric field in the detector volume, as the rate of counts in the photopeak for a given source-detector configuration depends on the active volume (depth) of the detector.

The α particles, X- and γ-rays are either totally absorbed by the primary detector or scattered in such a fashion that capturing spectra for these types of radiation requires the use of a random trigger with consequently low efficiency and poor ability to discriminate low S/N. Triggering on the signal of interest has the tendency to introduce a bias to the measurement. The MIP, on the other hand, passes through the detector and is available to produce another, independently produced trigger signal in a second, appropriately positioned detector.

The use of an electron microscope was proposed as another way of measuring active thickness. The GaAs detector was cleaved and placed in the microscope vacuum chamber with an attachment to the outside world to supply bias and examine the signals produced. The beam was focused on the cleaved surface and scanned across the depth of the detector at different values of applied bias. At this point, two possible methods of investigation were used. The first imaged the cleaved edge, showing the voltage contrast as a function of depth and applied bias. This method did indeed show qualitatively that there was a region of high electric field which showed up as a bright region which grew from the Schottky contact as the bias was increased. A second method was to scan the beam and look for a current signal on the diode output. This also indicated the presence of a 'dead' region in the diode. Although the information yielded by the microscope tests does not give a definitive answer, when combined with active depth calculations derived from rate tests with photons and charge collection efficiency measurements then it becomes apparent that the entire detector volume is not active, as shown in Fig. 3.14.

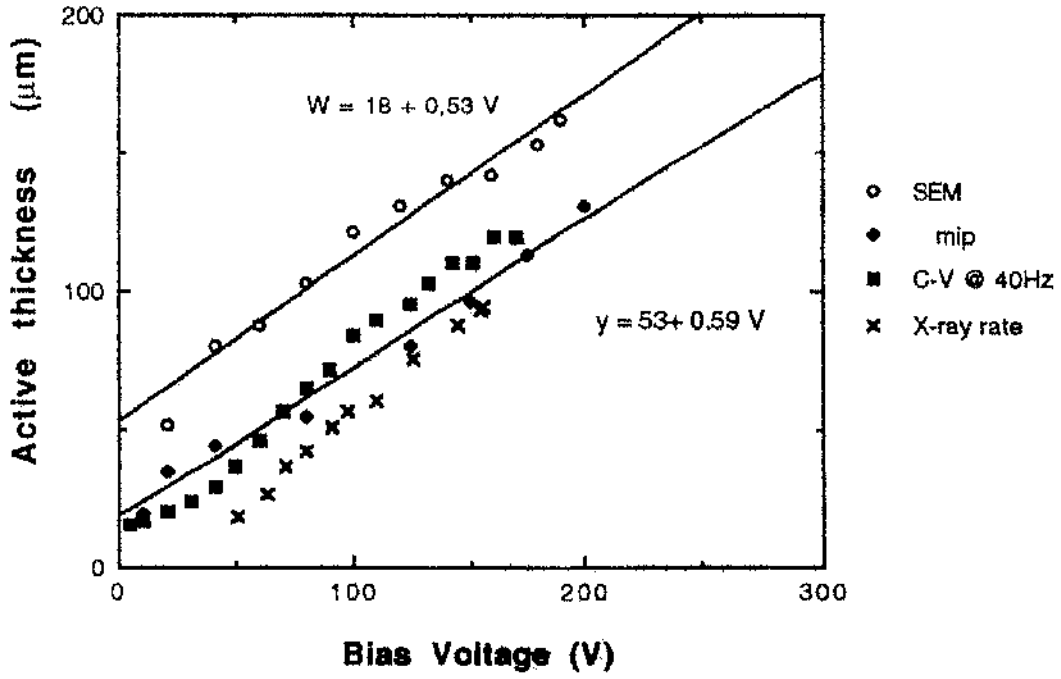

Fig. 3.14. The graph shows the measurement and reasonable consistency of different methods of measuring the active thickness of a detector.

Finally, if the capacitance of the detector is measured at a low enough frequency [52] the traps in the material have enough time to fill and relax and a C-V measurement gives an accurate reflection of the depletion depth or active width. The interesting aspect of the graphs shown in Fig. 3.14 is not the absolute value of depletion depth measured by any one method but the way that the region grows at roughly the same rate for all methods. The difference in absolute values is due to putting a threshold on the signal appearance on the SEM or the accurate measurement of the geometrical acceptance of the detector in the X-ray source set-up.

In an experiment carried out at UMIST [53] a cleaved diode 500 μm thick has undergone E-field profiling with a contact probe to ascertain the behaviour of the 'internal' field with applied bias. The result, shown in Fig. 3.15, indicates that there is a region of constant but relatively high electric field and a low field region. This is entirely consistent with the behaviour of the diode as deduced from the previously described experiments.

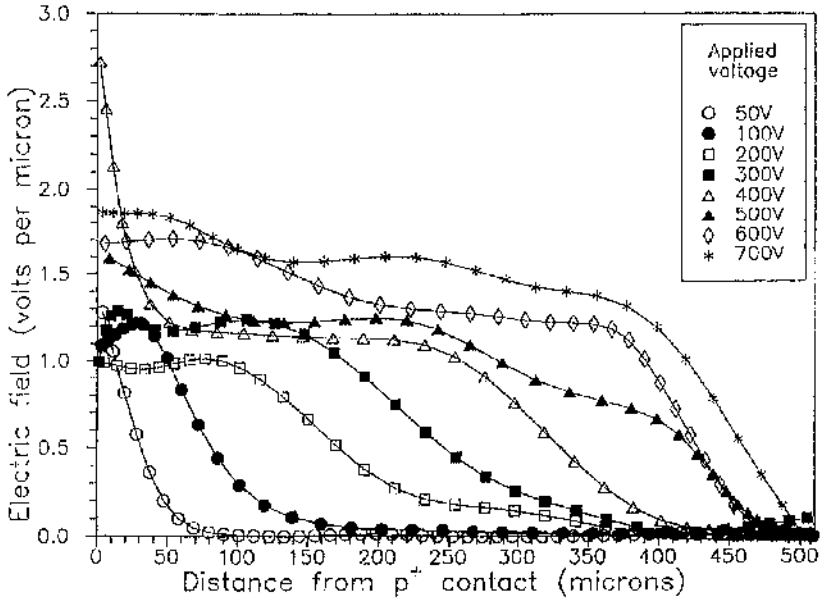

Fig. 3.15. The electric field profile through a 500 μm cleaved diode as measured with a contact probe.

From the behaviour of charge collection efficiency with applied bias for alpha particle illumination, it becomes apparent that the active region not only grows in a linear fashion, but that there is an insensitive region where there is no charge collection until a very high bias is applied. It is possible, because of the very small range of the alpha particle in the material, to approximate the signals formed as being exclusively from one type of carrier. When the detector is illuminated from the front (biased) side, the signal is formed by the electrons which traverse the bulk of the detector to the far side. The holes contribute only about 10% of the total signal for a 200 μm thick detector. (This is analogous to the signal formation in gaseous particle detectors where the avalanche of electrons is responsible for the formation of the signal but contributes very little to it as the signal owes its size to the long distance drifted by the ions.) The holes are the carriers principally responsible for signal formation when the detector is illuminated from the back with an alpha source. The graph in Fig. 3.16 shows the evolution of CCE with bias depending on the type of carrier responsible for signal formation. There is no signal from holes until a high enough bias is applied, indicating that an insensitive region exists close to the back contact. At high enough bias, the active region extends sufficiently close to the back contact that the active region reaches the end-point of the alpha particle range.

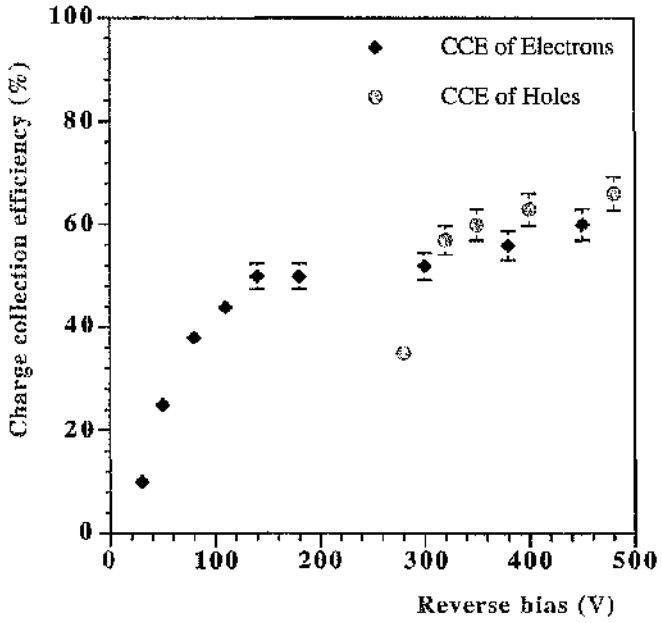

Fig. 3.16. The measured charge collection efficiency for alpha illumination of the front and back contacts.

The charge carriers can then be assigned a mean free path length λ in an environment where trapping occurs. From an extension of Ramo's Theorem, the total charge collected in an external circuit Q_{tot} due to n carriers of charge q moving between two conducting plates (with a separation of W) with each carrier travelling a distance x is given as

$$Q_{tot} = nq_i \sum \frac{x_i}{W} = nq \frac{\bar{x}}{W} \qquad (3.1)$$

Ideally, the electron moves from its arbitrary generation point to one of the electrodes and the hole moves from the same point to the other electrode, giving a net unit charge out. If the carriers are trapped by defects in the lattice they cannot contribute to signal formation. If λ is the mean free path, then

$$n(x) = n_0 e^{\frac{-x}{\lambda}} \qquad (3.2)$$

where n_0 is the number of carriers created by the radiation. Integration over W then gives the total observed charge

$$Q_{tot} = \frac{q}{W} \int_0^W n(x)dx = n_0 q \frac{\lambda}{W} \left(1 - e^{\frac{-W}{\lambda}} \right) \qquad (3.3)$$

This model can be adapted to take account of the different trapping cross-sections for electrons and holes as well as the different energy deposition mechanisms for the types of radiation used. It has been applied with reasonable success [54] to fit data obtained with alpha and beta sources.

These measurements helped to define a certain direction for modelling the observed behaviour and trying to explain the cause. The underlying reason for the linear growth of active thickness with bias can be attributed to the presence of deep levels (defects) in the crystal lattice, in particular to a defect known as EL2 which acts as a deep donor in GaAs. This is known to be a very complex defect and is thought to be the result of a Gallium vacancy in the lattice being filled by a neighbouring Arsenic atom causing an Arsenic anti-site defect [117]. The behaviour of EL2 has perplexed material scientists for a very long time. It is multivalent and even has a metastable state which is thought to be caused by the Arsenic atom returning to its correct position in the lattice under certain conditions. The defect is shown schematically in Fig. 3.17.

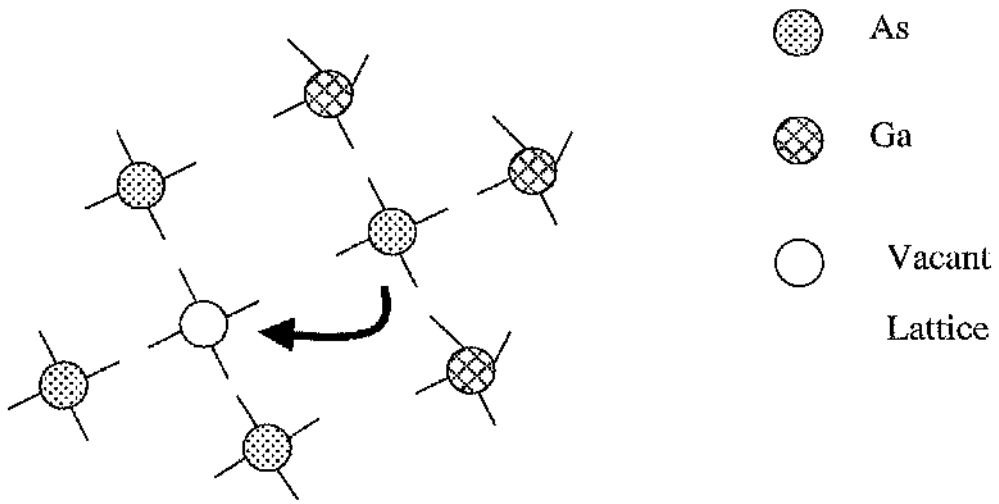

Fig. 3.17. A representation of the Arsenic anti-site defect which is thought to be the origin of the deep level known as EL2.

A number of models [55,56] has been proposed to describe the observed behaviour. These postulate that the applied bias ionises the levels in the material to create a "constant" field region in the device followed by a region which has accumulated a high

space-charge. The field drops across the latter to give the low field region at the back of the device.

McGregor [57], for example, has used measured values of deep donor and acceptor concentrations in a simple model with one shallow donor and acceptor as well as a deep donor and acceptor present in the band gap such that

$$\frac{\partial^2 V}{\partial x^2} = \frac{\partial \varepsilon}{\partial x} = \frac{q}{\varepsilon_s}(N_D^+(x) - N_A^-(x) + N_{DD}^+(x) - N_{AA}^-(x) - n(x) + p(x))$$

where the subscripts D, A, DD and AA represent the shallow and deep levels respectively. The shallow levels are assumed to be totally ionised at room temperature. This model is not able to describe the field observed in Fig.3.15 unless the electron capture cross-section of EL2 is assumed to increase as the field changes by 2 orders of magnitude for a field of about 10 kV cm^{-1}. The calculated field distribution then becomes very similar to the measured one, as shown in Fig.3.18. It is also of interest to note that the calculated field at the contact is of the same order as the measured value shown in Fig. 3.15.

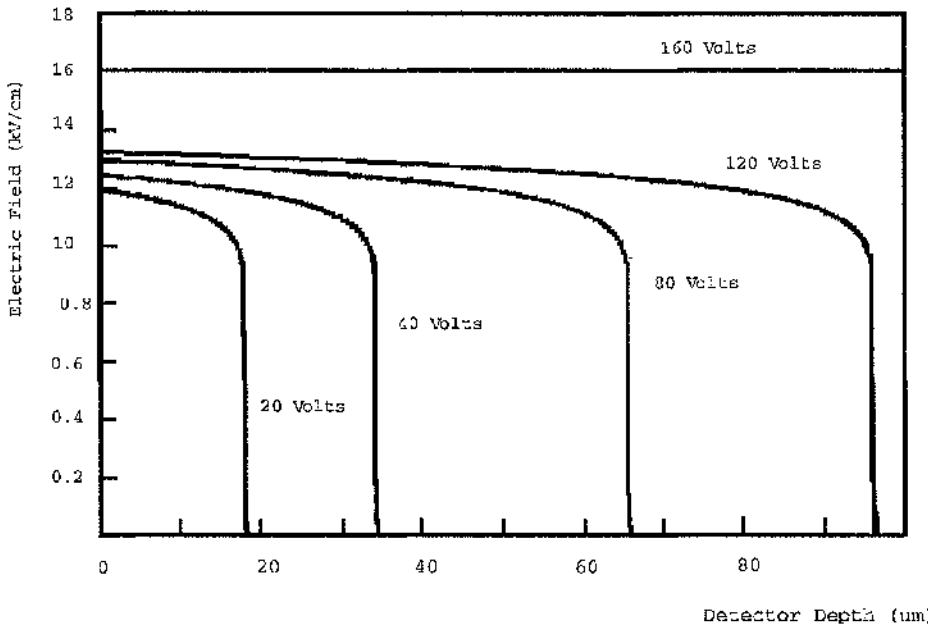

Fig. 3.18. The field distribution in a 100 μm thick GaAs diode according to the model of M^{c}Gregor et al.

While there is reasonable agreement between the model and measurements, this model predicts an abrupt interface between active and passive regions. Such an abrupt interface is inconsistent with alpha particle measurements. It should also be noted that the

behaviour of the electron capture cross-section in elevated electric fields has not been thoroughly measured and this has a critical impact on the width of the transition region.

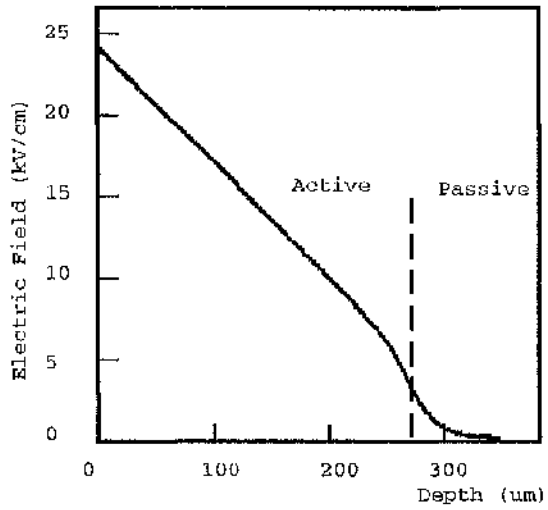

Fig. 3.19. E-field distribution as calculated from the model of Kubicki et al. [55]. The field at the Schottky contact is too high and general form does not agree with direct voltage profiling.

The modelling done to date has had only reasonable success in explaining the behaviour of the material when large bias voltages are applied. The enhanced electron detrapping cross section, which differentiates the models of Kubicki and M^{c}Gregor, gives little indication of the value of critical field required for the active region. While the models explain the linear growth of the active depth and the average charge collection observed in 3mm pad structures, the localised variations observed in small pixels (Fig. 2.5) and results obtained with a proton microprobe which show large variations in detector response when a small area is probed, cannot be explained by a simple one dimensional model of the material.

The current models assume a homogeneous distribution of one type of deep donor and deep acceptor level through out the material. The models are not capable of incorporating localised variations in the trap density in the material and this may be one area where future progress may be made towards an improved model. It is also possible that more levels need to be incorporated into the model in order to predict a more realistic behaviour. The extension of modelling to cover these aspects is far from trivial. Simulation packages using finite element modelling of the crystal structure which include some capability for introduction of traps exist, but work in this area is in its initial stages.

A comprehensive review of characterisation and modelling of GaAs radiation detectors may be found in reference [28]

Chapter 4. GaAs Microstrip Detectors.

4.1 Motivation for GaAs Microstrip Detectors

The motivation for entertaining the possibility of using GaAs detectors for tracking in a future HEP experiment was that the level of radiation foreseen over the projected ten year life of the experiment was much higher than could be tolerated by any of the alternative technologies which were then available. Pad detectors made from GaAs had been shown to work satisfactorily even after being irradiated with 16 Mrad of Co^{60} and with a flux of several 10^{14} neutrons cm^{-3}, so this looked like a promising technology for use in the harshest regions of the experiment. The first microstrip detectors to be tested were based on the design of silicon detectors that were to be used in a tracker/pre-shower detector for the EAGLE experiment proposed for the LHC at CERN. This experiment has since evolved into the ATLAS collaboration via a fusion with the ASCOT project. The detectors were fabricated in Glasgow and by GMMT [58] at their research facility in Caswell. Samples were also produced at the University of Modena in Italy. There was a need to show that commercial production of detectors was possible as an "in-house" production by a participating institute would not be acceptable for an experiment of this size. The initial detector designs were copies of the silicon versions which were proposed for the SITP (SIlicon Tracker/Pre-shower) by the RD-2 collaboration [111], the masks for which were kindly provided by Micron Semiconductors Ltd. [59]. At this time we did not have the capability to design and fabricate our own masks other than in a very basic way. The following sections describe the study of 3 different GaAs designs as the project evolved from a pre-shower/tracker to the inner wheels of a forward tracker in the harshest radiation environment. There follows a brief survey of the radiation hardness testing that was carried out in parallel to the microstrip detector development.

4.2 Types of Strips for the SITP

The micro-strip detectors fabricated in Glasgow were made on wafers supplied by MCP Wafer Technology Ltd., which were processed without thinning and so had factory polished faces. The wafers, as supplied, were 500 μm thick. The detectors consisted of

300 μm wide strips of metal on a pitch of 330 μm and were made with rectifying contacts for the strips and a continuous ohmic back connection. The strips were 15 mm long.

The GMMT devices were different in that they were carbon copies of the silicon detectors proposed for the SITP [60]. Each detector had 64 strips, each 24 mm long with a width of 275 μm on a pitch of 375 μm. The metallisation recipes were the GMMT 'standard', proprietary recipes for rectifying and ohmic contacts and were deposited with rectifying strips.

The sample produced at Modena was made on a 675 μm thick, 3 inch diameter wafer. The Modena device had 40 mm long strips which were 200 μm wide on a 400 μm pitch. The contacts were deposited in the same sense as the previously described detectors but the ohmic contact was modified in an attempt to improve the breakdown characteristics of the devices [61]. (In a conventional ohmic contact, the gold and germanium form a eutectic when annealed. This then diffuses into the crystal and dopes the material close to the surface. It is known that "fingers" of germanium can extend quite deeply into the material as the local diffusion can be greatly enhanced by lattice imperfections.) The ohmic contact on the Modena detector used a layer of palladium and then silicon to form an ohmic contact.

The use of read out strips in Si is complicated by the fact that additional implants have to be made between the strips on the back side to avoid the build up of a continuous space charge layer on the oxide between strips when the detector becomes fully depleted. It was felt that the high intrinsic resistivity of the GaAs would be sufficient to make a double-sided detector using Schottky contacts on both sides of the device and that no further processing steps would be necessary. A further detector was therefore fabricated in this way in Glasgow, with orthogonal contacts 275 μm wide on a 375 μm pitch using a 650 μm thick wafer.

All of the above samples were mounted (glued) on a printed circuit board which had a hole machined in the centre for the device and gold-plated tracks leading to a standard (0.1 inch pitch) connector to the read-out. The ultrasonic wire-bonding of detector strips to read out chips was done at CERN by Bob Boulter who has been of inestimable help on many such occasions.

4.3 Read-out Electronics, Test Telescope and Initial Results

The detector evaluation in a particle beam was carried out before the widespread availability of the highly accurate, almost 'standardised' silicon telescopes that are

currently used to track the passage of particles. The telescope used in the first detector tests consisted of 2 planes of silicon detectors with strips of 100 μm pitch and 2 further planes of the GaAs devices under test, with 15 mm separation between planes. The trigger particles were selected by a pair of crossed scintillators upstream of the detector arrangement and a vertical scintillator behind, all read-out by photomultiplier tubes, as shown in Fig. 4.1. Each detector plane had 32 channels of read out, sufficient to define a region of about 8 to 10 strips wide in our test detectors.

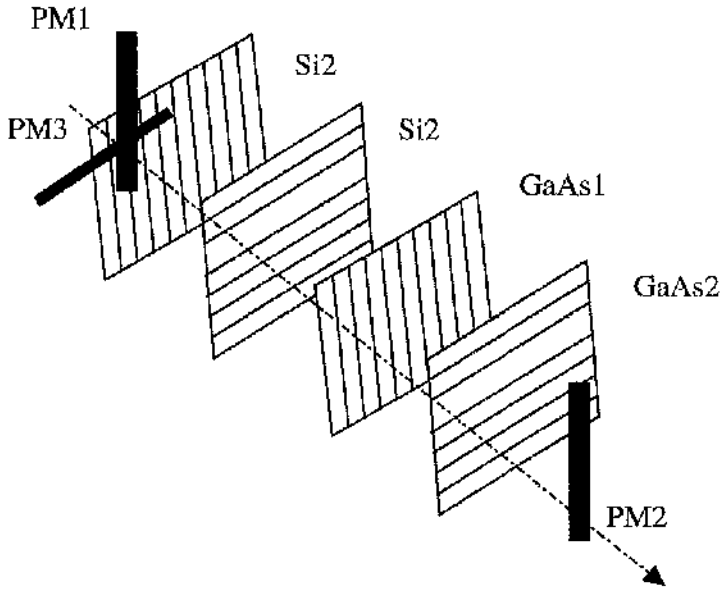

Fig. 4.1 The layout of the telescope used to test the first GaAs micro-strip detectors. The dashed line represents the passage of the particle beam through the arrangement.

The AMPLEX chip, described in section 2.4, was chosen to read out our first micro-strip detectors. It was available mounted on a pcb with a rather simple means of making a relatively low capacitance connection. The alternative read-out chips available at that time were all based on the MX series, which had no means of monitoring the analogue signal. This would have made the set-up with an unknown detector performance impossible. In the set up shown schematically in Fig.4.2, the sequencer accepts triggers (selected particles) from the coincidence of the photomultiplier signals which has been AND'ed with a BUSY veto from the data acquisition. All the necessary signals to control the AMPLEX chip and set the timing for the ADC gate are then generated by the sequencer with the help of a number of timing units to set up delays specific to the cabling in the experimental hall.

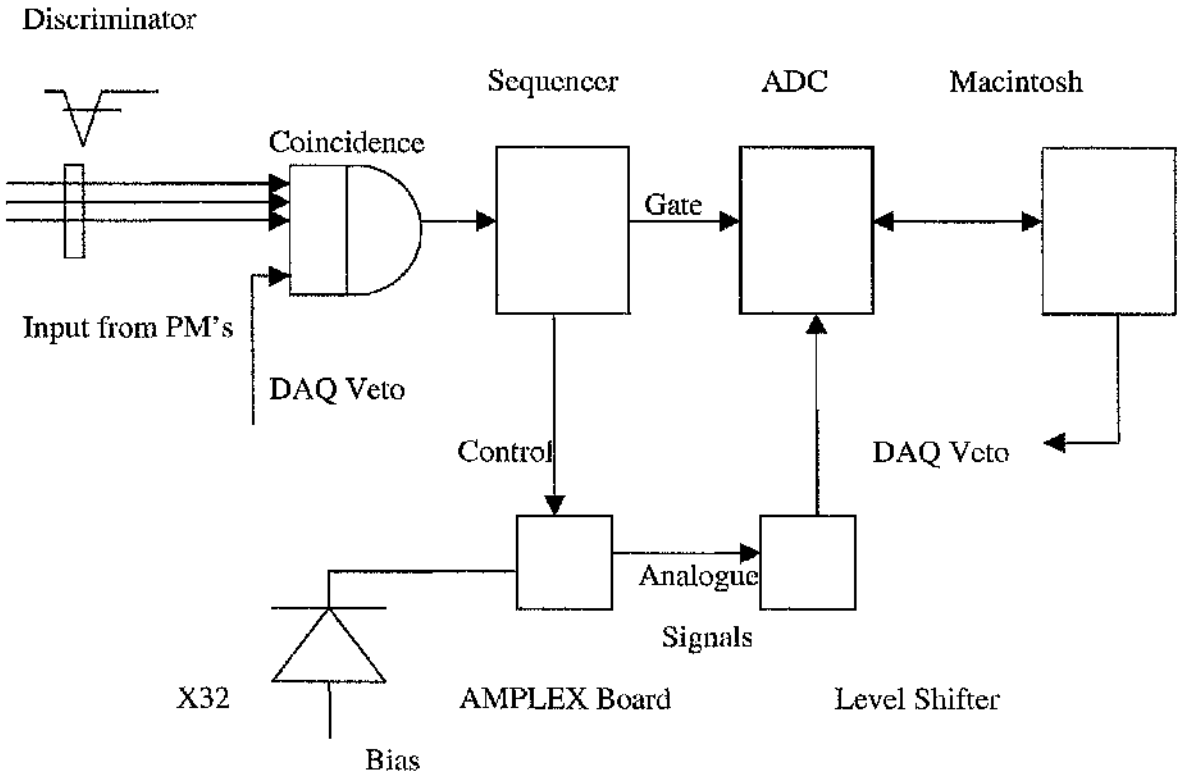

Fig. 4.2 The data acquisition set-up used to drive the AMPLEX read out in the test-beam.

The Macintosh is interfaced to a CAMAC crate containing the ADC with a MacVEE card and uses a Status A unit for managing the interrupt status of the acquisition system. The software package used for the acquisition was MacDaq 3.0, written by Federico Cindolo. This software controlled a CAMAC crate and read-out the ADC as well as providing the online data sampling and was reasonably easily set up for the required configuration. The set-up described above was installed in the X1 experimental area on the CERN SPS (Super Proton Synchrotron) accelerator. The detectors were tested with both pions and electrons of 70 GeV/c.

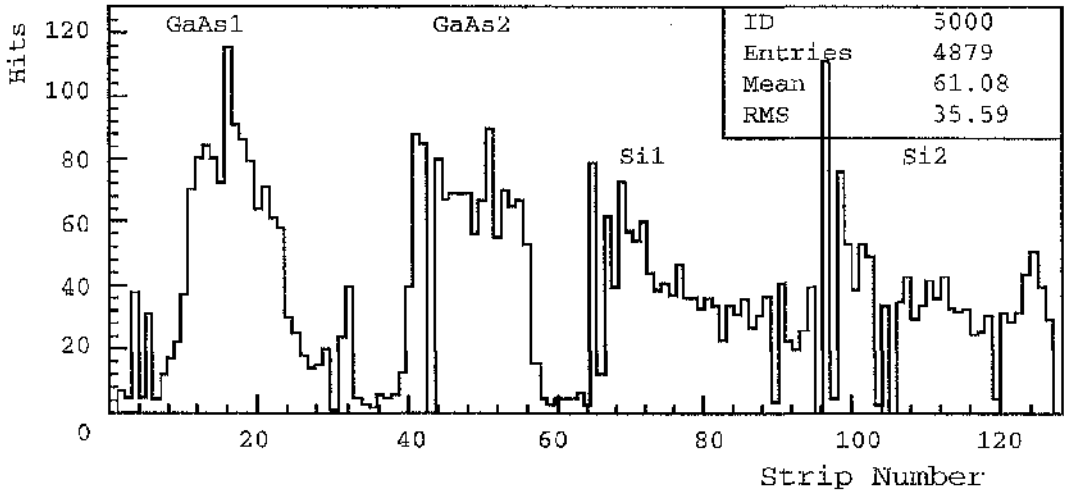

Fig. 4.3 The beam profile across the planes of the telescope. The narrower profile on the GaAs planes is due to the strips being wider than those on the Si detectors

The plots shown in Fig. 4.3 and 4.4 show that the telescope was successful in defining the particle beam and also in tracking the particles through the test detectors. In order to calculate the charge collection efficiency of the GaAs detectors, the following analysis was performed. For each data run with fixed parameters the noise σ and offset of each channel was calculated from a pedestal run of 2500 events and used to establish the cuts used to analyse the data. The signal amplitude from the GaAs strips had a cut of 2.56 σ applied. A further cut required that a hit in the GaAs detector fell within two strips of the position predicted by a Si detector whose strips were parallel. A more refined analysis would have required a much better telescope than that which we were using. The detection efficiency,η, for each detector was calculated as the number of hits in (Si1+Si2+GaAs) divided by the number of hits in (Si1+Si2), after both the noise and spatial cuts had been applied. The pulse height distribution of all hits surviving both cuts was fitted by a Landau curve. Its most probable value divided by the average σ of the strips gave the signal to noise ratio. The equivalent noise charge (ENC) was measured in calibration runs, where a voltage pulse was applied to a precision capacitor at the input of the amplifier, thus injecting a known charge, enabling us to measure the value of σ in units of electronic charge.

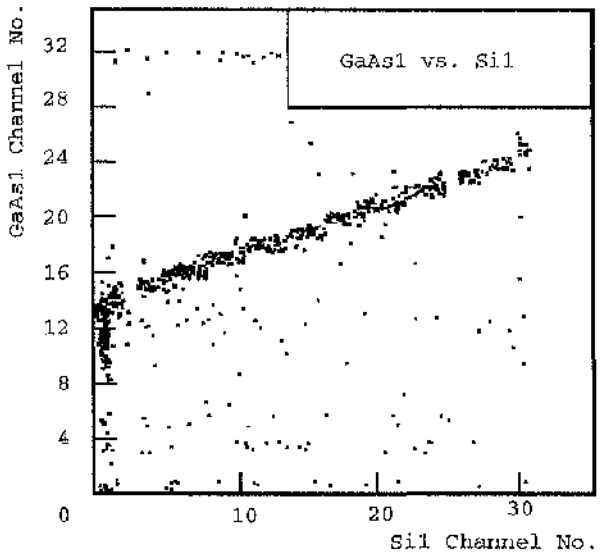

Fig. 4.4 A correlation plot showing the hits on GaAs1 vs. Si1. The large difference in the pitch of the strips on each detector is again evident.

The best performance for each of the single-sided detectors, using the criteria described above is presented in Table 4.1.

DETECTOR TYPE	THICKNESS (μM)	MAXIMUM BIAS (V)	RAW DETECTION EFFICIENCY	C.C.E.	S/N
Glasgow I	500	200	96%	13%	5.4:1
GMMT1	600	300	97%	16%	8:1
GMMT2	600	400	98%	16%	8.6:1
Modena	625	700	96%	25%	12:1
Telettra	450	375	97%	17%	6.4:1

Table 4.1 A summary of the performance of the first GaAs microstrips tested in the beam at CERN.

The detectors gave broadly similar performances except for the Modena detector, which was capable of being operated at a much higher bias and was able to collect much more charge. The detection efficiency of this detector was not any better than the others and decidedly worse at lower bias. This was attributed to the metal to pitch aspect ratio (1:1 for this detector) as it was thought that there could be a region between the strips

with a lower charge collection efficiency. If this were so, then the passage of particles in the space between strips may produce less total charge, resulting in a lower detection efficiency. The detector was later cleaved on a plane orthogonal to the strips and examined in an electron microscope, where it was seen that there was a low field region between the strips, which could explain this effect.

4.4 Results for Double-Sided Detectors

One double-sided detector took the place of both GaAs read-out slots in the telescope, as we were limited by the number of available readout channels. The physical connection of the detectors to the electronics until now had been a dc-coupling. Clearly this needed to be modified in order to accommodate the biasing of the strips on one side and so the scheme illustrated in Fig. 4.5 was implemented on the printed circuit board.

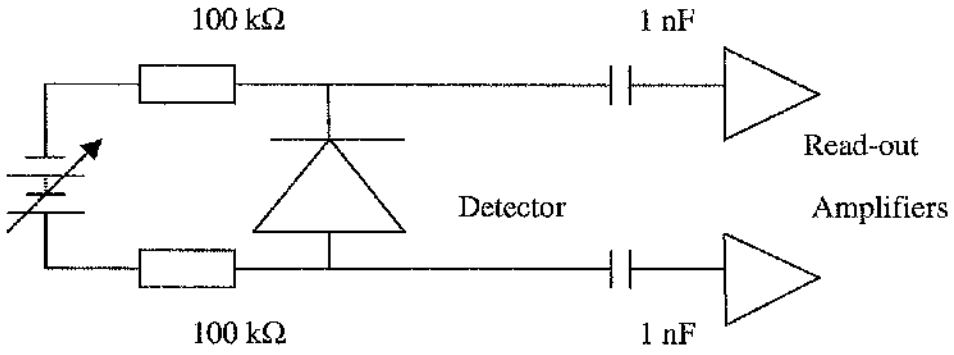

Fig. 4.5. The electrical connection for ac-coupling of the double-sided detector. Since both contacts were rectifying, this scheme gave us the possibility of biasing from either side. The ENC of the system was 3000 e- and the shaping time used was 1.5 μs.

The detector was tested in a 70 Gev/c pion beam in the telescope comprising two planes of Si strips with 100 μm pitch which were rearranged to have their strips parallel [62]. The device functioned well and gave signals from both sides as anticipated. From the outset, the online displays showed that the charge collected on both sides did not appear to be equal. The histograms of the collected charge for each side were not remotely alike as seen in Fig. 4.6. The calibrations were checked again to ensure that no

error had been made. In the analysis to date, no attempt had been made to look at the charge sharing between strips following the passage of each individual particle. By looking only at the accumulated charge on each of the strips, the charge collection efficiency was measured to be 21% on the cathode side and only 11% on the anode side of the device. In an attempt to find the missing charge, signals from neighbouring strips were examined each time a signal was seen (greater than 2.56 σ). Hits were selected on the Si planes and then a track linking them was extrapolated out to the GaAs. A hit was accepted if the signal was above 2.56 σ for that strip and within 1.5 strips of the extrapolated track. This method was only valid for the anode as these were the strips parallel to the Si strips. For the cathode, a hit was accepted if there was a hit on the three other planes. The signal-to-noise ratios for the two sides were 6.2:1 and 3.6:1 for the cathode and anode respectively. The low value of signal-to-noise ratio on the anode side precluded the imposition of any cut above the noise.

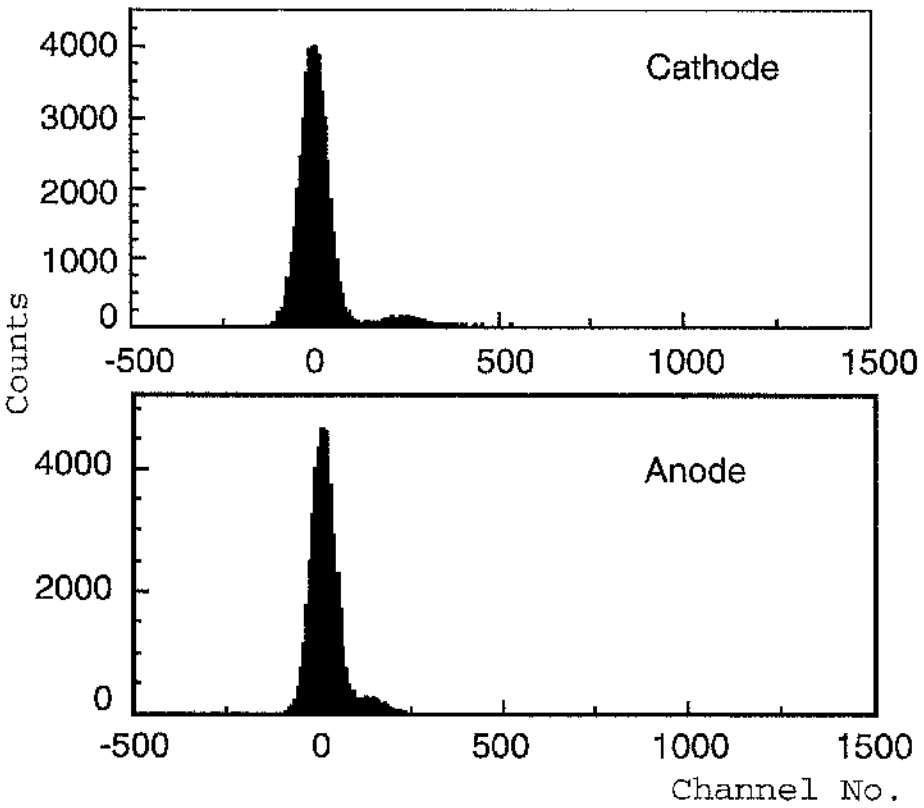

Fig. 4.6. The graphs show the charge distributions for the two sides of the double-sided detector. It is obvious that the anode has a much poorer performance as the separation from the pedestal is less pronounced.

For each hit assigned according to the criteria described, the charge over the five neighbouring strips on each side was averaged over all the events, without applying a cut on the noise. As the analysis had always previously applied a 2.56 σ cut, the effect of

charge sharing was largely ignored. It is clear that there could be no imbalance between the charge seen on the anode and on the cathode – we just had to look in the right place. The distributions shown in Fig. 4.7 show that 16% of the charge in the central strip appears on each of the neighbours on the anode side, whereas the sharing is negligible on the cathode side.

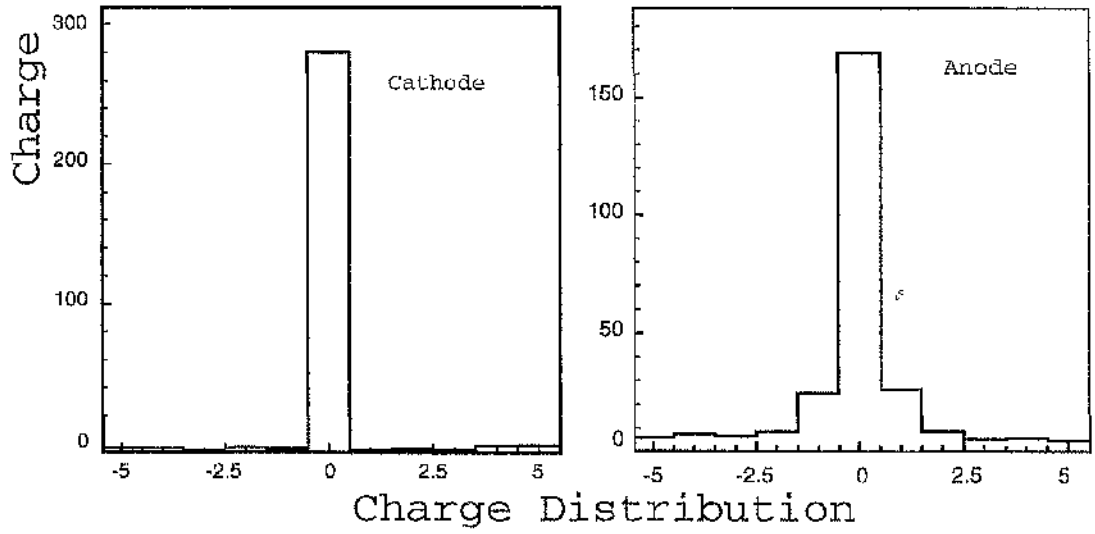

Fig. 4.7. The distribution of charge w.r.t. a central strip without any cuts applied to the neighbouring strips. The cathode charge is distributed essentially over one strip whereas the anode signal is shared by the neighbours.

If the detector is assumed to contain a high field, 'depleted' region and a low field, inactive region, the charge liberated by the passage of the ionising particle will drift to the edges of the high field region and then diffuse slowly to the contacts. The diffusion of the charge, in the absence of a high drift electric field means that the charge cloud will spread laterally as it migrates to the contacts on the low field side. Consequently the charge will be shared between more strips. The measured cce of 21% corresponds to an active thickness of 130 μm. If the charge diffuses through the remaining 520 μm to reach the anode, it is not unreasonable to expect that the lateral diffusion of the charge cloud would increase the charge sharing between strips separated by 375 μm.

After the initial evaluation of the double-sided detector, it was decided to concentrate on the development of single sided detectors on material that had been thinned to 200 μm. This would give roughly the same charge output as a 300 μm thick silicon detector and reduce the effect of the shorter radiation length of GaAs. The Pre-Shower/Tracker had evolved into an Inner Tracker which uses two principal technologies for particle tracking:

semiconductor detectors made from Si or GaAs, depending on the radiation environment, and a Transition Radiation Detector (TRD) which uses a polyethylene radiator and xenon filled gas detectors to generate and detect low energy X-rays from the passage of relativistic particles. The particle type can be identified by the density of X-rays generated along the length of a track.

The GaAs detectors for this type of tracking required much more complex structures than those described so far. The pitch of strips used had been of the order of 200 to 400 μm. The new generation of detectors required strips on a 50 μm pitch in order to deliver the spatial resolution needed to achieve the physics performance of the whole detector. Several changes were needed in order to evaluate these detectors. The AMPLEX chip was no longer suitable as the density of channels was too low. Fortunately a suitable new read-out chip, the VIKING, became available. The detectors had to be wire-bonded directly to the readout chip as any other connection at this high density would increase both noise and assembly complexity. The telescope used to track the particles through the test detector needed to be much more precise than that previously used. The detectors also required an integrated biasing scheme as well as an ac-coupled output to the read-out, since external capacitors would use too much space.

4.5 AC-coupled detectors

The detectors were made commercially by Alenia SpA., [63] Rome in their research laboratories. The production was supervised by Dr. Antonio Cetronio and the masks were designed by the author and written in Glasgow. The bias was implemented by a reach-through structure on the high resistivity substrate. The reach-through is a 5 μm gap in a track that is 6 μm wide. A common bias bar runs orthogonal to the rectifying strips and establishes a high resistance current path to each strip when biased correctly. It has been shown recently that this type of biasing introduces excess noise in silicon strip detectors but the implementation of this type of biasing structure on our detector had the attraction of needing no extra processing steps in this first attempt [118]. The rectifying strips were capacitively coupled to the read-out strips using a Si_3N_4 dielectric layer deposited between the two metal layers. The lift-off process used to deposit metal onto GaAs can occasionally leave sharp edges on the metal if the chlorobenzene soak has not been successful. These points can encourage a micro-discharge to that read-out strip through the dielectric if it overlaps. The read-out strip was therefore designed not to overlap the

rectifying strip at any point so that the possibility of breakdown between the two layers would be reduced

The read-out strips were connected to their bond pads by air-bridges that make the connection through the air at a height of 5 – 7 μm above the surface of the material. The process used by Alenia is broadly similar to that used in Glasgow although they use their own proprietary recipes for contacts and the processing of air-bridges. Their detectors have generally similar performance to those produced in Glasgow except where an ion implantation step is used to increase the breakdown voltage of the ohmic contact by reducing the tendency for minority charge injection when the high field region reaches the back contact.

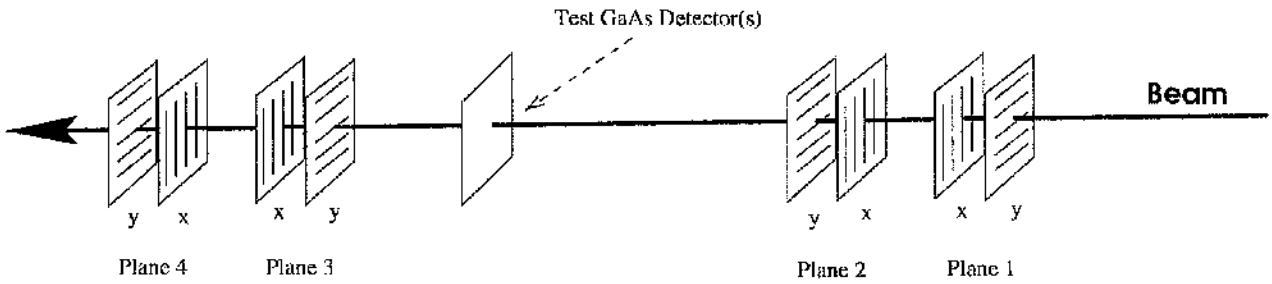

Fig.4.9. A representation of the telescope used to obtain high resolution tracking.

The detector used for this beam test had 30 μm wide strips on a 50 μm pitch. The strips were 28 mm long and the LEC substrate had been thinned to 200 μm. The detector was bonded to a VIKING chip and placed in a slot on the telescope. This telescope, outlined in Fig.4.9, had 4 planes of X-Y read-out on 50 μm pitch silicon strips and a spatial resolution of 3 - 5 μm for tracks through all its planes [64]. The differential analogue signal from the VIKING was daisy-chained through the other chips on each read out hybrid, buffered by a video amplifier on an adjacent motherboard and sent via a twisted pair cable to the input of an analogue to digital converter (ADC) in the counting room. The SIROCCO ADC used was a modified version of the original CAMAC design adapted to run in a VME crate. Each SIROCCO had a 12 bit ADC coupled to a 2KByte deep memory. The telescope used one per plane, as well as a separate one for the test detector. The converted data were written to an EXABYTE tape by the VME processor, which controlled the acquisition system. The telescope and detector (AL-W3-6AC) were

installed in the X1 area at the CERN SPS. The particle beam used for the tests was a 70 GeV/c pion beam. Initially, the noise in the test detector was unacceptably high so the shaping time of the front end was reduced from the standard setting (for Si) of 2100 ns to the minimum possible, 680 ns, in order to reduce the parallel noise due to the high leakage current of the GaAs detector. Even so, the ENC was of the order of 2000 electrons – a factor of 5 more than expected for a detector of the type used. The signal at the maximum applied bias of 180 V was about 12,000 electrons (45% cce) which is in reasonable agreement with a measured cce of 60% on pad structures from the same wafer. The pulse height spectrum, shown in Fig. 4.10 shows the effect of a 3σ noise cut on the low energy part of the Landau due to the high noise. The offline analysis, carried out by Steven Gowdy [65], showed that the detector performance was consistent with the measured signal-to-noise ratio of 6.

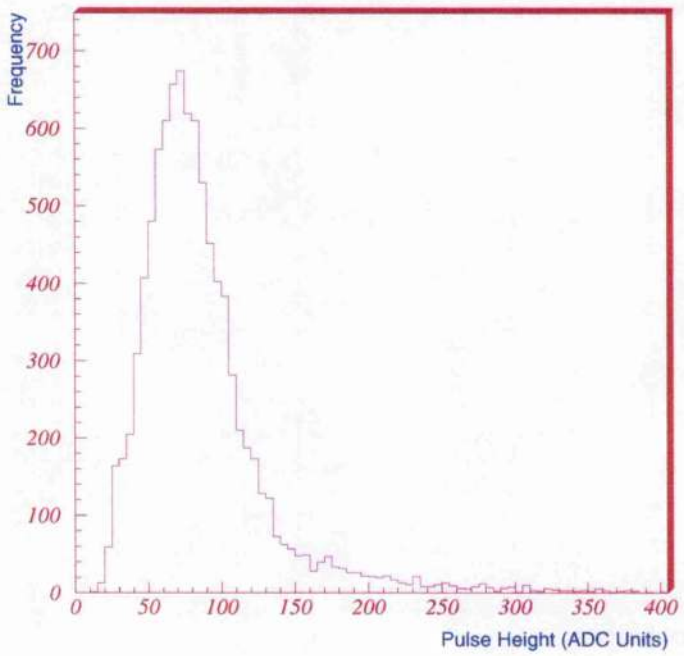

Fig. 4.10. The signal distribution for a single strip on the ac-coupled detector in a pion beam at the SPS.

In a system where the strip with the highest signal is considered to be the hit, and no information from adjacent strips is used to interpolate for a more accurate position, the resolution is given by the pitch divided by $\sqrt{12}$. When the signal on neighbouring strips is taken into account, the resolution can be enhanced considerably. Because the signal-to-noise ratio was so low, one would not expect any significant improvement in resolution over that obtained using clustering algorithms. The residual distribution shown in Fig.

4.11 shows a marginally better σ than the 14.43 μm that would be expected for a purely digital readout. The difference is so small that this probable represents no improvement.

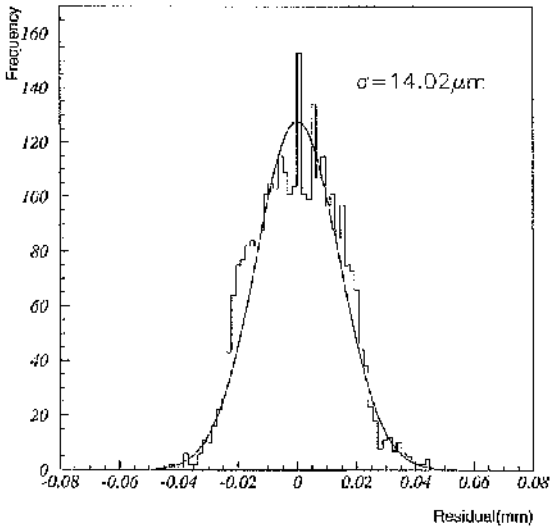

Fig.4.11. The residual distribution for the ac-coupled detector.

4.6 Binary Wedge Detectors

In the ATLAS experiment, the GaAs detector was to occupy the innermost rings of the forward part of the Inner Tracker where the radiation levels would preclude the use of any other technology. Largely on cost grounds, it had been decided that the electronics to read out the detector would use digital signals at the earliest possible moment so that the read out consists essentially of an amplifier/shaper followed immediately by a discriminator. The subsequent manipulations required to pipeline data during trigger information processing are greatly simplified if the information is digitised. This binary read-out has been designed by groups at U. C. Santa Cruz and LBL in California. The function is implemented in a three chip set comprising a bipolar amplifier/shaper/discriminator called the LBIC [66], a CMOS digital pipeline chip – the CDP [67] and a CMOS control chip called the HAC [68]. It was necessary to demonstrate that the GaAs detectors would function with binary read-out electronics running at the correct LHC speed (40 MHz). The other interesting aspect of this test is that the detectors must be wedge shaped in order to fit effectively in a ring around the beampipe.

The 55 mm long rectifying strips therefore have a pitch of 62.5 μm on the narrow side 76 μm on the wide side. The gap between metal strips is a constant 15 μm. All the corners on each strip have been rounded on a 5 μm radius using a series of 20 arcs to eliminate any sharp metallic points that could cause discharges. The read out strips have the same

dimensions, except that the gap between metal strips has been increased to 35 μm. The detector was fabricated by Alenia SpA. using a design and masks from Glasgow. Some details of the detector design are shown in Fig. 4.12. The bias was provided by a variation on the punch-through mechanism in which contacts are made ohmic and the high resistivity of the material is used as a pure resistance. This means an extra mask step to make both ohmic and Schottky metal depositions on the top side. Good ohmic contacts are difficult to make on SI GaAs and, indeed, there is an asymmetry in the I-V characteristic, measured across the bias structures. The detector was characterised in the laboratory, where resistance and capacitance were measured prior to assembly on a support and bonding to the electronics on a hybrid. The detector had been thinned to 200 μm by the manufacturer and the wedge shape was cut using a diamond saw at 5° off the crystal axis.

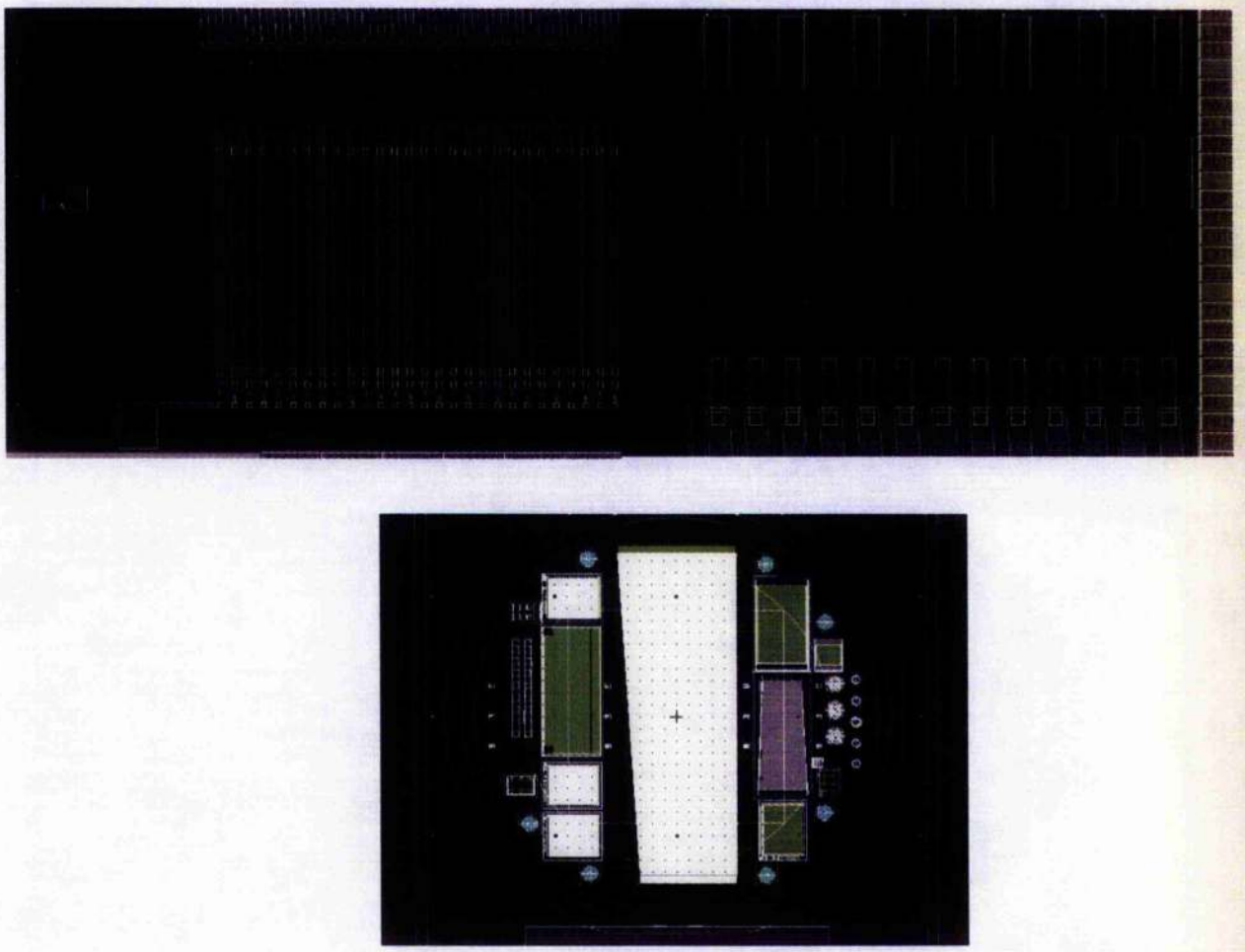

Fig. 4.12. Some details of the wedge detector layout illustrating the bias structure on the left, the readout pads on the right – notice the rounding of corners to reduce the possibility of high field spikes. The wafer layout for a 3" wafer is underneath.

The coupling capacitance was measured to be 370 pF with a variation of less than 10% across the detector. Of the 80 strips tested, only 1 had a pinhole. The value of the bias resistance was of the order of 17 MΩ when the current was between 0 and 250 nA. Since the expected leakage current per strip at operating bias is about 50 nA, this value is quite acceptable. The dielectric was specified as having a breakdown voltage of greater than 30 V -- all of the structures tested were found to be good to 30 V. At nominal leakage current through the measured resistance of 17 MΩ, the voltage stress across the decoupling capacitor is a only fraction of a Volt [69]. The process was specified to give 200 pF mm^{-2} and the test structures on the three wafers received had 187, 185 and 181 pF mm^{-2}, indicating that the wafers had been processed according to specification.

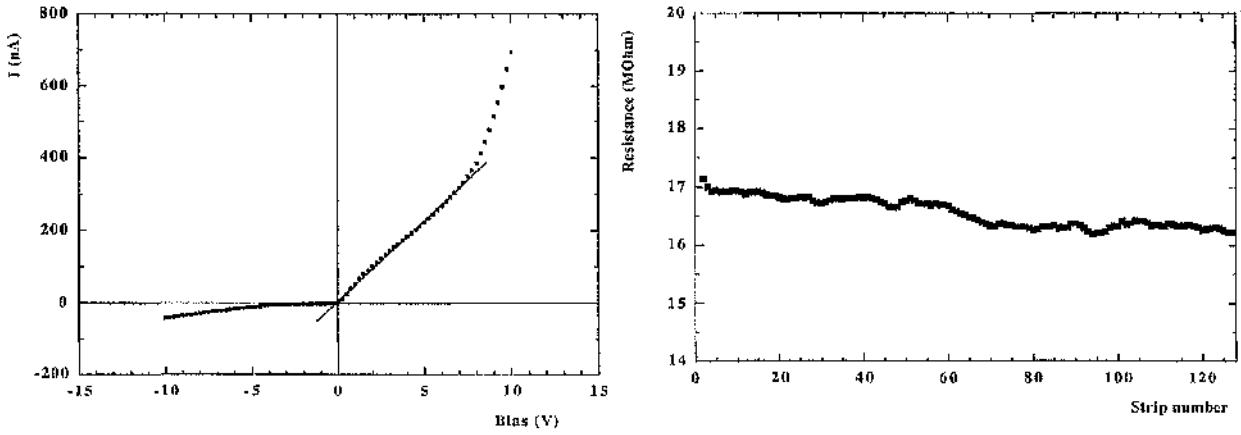

Fig. 4.13. The I-V curve for the bias structure is not completely ohmic. The resistance map across the detector shows good uniformity and reasonable values for the resistance.

The detector was bonded to the read-out electronics on a kapton hybrid developed at KEK, Japan, by Ogmundur Runolfsson, who took great care to minimise the length of the bias connection. The detector had been laid out with the decoupled strips bonded out at one end and the bias structure bonded out at the other. This bias connection is crucial for the binary read out, as the detector bias has to be decoupled as close to the bias point as possible – failure to provide adequate decoupling aids the injection of common mode noise [119]. The binary read out scheme proposed has virtually no immunity to common mode noise and therefore inadequate decoupling results in detectors which do not work.

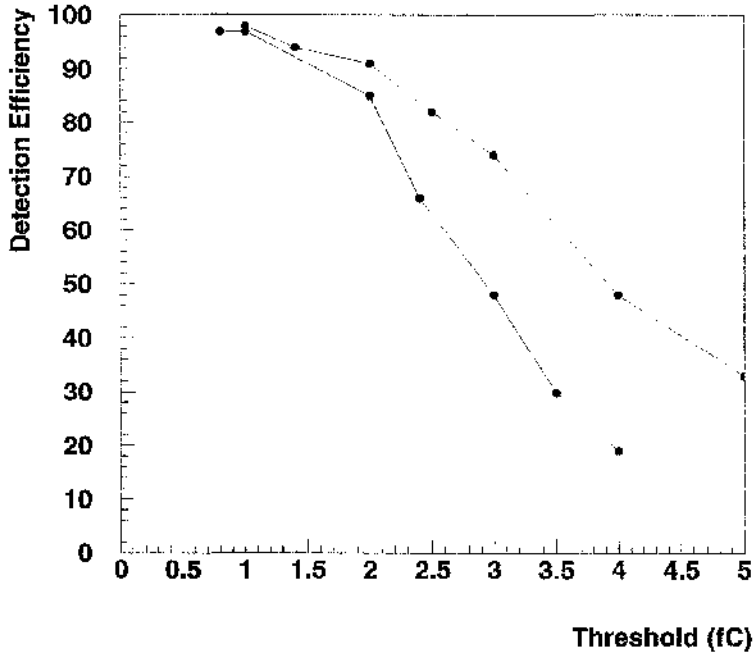

Fig. 4.14. The detection efficiency graphed as a function of threshold applied to the binary readout for 250 Vand 350V bias.

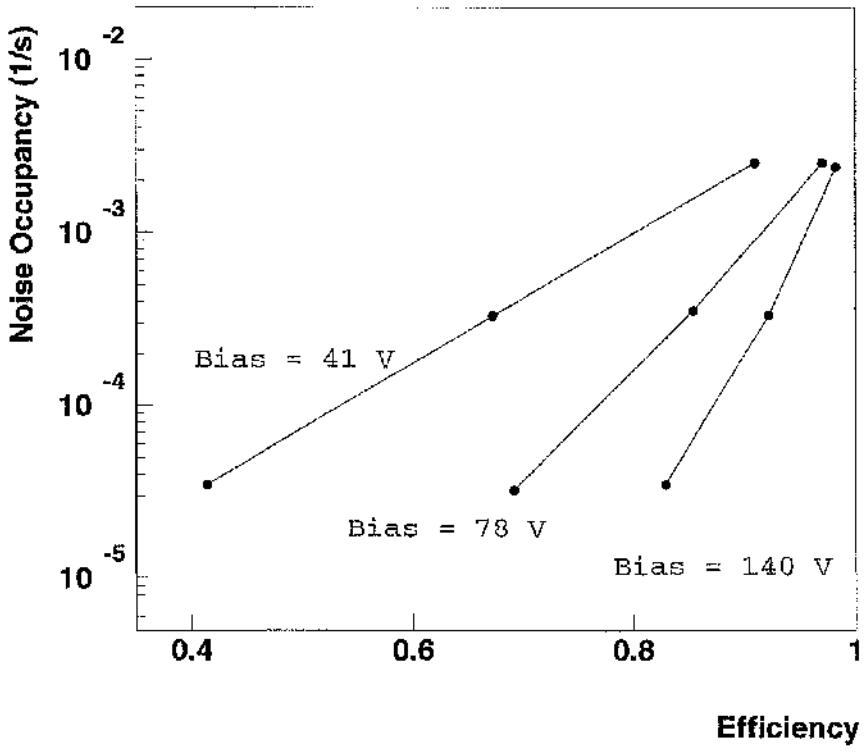

Fig. 4.16. The noise occupancy as a function of the efficiency of the detector. This is the binary equivalent of signal-to-noise ratio

The detector module was installed in a Si telescope comprising 4 x-y planes read out by the VA2 chip [70], a successor to the VIKING. The set up was very similar to the previous telescope, except that this time the binary read out was running in tandem to the telescope. The binary read out was managed by a dedicated DSP card in a VME crate. The crate itself contained a RAID processor which, in conjunction with a SunStation, ran the acquisition for both systems as well as the online monitoring.

The analysis was carried out by Thilo Schmid of Freiburg [71]. The detector has an efficiency of 97% at a discriminator threshold of 1 fC, the desired operating point for the binary read out, for bias voltages of 250 and 350 V as shown in Fig. 4.14. The detection efficiency drops off much quicker than expected as the threshold is increased and a longer plateau would be much more desirable. The noise occupancy shown in Fig 4.15 is of the order of 10^{-3} hits per strip per second which is the maximum acceptable for ATLAS.

4.7 Radiation Hardness and Testing

The performance of the detector in the beam was, however, not the only criterion that had to be met in order to show that GaAs was the correct choice for the detectors in the harshest radiation environments. Throughout the development of the fabrication technology and testing of the detector performance in tracking devices, a parallel programme of irradiation testing was being followed. The GaAs detectors were first shown to be capable of functioning after a neutron dose equivalent to 10 years running in the hottest region of the Inner Detector. Samples were irradiated at the neutron spallation source at the ISIS facility (Rutherford Appleton Laboratories), which provided a well characterised source of neutrons with a peak energy of about 1 MeV [72]. This corresponds to the energy at which the maximum damage to the crystal occurs in Si and so the ISIS source is particularly useful for characterising the effects of radiation damage.

Samples were also irradiated in a commercial facility near Lyon in France, where they were exposed to a powerful Co^{60} source which is normally used for sterilisation. The samples were exposed to up to 16 Mrad and showed very little loss of signal and only small increases in leakage current [73] as shown in Fig. 4.17. This is not really very surprising, as the technology used to make the detectors on GaAs is known to be inherently very radiation hard for ionising radiations such as the gamma-rays from the Cobalt source. The technology uses no oxides or dielectrics as integral parts of active

devices. There is, therefore, very little build-up of polarised charge in the dielectrics which can alter the field distribution in the detector bulk and alter its performance. The principal damage mechanism of such ionising radiation involves the liberation of charge in dielectrics, which tend to form dipoles, if the dielectric is stressed by an electric field while under irradiation. The resulting dipole can result in threshold shifts in devices such as Field Effect Transistors or in detectors where structures such as field plates and "foxfets" are used.

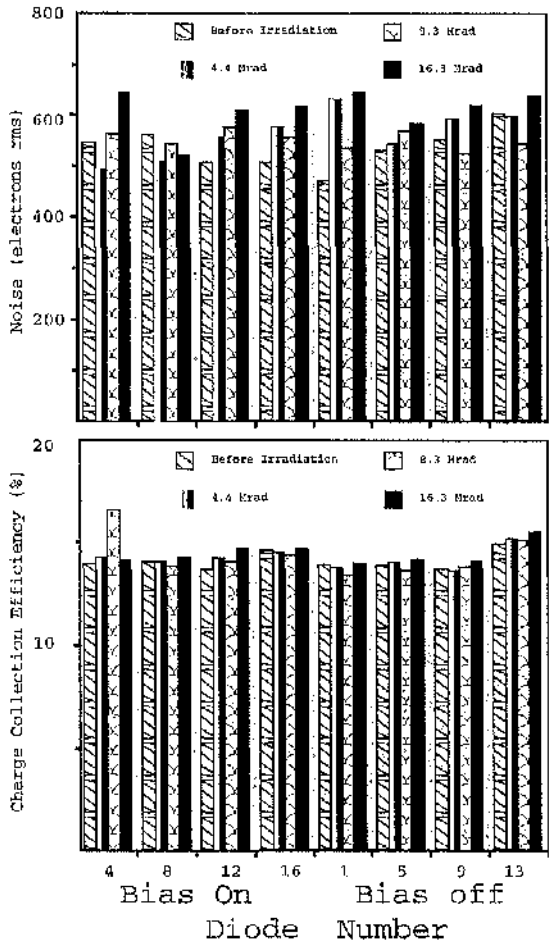

Fig. 4.17. Measured values of collected charge and noise for detectors before irradiation and after 4.4, 8.3 and 16.3 Mrad from a commercial Co^{60} source. There is essentially no change in the device performance up to this level of irradiation. The bias does not appear to be important.

The damage caused by neutrons and charged particles is quite different in nature. The common denominator for this type of damage is the non-ionising energy loss, (NIEL), which is responsible for damage to the lattice structure of the crystal. This damage leads to the introduction of energy levels in the band gap which can alter the Fermi level and therefore change the effective doping concentration. This leads to type inversion in Si detectors at fluence levels of some 10^{13} cm^{-3}, (depending on irradiating particle type), where the bulk semiconductor doping changes from "n" to "p" type. The introduction of

these mid-gap levels also provides additional paths for carriers to pass from the valence to conduction bands and so increases the leakage current.

GaAs detectors appeared to be free from these worries, the leakage current did not increase by more than a factor of 2 or 3 for a dose of 10^{15} cm^{-2} neutrons, while the same dose in Si results in several orders of magnitude change. The spectra shown in Fig. 4.18, before and after a neutron dose of $5x10^{14}$ cm^{-2} show that the noise remains the same, as there has been no major change in the leakage current, however the magnitude of the charge signal after irradiation falls off to less than 40 % of its original value [74]. The signal is still easily resolvable from the noise and so the detector is still functional. As this level of irradiation is believed to be a factor of 2 more than the lifetime neutron dose in the hottest part of the experiment, this performance was judged acceptable.

Although neutron-induced damage is the major concern for silicon detectors at the LHC, simulations of the radiation environment showed that the major fraction of the total dose comes from pions and other charged particles, particularly in the forward regions where it was proposed that the GaAs detectors would be installed [75]. Studies suggested that there could be differences in the damage caused by these charged particles in Si and GaAs [76]. Comparisons were hampered by less accurate calculations of NIEL in GaAs, however.

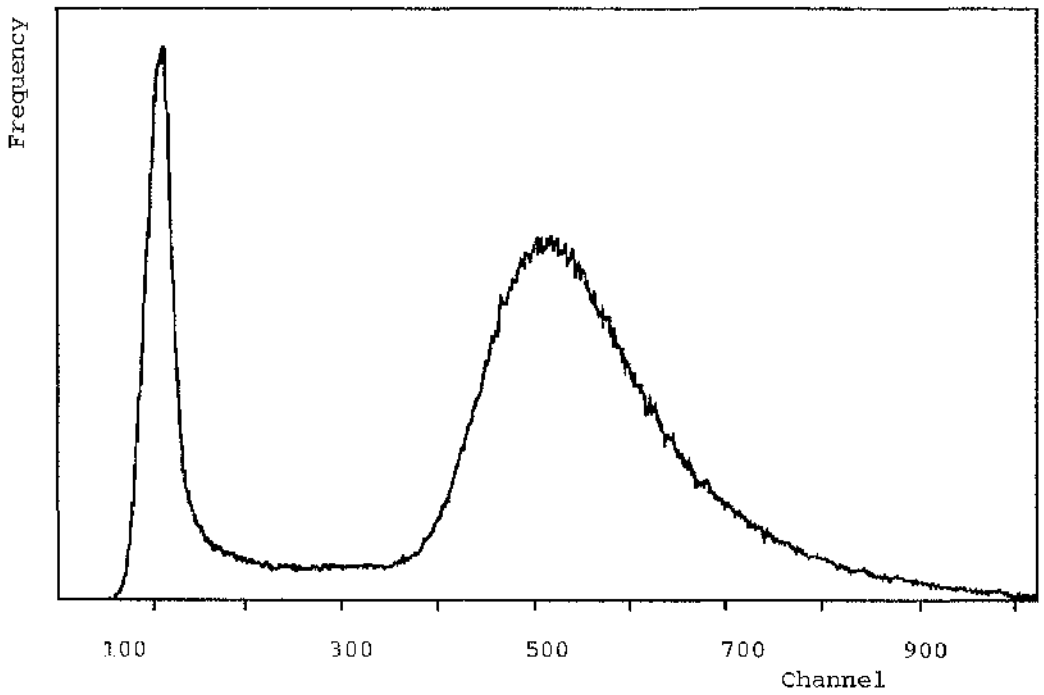

Fig. 4.18a. Spectrum taken before a neutron irradiation of $5x10^{14}$ cm^{-2}

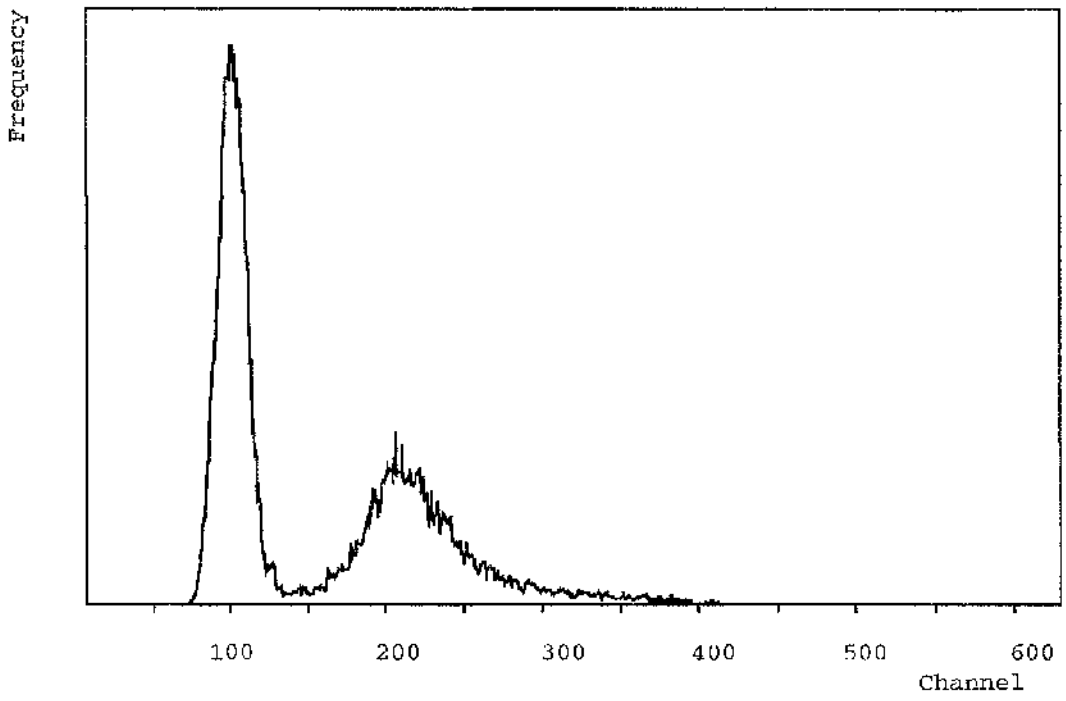

Fig. 4.18. Spectrum taken after a neutron irradiation of $5x10^{14}$ cm^{-2}. The noise has increased only slightly in the irradiated sample but the signal has fallen off to about a third of its original value.

The first tests with pions, carried out at the Paul Scherrer Institute in Villigen, Switzerland, using a pion beam of 300 MeV/c indicated that this type of irradiation was

far more damaging to GaAs detectors than had been anticipated. The signal was reduced to 10% of its original value after 1-2x10^{14} pions cm^{-2}. It now became a matter of urgency to try to understand the loss of charge collection and to improve it if possible. The measurements show that, after irradiation, the high field region extends further into the crystal for the same applied bias voltage. There is even an "improvement" in the breakdown characteristic of the device in that there is a soft breakdown in the irradiated detector which extends far beyond the original breakdown voltage before irradiation.

The irradiated GaAs material has been extensively investigated by the Freiburg group and, in particular, by Markus Rogalla [77]. The investigations at Glasgow centred on understanding the loss of charge signal. Many samples were produced in the, by now standardised, 3 mm diameter Schottky contact with guard ring format, tested for I-V, C-V and charge collection efficiency. These measurements were not able to help us in evaluating the source of signal loss. Illumination with an Am^{241} α source of both sides of the device provided the most important clue.

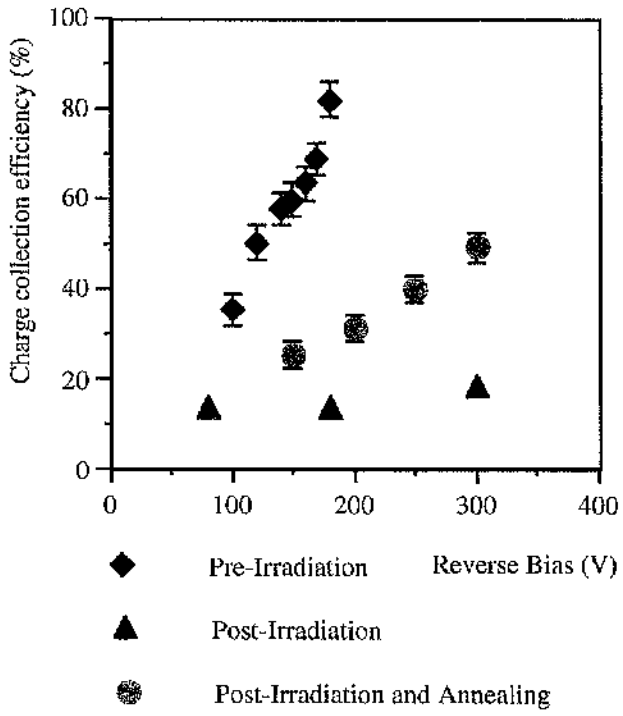

Fig. 4.19a. A 450°C anneal for 30 s shows a dramatic improvement in the overall charge collection efficiency.

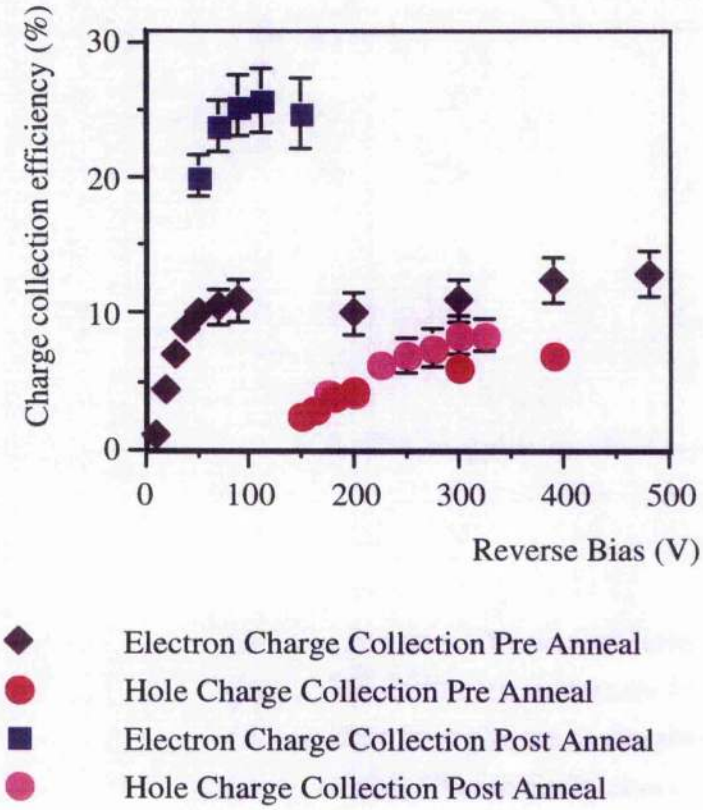

Fig. 4.19b. The anneal at 450°C gives a dramatic improvement to the electron lifetime in the material.

The contributions of each type of carrier were measured for irradiated samples and it was found that the contribution from both electrons and holes was severely diminished due to the radiation damage [112]. Annealing the irradiated sample at 450 °C for 30s improved the electron contribution considerably as arsenic anti-site defects can be removed by this process [113]. The plots in Fig 4.19 show the effect of the anneal stage on the carrier contributions to the collected charge.

Calculations by Chilingarov et al. [114] have resulted in the estimation of hardness factors which are used to adjust the damage due to the different non ionising energy loss (NIEL) from the various particles. Fig. 4.20 shows a plot of cce against integrated NIEL adjusted for the particles used in our irradiation tests. Using these figures and the expected integrated fluence over the 10 year lifetime of ATLAS it is expected that the signal from a 200 μm thick GaAs detector would be reduced by more than a factor of 3.

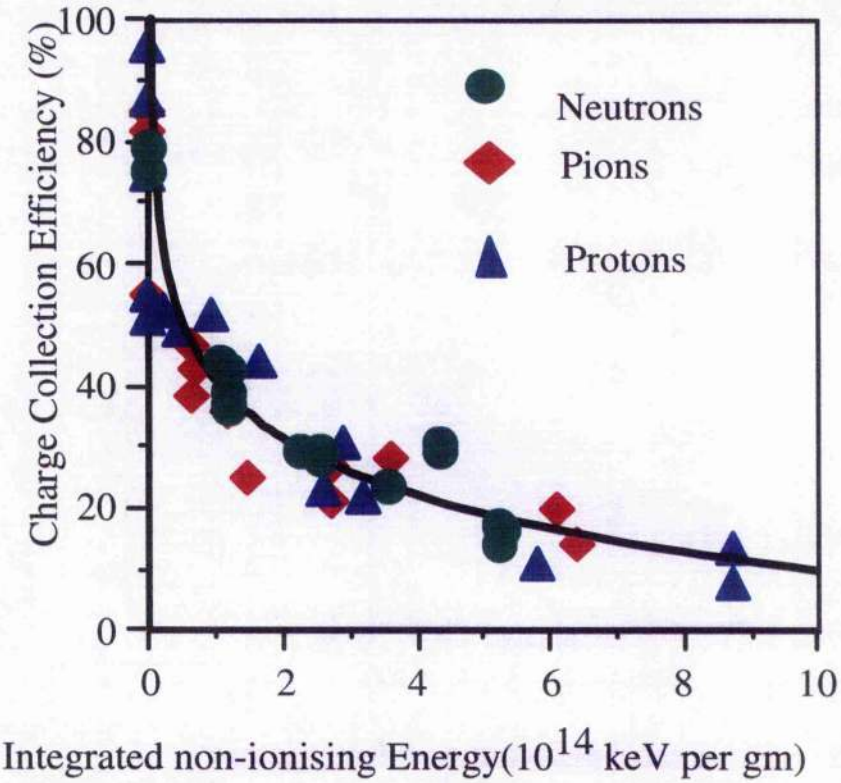

Fig. 4.20. C.C.E. as a function of NIEL normalised for the different types of particles used in the various irradiations.

The conclusion from studies of pion and proton irradiated GaAs samples is that the detectors would not stand the integrated radiation dose for 10 years of operation in the ATLAS detector as the signal would finally be smaller than the level required to maintain an acceptable signal to noise ratio.

Silicon detectors operating at -10°C have been successfully tested to equivalent fluences of $3x10^{14}$ protons cm^{-2}. The process and design for these detectors is of critical importance in determining their resistance to radiation. These factors, however, do not lead to a dramatic rise in cost – it means that the detector properties need to be very carefully specified at the outset. Their performance at this level of irradiation has led to this technology being adopted for use in the experiment.

Chapter 5: Pixel Detectors and Imaging

5.1 Motivation for and Early Development of Pixels in GaAs

Towards the end of the 1980's, research was beginning to focus on ways of instrumenting the next colliders for High Energy Physics experiments. The Superconducting Super Collider (SSC) was approved by Congress and, while it was known how to build the machine, there was very little that could be used to instrument an experiment that could be installed in it. The radiation environment would exclude the use of commercial electronics inside the calorimeter. While it was thought at the time that most of the physics aims of an experiment could be met using calorimetry alone it was felt that any developments that might help in realising a tracking detector would be extremely useful and find applications.

The LAA project at CERN was looking at ways of instrumenting experiments at future colliders. The project was organised so that novel detector techniques could be pursued in the main experimental detection areas such as tracking, calorimetry and muon detection. While GaAs was the object of the tracking section of LAA, one of the promising techniques for vertex detection that was investigated was based on pixels made on Si. If the pixel could be made small enough, the noise would never exceed a tolerable value at the extreme levels of irradiation foreseen close to the interaction point.

The technology of electronic design for integrated circuits was going through a fundamental reorganisation around this time as well, in that the concept of standardised cells for certain digital functions was just beginning to become a possibility. The potential for extending this to analogue cells was quickly recognised at CERN. The very substantial experience based on the evolution of these cells has been of tremendous value to the designers of all the subsequent versions of pixel read-out at CERN. The prospect of integrating the complex electronics on the detector, while very attractive, is not feasible when the yield of such a process is taken into consideration. The approach adopted was to design the read-out circuits on a separate wafer to the detector and then to bump bond them together. A solder bump bonding process (also known as flip chip, shown in Fig. 5.1), developed by GMMT at their Caswell laboratories, uses a system of wettable and non-wettable metals to define pads upon which a layer of solder is electro-deposited. The solder, when heated to the temperature at which it reflows, pulls itself into a sphere due to the surface tension of the liquid solder. The solder sticks to the wettable metal pad but

lifts off the non-wettable surface [78]. Bumps for the present generation of devices sit on an octagonal pad of 18 μm and have a diameter of about 22 μm on a 50 μm pitch for the short axis and 500 μm on the long axis.

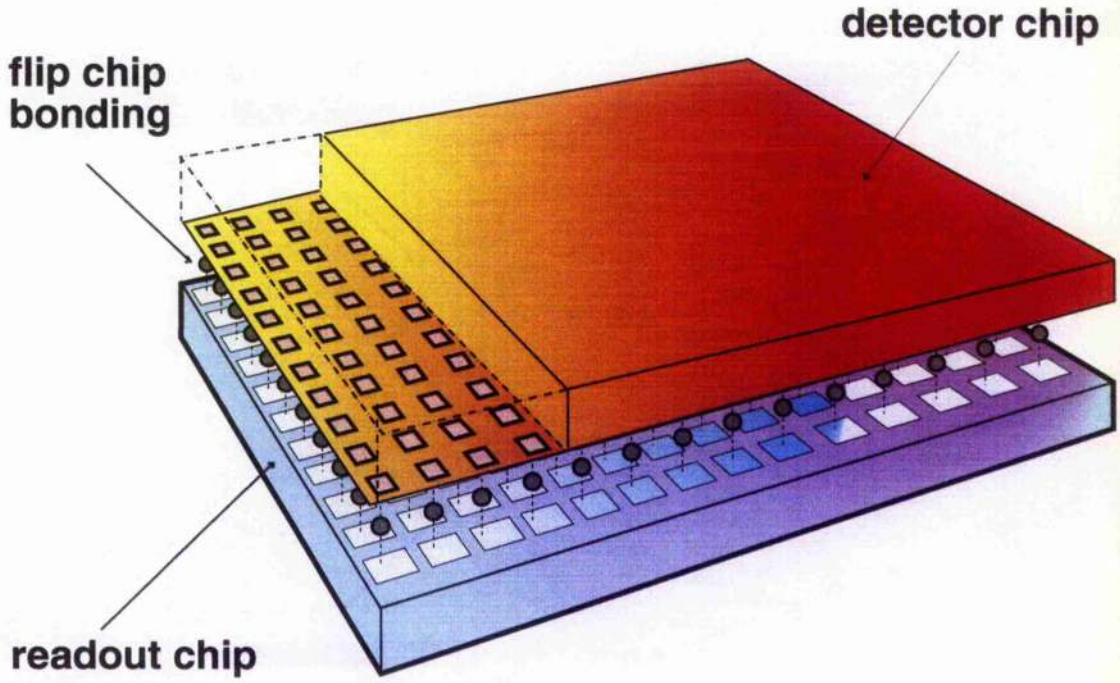

Fig. 5.1. The bump bonding concept shows the interconnection of two independent patterned substrates using a system of self-aligning solder ball contacts.

The pixels initially developed for HEP, as mentioned above, were not square. The area of the detector pixel is determined solely by the "real estate" required to realise the electronic function required of the cell to read-out the detector element. The detector elements cannot be smaller than the read out cell bumped on top of it. The bump size is not the limiting factor in the design, as it is possible to reduce this by a factor of at least two. The present circuit needs about 400 transistors for the amplifier, shaper, discriminator and register functions [79]. The area required for these transistors depends on the technology and is about 2500 μm^2 in the Faselec SACMOS 1 μm process. The pixel geometry has been dictated by the need to have a very good resolution on one axis only, because of the magnetic field configuration in the experiment for which it was designed.

Another important consideration for electronics of this type is that the power dissipation per channel has to be minimised. The present circuits are bonded to 2000

pixel elements so the permissable power dissipation per pixel has to be less than 100 μW if there is to be any reasonable means of cooling the assembly.

The latest family of "OMEGA" is capable of operation at 40 MHz while maintaining low noise and acceptable power dissipation. The use of a small detector element, which minimises capacitance and noise from the detector as well as giving a true 2-dimensional co-ordinate, has found many applications for pixel detectors in HEP.

5.2 GaAs Pixel Detectors

The first GaAs pixel detectors were fabricated in Glasgow primarily to see what would be needed to render the processing compatible with that required for bump bonding Si detectors. There was some initial concern that the gold would be leached by the solder and that contact would be lost or that the contact would be contaminated. To counter this possibility a barrier layer was deposited so that it covered the aperture in the nitride as illustrated in Fig. 5.2.

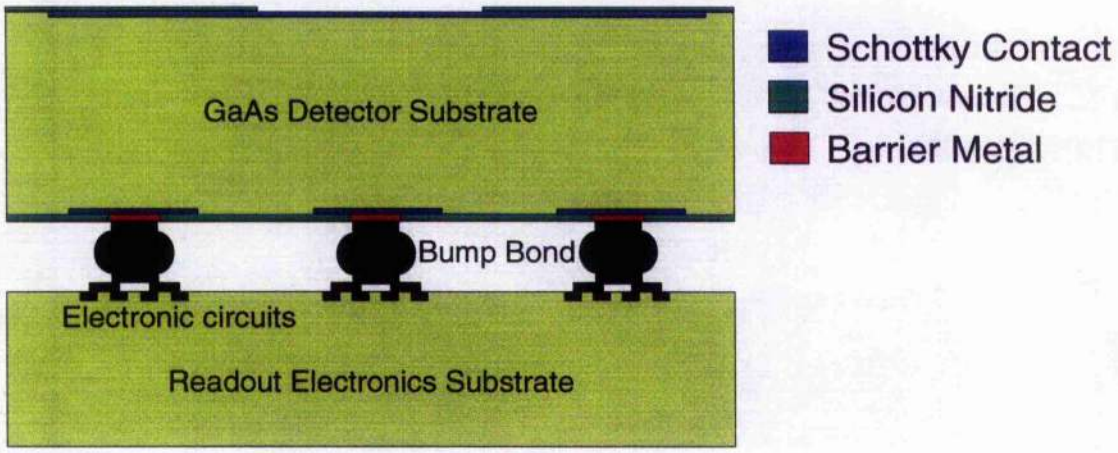

Fig. 5.2. Schematic outlining the assembly and metallisation for bump-bonding a GaAs detector to its appropriate readout chip.

Tests were carried out in which a second layer of titanium/gold was evaporated through the apertures and lifted off with a slightly larger diameter than the aperture to ensure that the Schottky contact was not contaminated by the bumping process. No discernible deterioration was found in the contact characteristics with the inclusion of this barrier layer. The bumps are deposited on the electronics substrate, on top of the patterned layers of wettable and non-wettable metals, by means of a plating process. A 63/37

tin/lead solder is used with a eutectic temperature of 183 °C [80]. After deposition of the required thickness of solder, the wafer is brought up to the reflow temperature. At this point the layer of solder pulls itself into an array of solder balls adhering to the wettable metal pads. Excellent uniformity of the solder ball size is achieved as the lithography used to determine the size of the deposited pads and the rate of deposition can be very precisely controlled, yielding a precise volume of solder per ball as indicated in Fig. 5.3. This process is carried out on a full wafer of read out electronics. When the wafer is diced, the working circuits (which have already been selected as Known Good Dice - KGD) are ready for bonding to a detector.

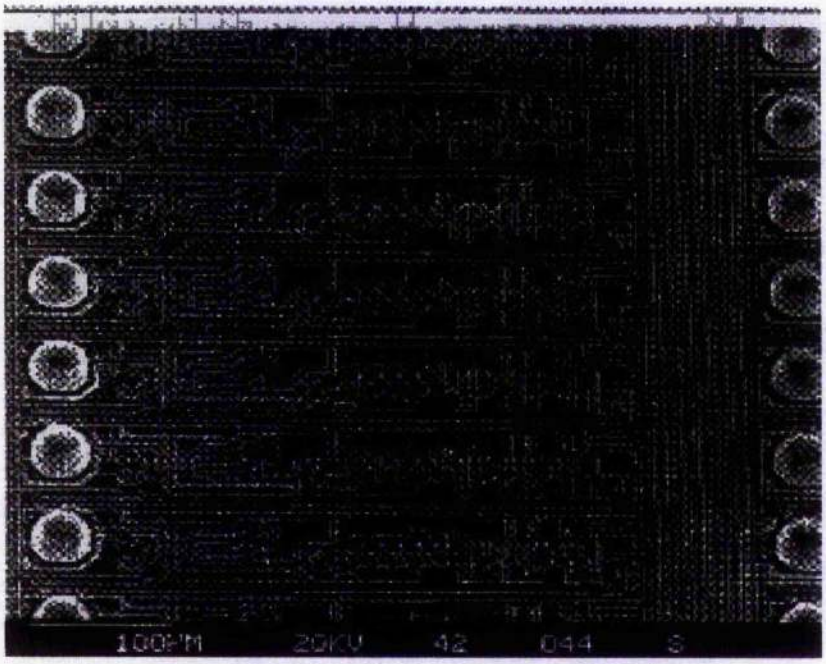

Fig. 5.3. A micrograph of the surface of a pixel read-out chip. The bump diameter here is 28 µm as this is from a previous generation of read-out circuits. The uniformity of the process is evident.

The GaAs detector is then aligned to an already bumped read-out chip at GMMT using a specialised bonding machine which has a precision of 1 µm when everything is correctly set-up. The substrates are pressed together and then heated until the solder melts and wets the pads of the detector. After the assembly has cooled it is visually inspected and is then ready for mounting onto a read-out board and electrical characterisation.

5.3 GaAs Pixels in the Test Beam

When a sufficient number of GaAs pixel detectors had been assembled, they were tested in a high energy pion beam at CERN using the Si pixel detector telescope developed at CERN for the RD19 collaboration, of which Glasgow was a member. The telescope (set-up by Dr. Cinzia Da Via'), consisted of three planes of GaAs detectors read out to a VME crate under the control of a FIC 68000 series processor. This was connected to a Macintosh-based acquisition and control package designed to read out the Omega series of chips.

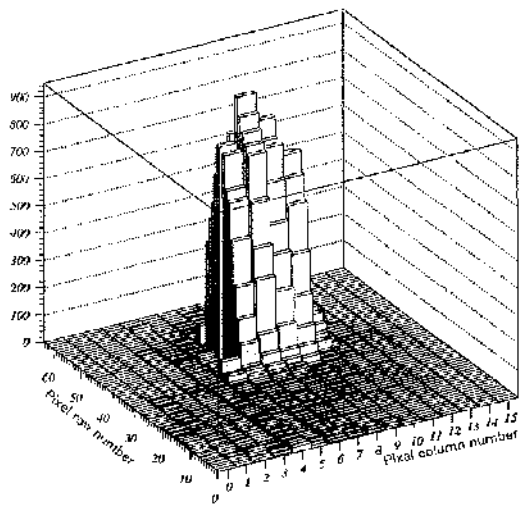

Fig. 5.4. The beam profile through one of the GaAs telescope planes. The sharp edges are due to the use of scintillators for beam definition. The noise hits are negligible.

The telescope was installed in the H6 beam line in the North Area of the SPS machine and 110 GeV/c pions were used to provide the data. Two of the detectors were used as anchor planes with their thresholds and biases maintained at a fixed value while the bias and threshold of the third plane were scanned to characterise that detector. When a complete scan was finished, the test plane was interchanged with one of the anchor planes and the process repeated. Fig.5.4 shows a profile of the beam through one of the GaAs planes.

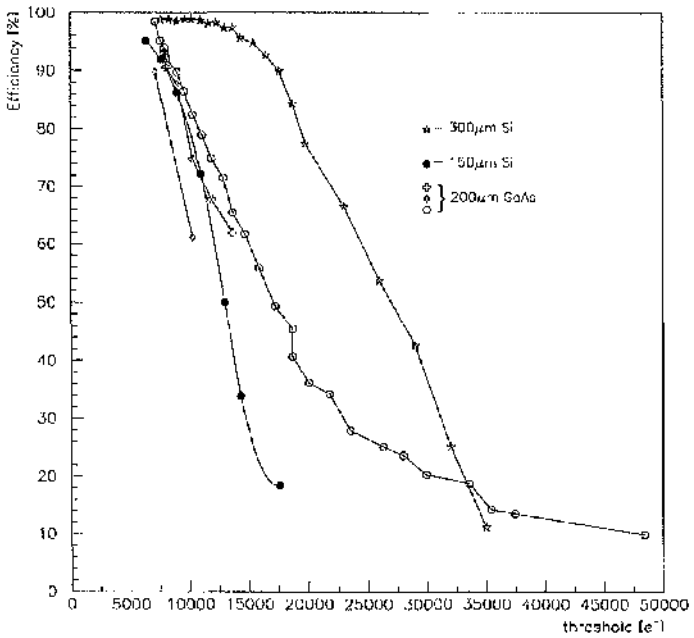

Fig. 5.5. A comparison of the detection efficiency for the three planes of the telescope with that for Silicon detectors of 150 and 300 μm thickness, scanning the comparator threshold.

The principal quantity of interest is the detection efficiency and how it varies with a comparator threshold scan, plotted for a variety of detectors in Fig. 5.5. The curve for Si shows a considerable efficiency plateau at almost 100% for a 300 μm thick detector. The absence of this plateau for the GaAs detectors was thought to be due to increased noise in the GaAs detectors but has never been adequately explained. Some very recent work using a different type of pixel detector, to be described in the following sections, may explain this type of behaviour, however.

The detectors worked very well in the telescope, even permitting the tracking of showers developing in the detectors themselves. There were very few noisy pixels when the threshold was properly adjusted. The technique of implanting back contacts has been used in the fabrication of pixel detectors (see 4.5), giving the same increase in breakdown voltage of the detectors as seen in micro-strips. The excess noise previously observed on pads is still present, indicating that all problems may not be solved merely by raising the voltage.

5.4 Pixel Detector Evolution

From an early stage it was noted that the read-out developed for HEP applications was very well suited for single photon counting in terms of electronic speed, power, and noise. The pixel shape, while suited for high precision about the magnetic bending axis, was not very suitable for imaging. The triggering requirement for reading out the device meant that it could not be read out efficiently without an external trigger which is not easily provided for photons. (This was addressed in later versions by the inclusion of a FAST OR of all the comparator outputs) [81]. The initial solution was to place an extra resistor in the bias line to the back contact of the detector and tap the signals from the back side to provide a trigger for the chip reading the same signals from the other side.

The disadvantage of this technique was that the noise on the back side was much greater because of the increased capacitance and leakage current of the much larger area of the detection element. This essentially limited the use of this technique to measuring the response to 60 keV Am^{241} gammas and higher energy photons.

Since the bump-bonding technique was easily adapted to detector materials other than silicon and GaAs would provide a much more efficient medium for X-ray imaging over the energy range of medical interest, it was decided to look more seriously at how one could adapt the pixels developed for HEP to an imaging application. At 60 keV, Compton scattering accounts for over half the interactions in any given thickness of Si while contributing to less than 7% of the counts in a GaAs detector [82]. The suppression of scattered photons, whether in the subject to be imaged or in the detector itself can only lead to enhanced image quality as this depends on the detected photons coming from a point-like source.

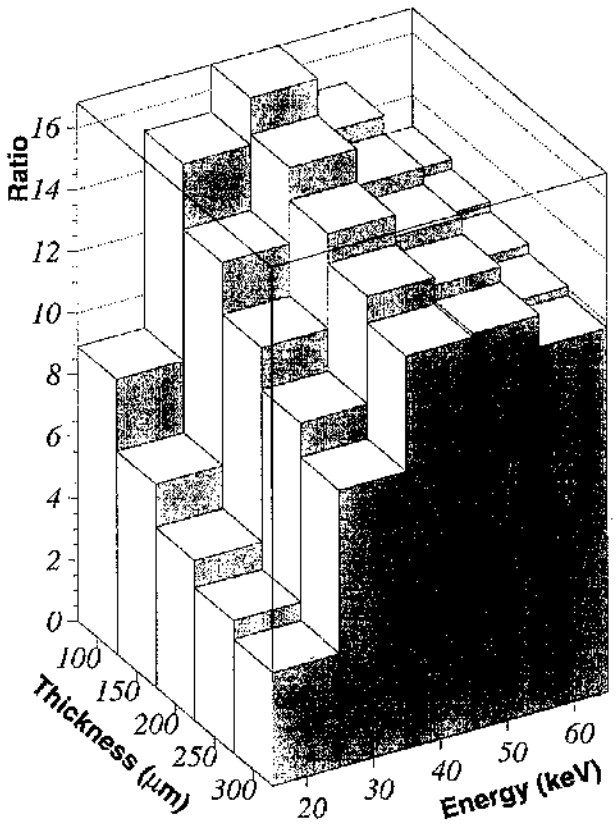

Fig. 5.6. Relative absorption efficiencies for various active thickness as a function of incident photon energy for GaAs/Si.

The absorption efficiency was calculated using EGS4 [83] to model the absorption in both Si and GaAs, including all the relevant conversion mechanisms for the energies simulated. Fig. 5.6 shows the ratio of absorption in GaAs/Si for a range of detector thicknesses in the medically interesting energy range. The enhanced photoelectric conversion cross-section in GaAs means that this simulation gives a realistic calculation of the improvement.

The prospect of significant dose reduction for radiology is a driving motivation for this type of development. The current method, using a film with silver halides, typically uses less than 1% of the incident photons for image formation. This can be increased slightly by coating the film with a phosphor screen. Recent developments in dental radiography use a Si CCD array to perform the image capture and a version which uses a layer of scintillator on top of the CCD to increase the conversion efficiency, with some loss of definition, has also been developed [84,85]. A comparison of the absorption efficiencies for Si, film and GaAs is shown in Fig. 5.7.

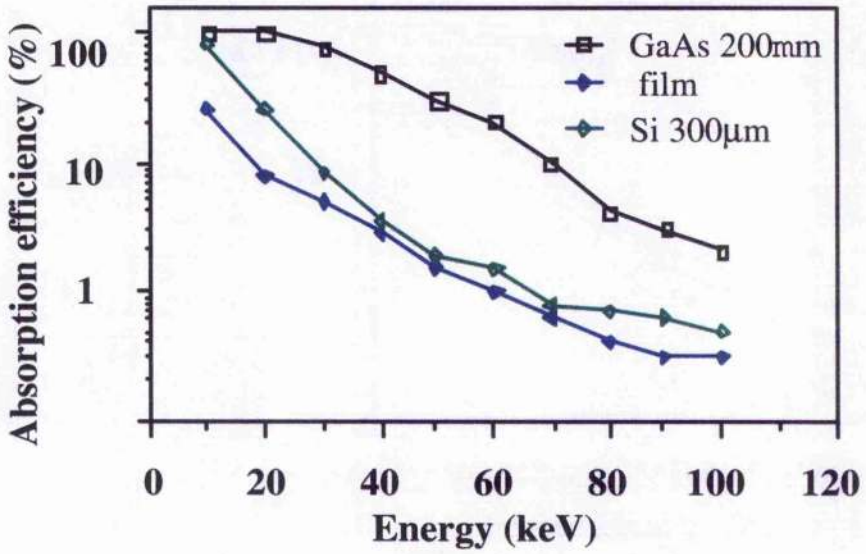

Fig. 5.7. A comparison of the absorption efficiencies of some detection media.

The attraction of developing an imaging system using a GaAs detector bump-bonded to a read-out chip based on the already developed Omega with square pixels and a counter on each pixel is immediately obvious. The design evaluation for this type of chip began in 1996. In order to take full advantage of this development, work on the evaluation of present GaAs detectors for use in imaging applications began at the same time. The group in Glasgow were instrumental in setting up the XIMAGE collaboration which secured EC Brite-Euram funding to develop X-ray detectors for dental intra-oral radiology [86]. Crude images had been made using X-rays and a variety of detectors to illustrate that imaging was possible but very little had been done to evaluate the quality of these images. The Omega chip was not ideal as a read-out chip because of the aspect ratio of the pixels. The issue of triggerability was not of crucial importance, however, as the photon flux from a commercial X-ray gun is high enough to give an acceptable efficiency. The solution to the aspect ratio was to scan the chip across the region of interest and evaluate the difference in counts for each step.

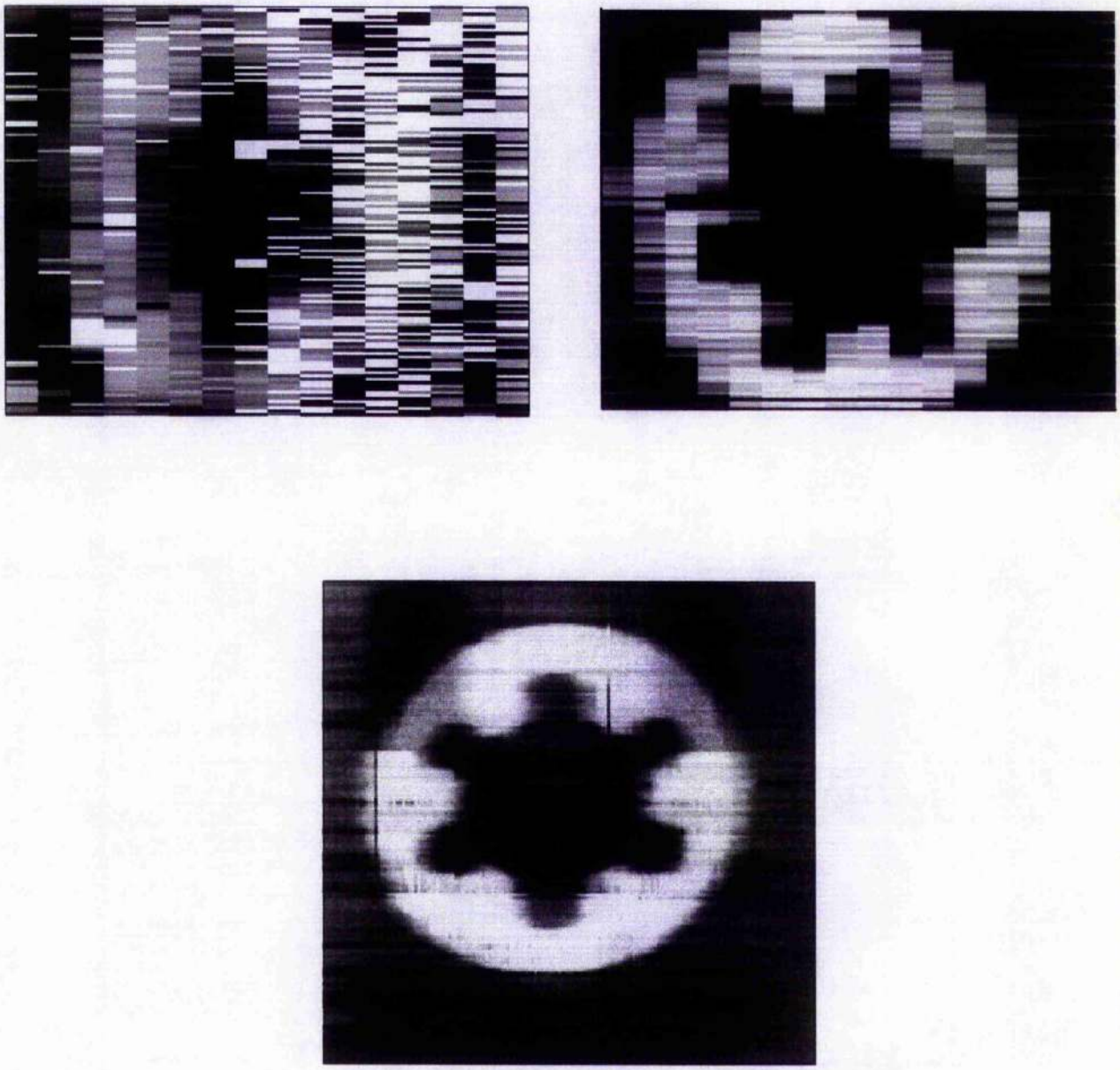

Fig. 5.8. Image evaluation using the Omega-3 read-out chip. The top left is a single shot using the whole array. The top right image uses the column with the least noise scanned in 500 μm steps. The bottom picture is an image built up by scanning in steps of 50 μm so that the steps on both axes are the same.

The preferred technique used to evaluate imaging systems involves measuring the sharpness of a well defined line exposed to the detector. For dental work, a 10 μm slit in a tantalum phantom is used in conjunction with a 70 kV X-ray gun. The data taken from a slit exposure give the line spread function (LSF) for the system. The data are then fitted to an analytical function [87] and Fourier transformed into frequency space where the

system efficiency is measured as a function of line pairs per mm. The resultant function is known as a Modulation Transfer Function (MTF) and is the most common yardstick used to evaluate imager performance.

The slit can be replaced by an edge to simplify the process and this characterisation has been done to evaluate the performance of an Omega-3 based GaAs detector and compare it against commercial CCD's and previously published results as shown in Fig 5.9. The data from the exposure are fitted to a Gaussian distribution with an exponential to approximate the cusp-like shape of the LSF using 5 parameters of the form

$$LSF(x) = a_2 \exp\left[\left(\frac{-(x-a_1)}{a_3}\right)^2 \bullet \frac{1}{2}\right] + a_4 \exp\left[\frac{-|x-a_1|}{a_5}\right] \tag{5.1}$$

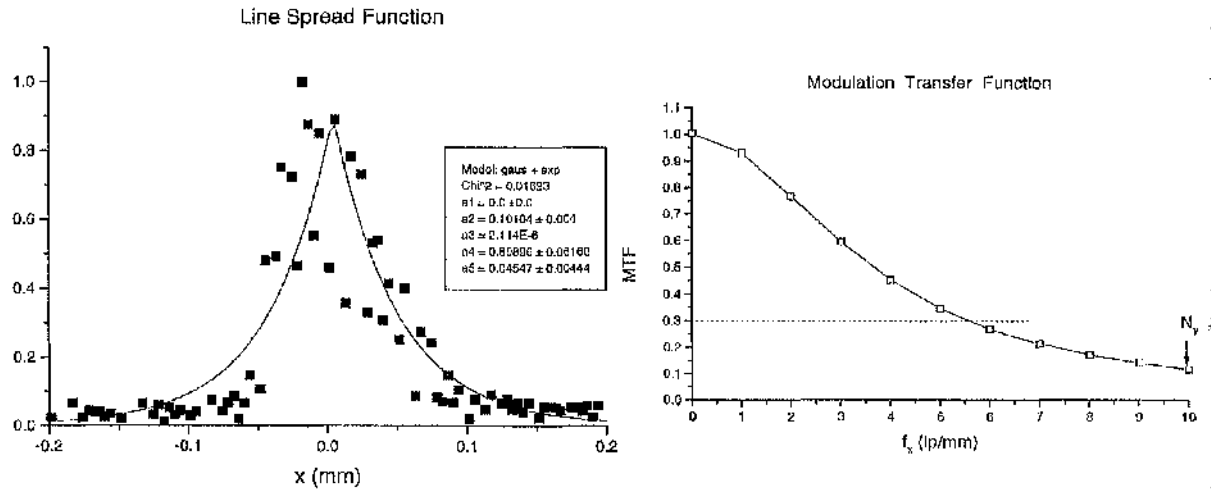

Fig. 5.9. The data points for a slit exposure of a GaAs detector with Omega-3 read-out are used to fit to a cusp-like LSF which is then transformed to give the MTF.

The number of line pairs/mm at 30% MTF is taken as a standard reference point for image comparison. In the comparison of MTF's in Fig. 5.10, the effect of the scintillator is clearly seen as a loss of resolution [88]. The pixel size in the CCD was 45 μm, while the slit was imaged across the 50 μm axis on the Omega detectors. The performance of the Omega detectors is comparable to that of the CCD's. The fact that the CCD pixels can

be made much smaller does not really gain much, as the dose required to minimise photon number fluctuations increases as the area decreases. The clinical features that can aid diagnosis are all adequately imaged with pixels of around 50 μm dimensions.

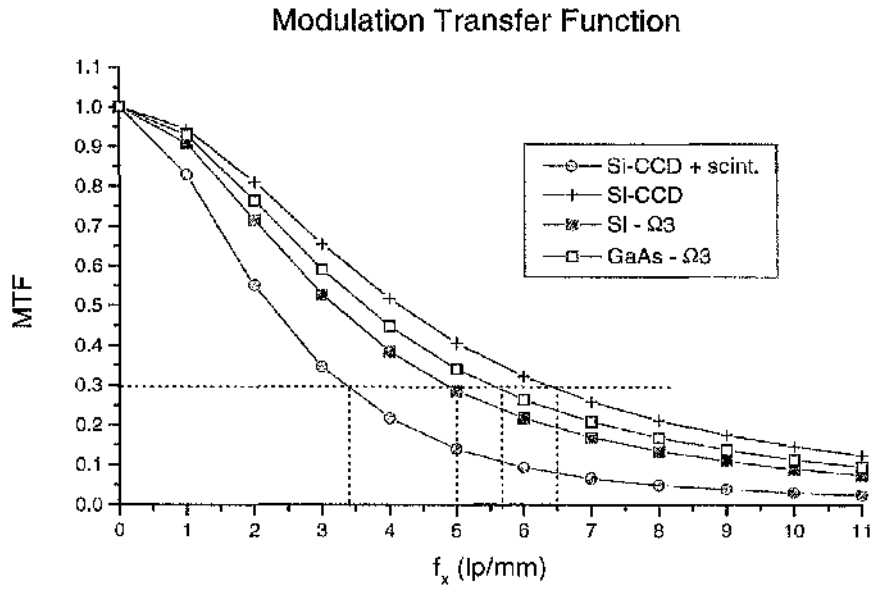

Fig. 5.10. A comparison of the MTF's measured in order to characterise bump-bonded pixels as imaging devices.

The pixel performance depends entirely on the electronics designed for the read-out. The next section describes a photon counting chip designed specifically for imaging by the Microelectronics group (MIC) at CERN, in close collaboration with the Universities of Freiburg, Glasgow and Pisa.

5.5 Photon Counting Pixels

The photon counting chip designed at CERN, called the MEDIPIX is an array of 64x64 pixels, each 170 μm square. As illustrated in the schematic of Fig. 5.11, each pixel cell consists of a front-end amplifier and comparator almost identical to those used in the Omega series of devices. The discriminator output is shaped and fed into a 15 bit counter which can be read out after an exposure. Each cell is equipped with a 5 bit register which controls the cell function. Two bits are used for selection of a test mode or to mask the

pixel in the case where it is bonded to a 'hot' (noisy) detector element. The remaining three bits are used to implement a threshold adjustment function. The circuit layout is shown in Fig. 5.12.

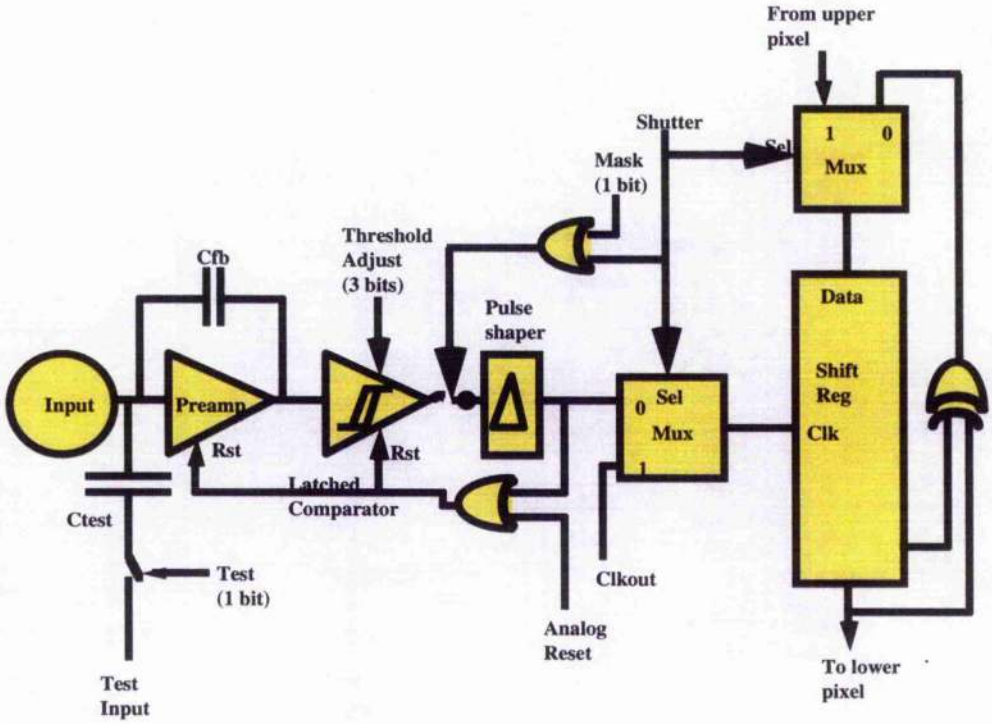

Fig. 5.11. A schematic layout of a single cell of the MEDIPIX chip. The counter is a variation on a pseudo-random generator which can be realised using a minimum number of transistors and can also be used as a shift register for read out.

The layout of the pixel cell illustrates some of the problems facing the designers of such high performance circuits [90]. The analogue circuitry takes up almost 60% of the pixel area and is the dominant factor in determining the minimum pixel size that can be achieved. The digital circuitry and busses can be seen to the right of the cell and it is clear that the layout of this part of the circuit is much more compact as the constraints on digital interconnection and routing are much less restrictive than those for analogue placement. The input transistors and the decoupling capacitor to the comparator are the space-consuming components in the analogue section [91].

The chip was submitted for fabrication in the spring of '97 and first results of tests began to appear in the autumn of that year [89]. A major problem with previous generations of similar devices was that the variation in the threshold value across the chip was many times greater than the noise that was generated on each detector element. The pixel detector for HEP developed prior to MEDIPIX incorporated an adjustable delay to enable greater precision in the trigger timing and take into account time walk differences

in pixels. The same idea was applied to the comparator threshold in the new chip. This had the effect of reducing the variation across the chip by an order of magnitude, as shown in Fig. 5.13.

An evaluation is already under way to estimate the improvements that may come from switching to the new 0.25 μm process which is available from IBM. The present 1 μm SACMOS process offers a very much higher packing density than usual for this line size but the smaller feature size available in the new process, as well as an increased number of interconnection layers, would permit a considerable reduction in the overall pixel size. A pixel dimension of 50 μm square is the goal for dental imaging while it is believed that pixels closer to 200 μm square would be suitable for mammography [92]. The principle of single photon counting means that the development of the electronics should always strive for the smallest possible pixel size, as 'super pixels' can be created by combining data from smaller pixels offline without any statistical loss.

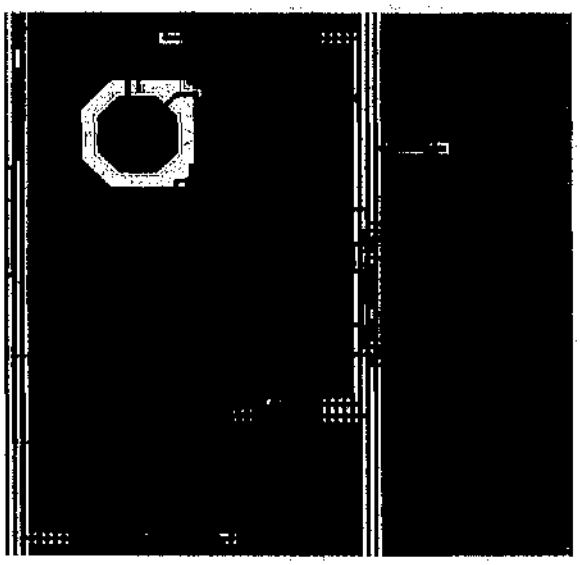

Fig. 5.12. A cell layout of a photon counting pixel cell. The bus through the middle separates the analogue section on the left from the counter on the right. The control register is on the bottom right of the analogue section as it remains quiet during acquisition.

The new process should be inherently more radiation hard as the gate oxides used are much thinner, and indeed preliminary measurements confirm [120] this, so it is appropriate for the MIC group at CERN to plan to migrate to these emerging processes. Some aspects of the simulation of noise performance for devices fabricated in these advanced processes have not been developed to the same level as for the current process. This may provide some surprises in the chip performance but should be regarded as part

of the "learning curve". The gains offered by the new technology far outweigh the potential hazards that may be encountered in the initial runs.

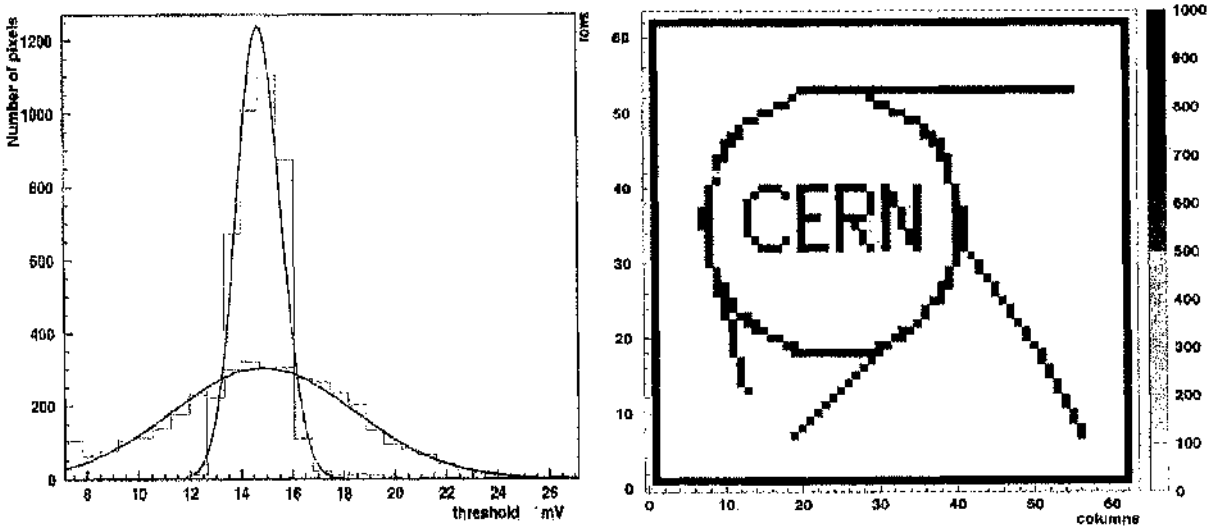

Fig. 5.13. The threshold variation, shown on the left, before and after tuning the registers shows a reduction from 350 to about 80 e- r.m.s. The logo is the result of 1000 pulses of 3300 e- on a threshold of 2250 e-. One noisy pixel is evident as well as an inefficient one in the pattern.

5.6 Integrating Pixels

The common approach to acquiring an image is to integrate the charge created in the detector and then read out this value for each pixel after the exposure. The operation of the CCD is one example of this method. IMC in Stockholm have developed a charge integrating read out chip different from a CCD. Their chip was designed to read out the charge created in a Quantum Well Infra-red Photodiode (QWIP). The electronics are produced as CMOS devices which are then bump-bonded to the pixellated detector. The cell circuit consists of a front-end transistor, a storage capacitor and some addressing logic. Because there is virtually no signal processing the pixels can be very small. The readout chip is produced as an array of 240x320 pixels, each 38 μm square. The detector is bump-bonded to the read-out using an indium bump-bonding process which has been developed at IMC [93].

The bumping consists of the evaporation of a barrier of NiCr patterned over the top metallisations that are to be bumped. This barrier overlaps the aperture opened in the nitride, to prevent any contamination. A thick photo-resist is then used to define the position of the In bumps which are evaporated to a thickness of 7 μm. The result is an

array of bumps 12 μm in diameter and 7 μm high on both the read-out and detector wafers. The wafers are then sawn and the dice are ready for assembly. The assembly is done on a Karl Suss machine which is specially designed to yield precision alignment in all planes for both pieces and then press them together with a precisely controlled force.

It was apparent that this scheme should also be suited to reading out a pixellated X-ray detector made from GaAs. Detector arrays were therefore designed and fabricated on 200 μm thick 2" LEC GaAs substrates at Glasgow and sent to IMC with the extra masks needed for bump definition and assembly. The assembled detectors were tested using a dental X-ray generator in Sundsvall in northern Sweden. The first results show that the array works well as an imager and is capable of resolving a 25 μm Al bond wire across the back of the detector [94] as can be seen in Fig. 5.14. The pixel size is small enough and the array size large enough to permit an evaluation of the homogeneity of the material. It appears that there is an 25% variation in detector cce in highly localised areas across the array.

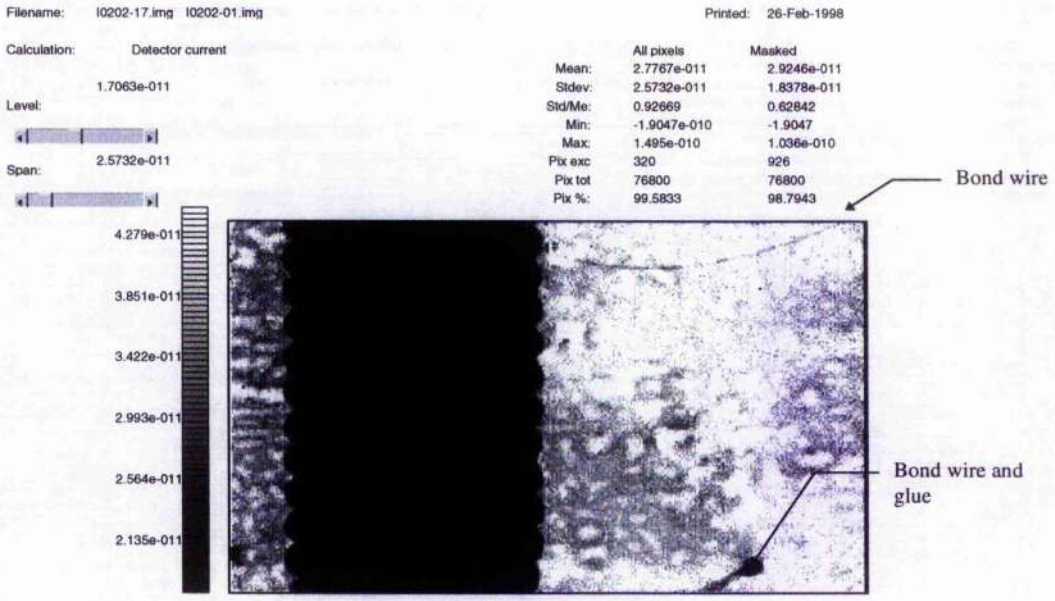

Fig. 5.14. An 18 ms exposure to a dental X-ray set (70 kV anode voltage) captured on an array of 38 μm square pixels bump bonded to a charge integrating readout chip. The dark outline is the image of a screw with an unusual thread and the bond wire is 25 μm in diameter.

Further work needed to establish the nature and origin of the variations is part of the XIMAGE work programme. A series of images captured with a lower resolution but at video frame speed show a low frequency change in the leakage current as the bias is applied. Whether the source of this effect is related to the detectors or the electronics is still unclear and is being investigated. This may indicate the need for a more uniform

material however, and so brings us conveniently to a description of the work that has been done on epitaxial growth as a means of producing such superior quality material.

5.6 Epitaxial Material for Detectors

Initially, the interest in epitaxially grown GaAs was as a means of extending its radiation hardness. Latterly, however, it is seen increasingly as the most promising way of producing detector grade material commercially. This material would have a trap density orders of magnitude lower than that in commercially pulled LEC or VGF crystals (typically 10^{16} cm^{-3}), a free carrier density less than 10^{13} cm^{-3} and a thickness over 200 μm. Such a material has yet to be produced with all of these qualities at the same time. Material with an acceptable free carrier density has been grown using Liquid Phase Epitaxy (LPE), but the growth process becomes unstable for thick layers. The surface of a thick layer of LPE material has a terraced appearance as growth proceeds at different rates in different areas. This renders it unsuitable for processing and attempts to make good detectors on thick layers of this type of material have been unsuccessful to date

A technique has been developed comparatively recently [95] to grow epitaxial layers of GaAs at a high rate with good surface morphology using a Low Pressure Chemical Vapour Deposition (LP-CVD) technique. By reducing the pressure in the reactor, it has been shown that the growth rate can be increased to 150 μm hr^{-1}. With this growth rate it should be commercially feasible to grow layers thick enough for detector use if the other properties of the layer needed for production of good detectors can be met. A study of these prospects is being undertaken as part of the XIMAGE project by Aixtron plc. of Aachen. Currently, epi-layers have been produced with a free carrier concentration in the region of 1.5 X 10^{14} cm^{-3} with a layer thickness of 50-100 μm.

The low pressure CVD techniques pioneered in Aachen have already been used by an American company, Epitronics [5.19] to produce material with carrier concentrations of 2-3x10^{14} cm^{-3} which has been extensively tested in Glasgow. The substrates were Si doped so that there was no need to thin the wafers before fabrication. A number of "standard" 3mm pad detectors was fabricated on the material after it had been chemically polished to planarise the surface [96]. The surface had a dull appearance with slight undulations before polishing due to thickness variations as illustrated in Fig. 5.15.

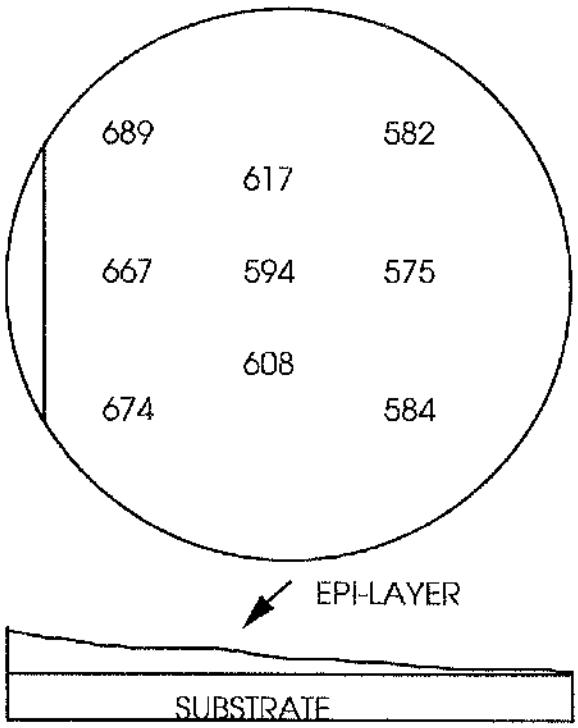

Fig. 5.15. The measured variation in epi-layer thickness across the wafer. The gradient is thought to be due to the way the gas flow is controlled in the reactor. It should be possible to remove it by modification of the reactor glassware.

The substrates were 450 μm thick, Si doped to 10^{18} cm^{-3} and supplied by Hitachi Cable. As these were the first epi-wafers to be processed, it was decided not to use an abrasive polish on the epi-layer. In hindsight this was a mistake, as the surface irregularities were large enough to ensure that the mask did not make good enough contact to define the guard rings properly. The wafer was polished with our standard chemical polish (see 3.3) to remove about 30 μm. This removed the localised variations on the surface, changing it to a mirror like surface. The large variations were still evident and led to the difficulties described above. It is never easy to decide how much to thin an already thin film in order to achieve the optimum result.

The test pads on this material exhibited a much higher leakage current than that seen on similar pads on SI material, due to the shorted guard rings. This was not a problem due to the material but was a hindrance to accurate measurement. The capacitance vs. bias voltage curves for the devices showed no variation with the measurement frequency and a linear behaviour when plotted against $1/C^2$, as shown in Fig. 5.16 [97]. The free carrier concentration was calculated from the slope of this graph to be $3x10^{14}$ cm^{-3}.

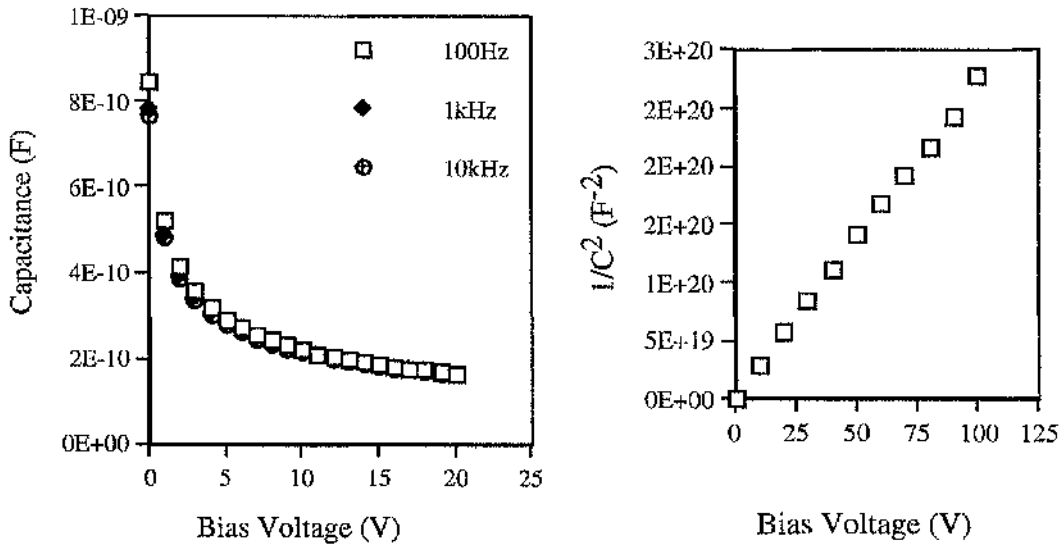

Fig. 5.16. Capacitance measurements on the material supplied by Epitronics indicate that the material has a low concentration of traps and behaves as a classical semiconductor.

One detector sample was tested using Deep Level Transient Spectroscopy (DLTS) in an attempt to measure the density of deep levels present in the material. Some deep levels were seen at a concentration of around 10^{14} cm^{-3}, two orders of magnitude lower than the levels encountered in LEC pulled crystals. The measurements of charge collection using X-ray spectra showed 100% charge collection – a spectrum of Tb X-rays is shown in Fig. 5.17. The devices were unable to resolve X-ray energies lower than 36 keV (Ba), because of the high leakage currents and associated noise due to the shorted guard rings.

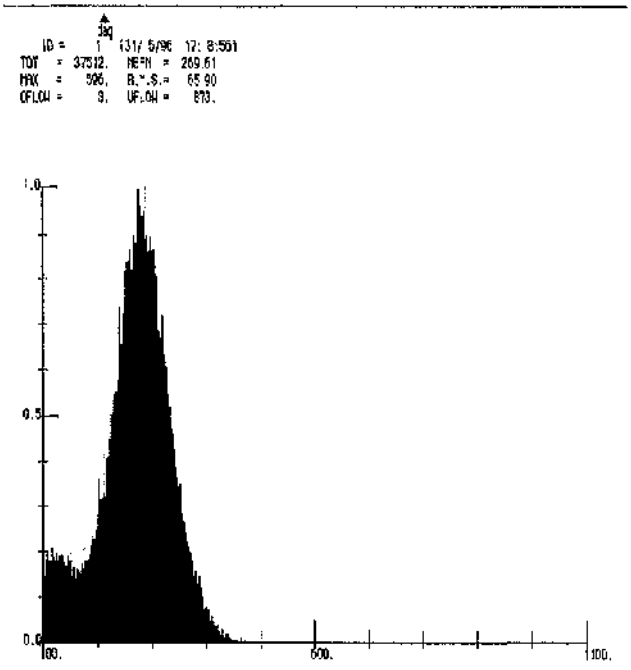

Fig. 5.17. The spectrum obtained from 44 keV Terbium X-rays in a 3 mm diameter pad detector. The detector was made on a 130 μm thick epitaxial GaAs layer supplied by Epitronics Corp. The data were obtained at a bias of 100 V at -20°C to reduce the leakage current.

Chapter 6. An Optical Readout.

6.1 Motivation

The principal limitation in the use of bump bonded pixel detectors is that the pixel size will always be limited by the silicon "real estate" needed to realise the electronics that sit on top. The tendency of circuit designers to want to provide more functionality to their circuits will always go against the reduction of pixel size. At one of the first GaAs detector workshops in Erice, it was suggested by Prof. J. H. Marsh that the read-out of the detector could be achieved using an optical modulator whose reflectance is controlled by the charge liberated in the detector. This could be achieved with the use of a reflective electro-absorption optical modulator coupled directly to the detector element [99].

The advantages of such a scheme would be that the detector element size would no longer depend on the read-out complexity bonded to it as this processing would be performed remotely. Indeed, the pixel size needs to be as small as possible to drive the modulator effectively. The smaller the modulator capacitance, the larger the drive voltage created by the charge. The modulator stack and small signal equivalent circuit shown in Fig. 6.1 give some idea of the proposed arrangement.

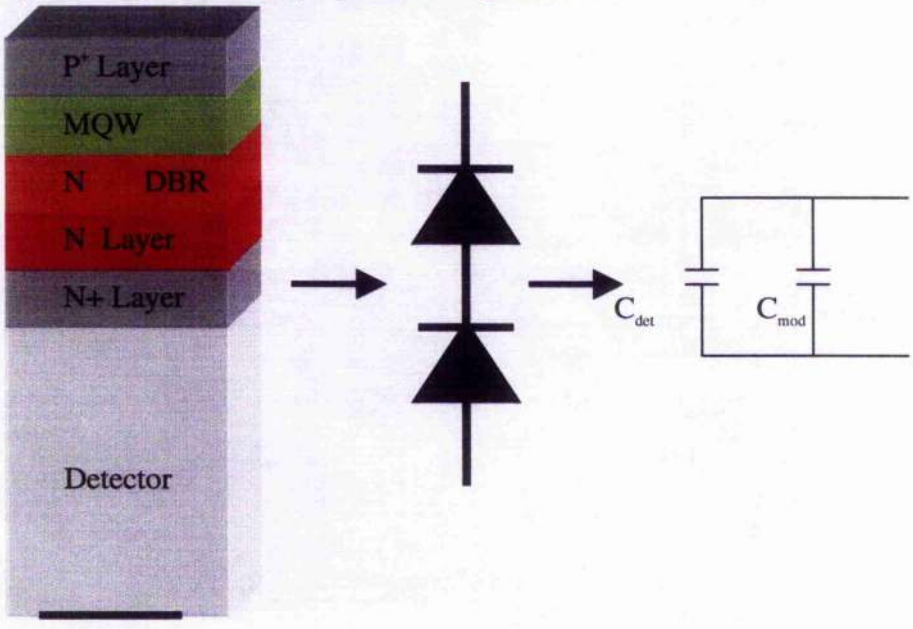

Fig. 6.1 An outline of the implementation of the reflective modulator using a Distributed Bragg Reflector (DBR) and Multi-Quantum Well (MQW) modulator integrated to a radiation detector. The structure functions as a pair of series diodes and reduces to the small signal equivalent circuit shown.

Optical modulators had already been fabricated with some success in Prof. Marsh's group [100]. These modulators were of the single pass type (no reflector stack) but exhibited characteristics indicating that they might have a sufficiently low drive voltage to make them interesting for this application. The structure, 100 pairs of wells coupled by thin barriers, gives a total thickness of 1.68 μm for the active volume of the modulator. A pixel area of 16 μm^2 gives a capacitance of 1 fF per pixel for this thickness. A signal of 12500 electrons provides a drive voltage of the order of 2 Volts.

The following sections describe the theory involved and the design and fabrication of test structures to study the suitability of this technique.

6.2 Theory of Operation of Modulator and Reflector

The Distributed Bragg Reflector (DBR) is the common way to achieve very high reflectance structures in multi-layer devices grown by epitaxial techniques. The reflector is composed of alternating layers of material with differing indices of refraction, the optical length through each layer being a quarter wavelength of the design operating wavelength for the stack. The partial reflections from each refraction discontinuity sum constructively to yield a mirror with a high reflectance band at the wavelength of interest.

The reflectivity, R, for such a sequential stack of N pairs (periods) of layers [101] can be calculated to be:

$$R_{\max} = \left[\frac{\left(\frac{\eta_{inc}}{\eta_s}\right) - \left(\frac{\eta_A}{\eta_B}\right)^{2N}}{\left(\frac{\eta_{inc}}{\eta_s}\right) + \left(\frac{\eta_A}{\eta_B}\right)^{2N}} \right]^2 \qquad (6.1)$$

It can also be shown that the reflectance pass-band for such a structure is:

$$\frac{\Delta\lambda}{\lambda_0} = \frac{4}{\pi}\sin^{-1}\left(\frac{|\eta_B - \eta_A|}{\eta_B + \eta_A}\right) \tag{6.2}$$

where η_{inc}, η_s, η_A and η_B are respectively indices of refraction for the material from which the light is incident, the substrate behind the stack and the materials A and B used to form the alternate layers of the stack. λ_0 is the design central wavelength for the mirror. These formulae do not take into account any absorption that occurs along the optical path of the device. It is evident that the maximum reflectance of the stack increases with more layer pairs as well as with increasing difference of the refractive indices of the layer materials. For the design of a reflector for this study, a DOS-based PC program [101] known as the Dielectric Thin-Film Reflectance program was used to simulate the stack performance prior to device growth.

The change in absorption of light at energies close to the band gap of a semiconductor under an applied field is used to modulate the passage of light in this type of device. The effect can be seen in bulk GaAs and is known as the Franz Keldysh effect, proposed independently by Franz and Keldysh [102, 103] in 1958. In Multiple Quantum Well (MQW) structures, the absorption is very much enhanced by the Quantum Confined Stark Effect (QCSE) [104] which is a very different effect to that seen in the bulk and can be responsible for a much stronger change in absorption.

The quantum well is realised by using a thin layer of pure GaAs surrounded by barriers of $Al_xGa_{1-x}As$ which have a higher band gap and serve to confine the carriers in the well. The wells and barriers are grown by epitaxial methods as sequential layers whose thickness and composition can be very precisely controlled. The width of the well must be kept small (the effect disappears for wells wider than about 300 Å) in order to prevent the ionisation of excitons. An exciton may be considered as an electron hole pair, which are still bound together by the Coulomb attraction.

The Schrödinger equation may be used to solve the wave functions for a potential well which resembles that formed in a real as-grown quantum well. The solution for a step potential of infinite height is modified to take into account the finite difference in band gap energies between the well material and the barrier. The diagram in Fig. 6.2 illustrates the conditions found in the model for a finite quantum well. The finite well has a depth V and width a. If E is the energy of a state, measured from the bottom of the well B = V – E

is known as the binding energy and is the energy required to remove the electron from the well.

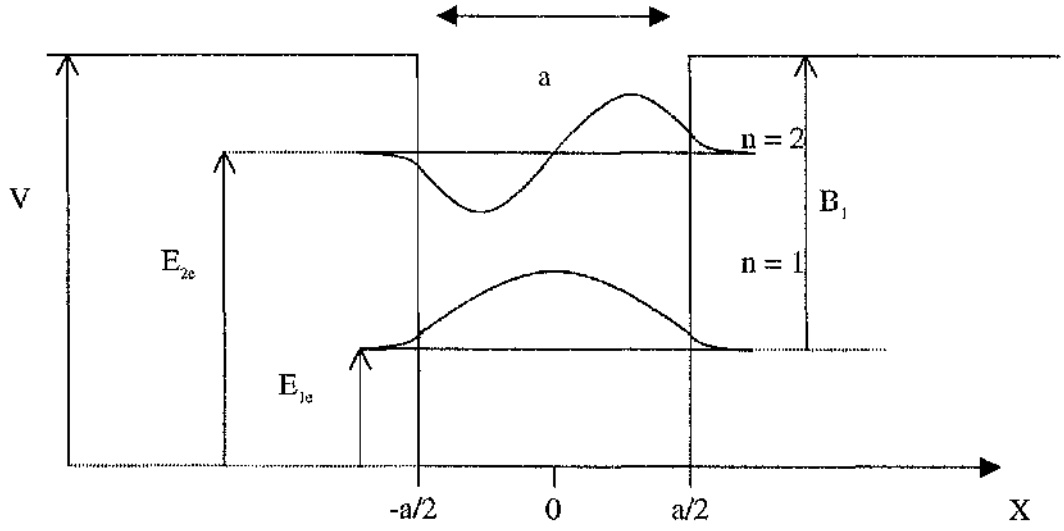

Fig. 6.2. Finite Quantum Well model parameters.

Inside the well, the solution of the Schrödinger equation yields:

$$\Psi(x) = \alpha \sin kx \qquad \text{where} \qquad k = \sqrt{\frac{2mE}{\hbar^2}} \tag{6.3}$$

for each even (n = 2, 4 etc) state of energy E, while the solution for the conditions outside the well gives

$$\Psi(x) = \beta e^{-\kappa x} \quad \text{where} \quad \kappa = \sqrt{\frac{2m(V-E)}{\hbar^2}} \tag{6.4}$$

the wave function ψ and $\frac{1}{m^*}\frac{d\psi}{dx}$ need to be matched at x = a/2 giving

$$\alpha \sin ka/2 = \beta e^{-\kappa a/2} \tag{6.5}$$

and

$$k\alpha \cos ka/2 = -\kappa\beta e^{-\kappa a/2} \tag{6.6}$$

Division and substitution of θ for ka/2 yield

$$\cot\theta = -\kappa/k = \sqrt{\frac{\frac{mVa^2}{2\hbar^2} - \theta^2}{\theta^2}} \tag{6.7}$$

This equation has no algebraic solution and must be solved numerically, however the series of equations above allow the following conclusions to be drawn:

1) There is always at least one bound state present in the well.

2) There are N solutions for the condition $(N-1)\frac{\pi}{2} < \sqrt{\frac{mVa^2}{\hbar^2}} < \frac{N\pi}{2}$

In a quantum well, the distribution of available states changes from the continuous band observed in the bulk lattice to a number of discrete levels which are confined by the potential well. The density of states available to absorb light of a high enough energy in this two dimensional lattice is stepped in energy as shown in Fig. 6.3.

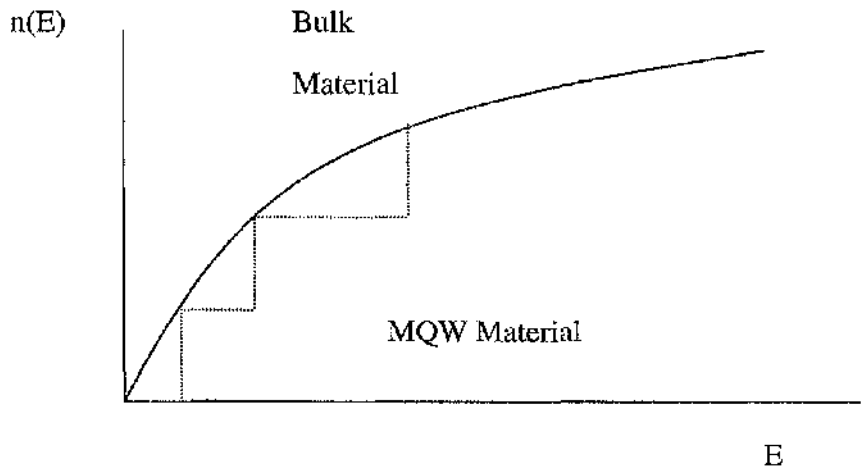

Fig. 6.3 An illustration of the quantised nature of the energy states available in an MQW design. The step increase in state density leads to sharply defined features in the optical properties of MQW structures.

In the classical Franz-Keldysh treatment, the absorption of photons with energy just below the band gap is made possible by the band broadening induced by an applied electric field which increases the probability of absorption. The applied field also increases the field ionisation of excitons which has the effect of broadening the feature and reducing excitonic absorption.

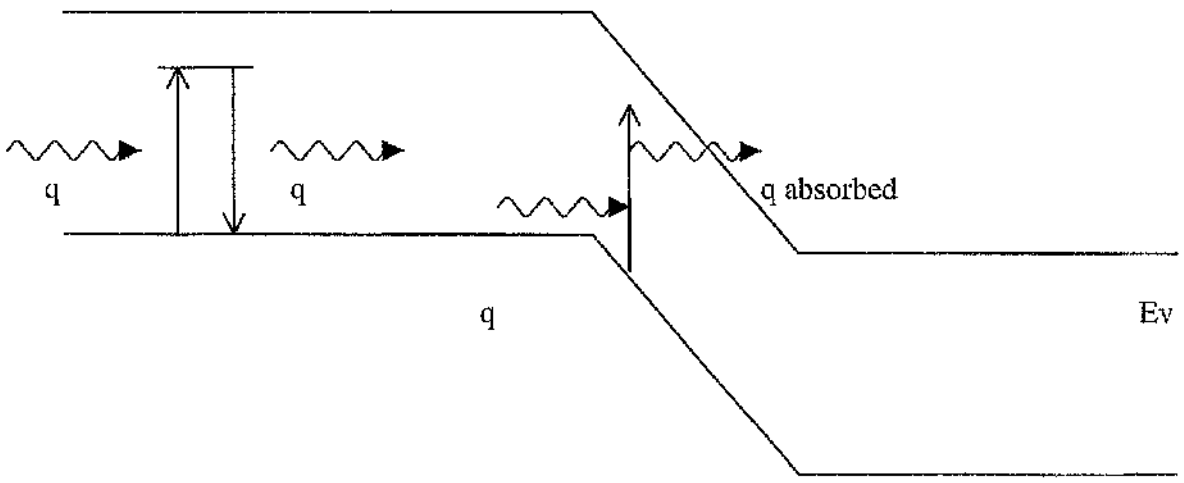

Fig. 6.4. The effect of the applied field on the band gap. The absorption of photons with energy just under that of the gap is enhanced by the applied electric field.

The effect encountered in MQW structures is markedly different. Absorption is enhanced by band tilting, as described in Fig. 6.4. The dominant excitonic features,

extinguished by the applied field in bulk material, remain in MQW structures even with high applied fields. In the presence of an applied field, the electrons and holes comprising the excitons are pulled apart by the field but constrained by the walls of the potential well. The Coulomb attraction between each hole and electron is weakened by the separation and so the binding energy of the exciton is reduced.

6.3 Device Design, Growth and Fabrication

Based on earlier work on transmission modulators by members of the opto-electronics group at Glasgow [105], a natural starting point was to take a proven modulator recipe, and couple it to a DBR designed to have a high reflectance at the operating wavelength of the modulator. The most promising modulator structure was based on pairs of coupled wells. This structure was achieved by making alternate barrier layers thin enough to allow significant tunnelling between pairs of wells so that the levels split. Theory predicts that this type of structure should be sensitive at much lower drive voltages than modulators based on conventional MQW structures. This is due to the fact that pairs of wells are resonantly coupled, the discrete levels seen in isolated wells split into pairs in adjacent coupled wells as shown in Fig. 6.5. In the absence of an electric field, only transitions between electron and hole states of the same symmetry (S) are allowed. On the application of an electric field all transitions are allowed, as the wave function symmetries become distorted. The transitions 1 and 3 move to lower energies while 6 and 8 move to higher energies on the application of an electric field. The overlap of the wavefunctions is enhanced for asymmetric transitions and diminished for symmetric transitions. On the application of a small electric field, the resonant coupling between wells is destroyed, leading to a blue shift in the absorption band followed by the classical red shift as the field is increased [106].

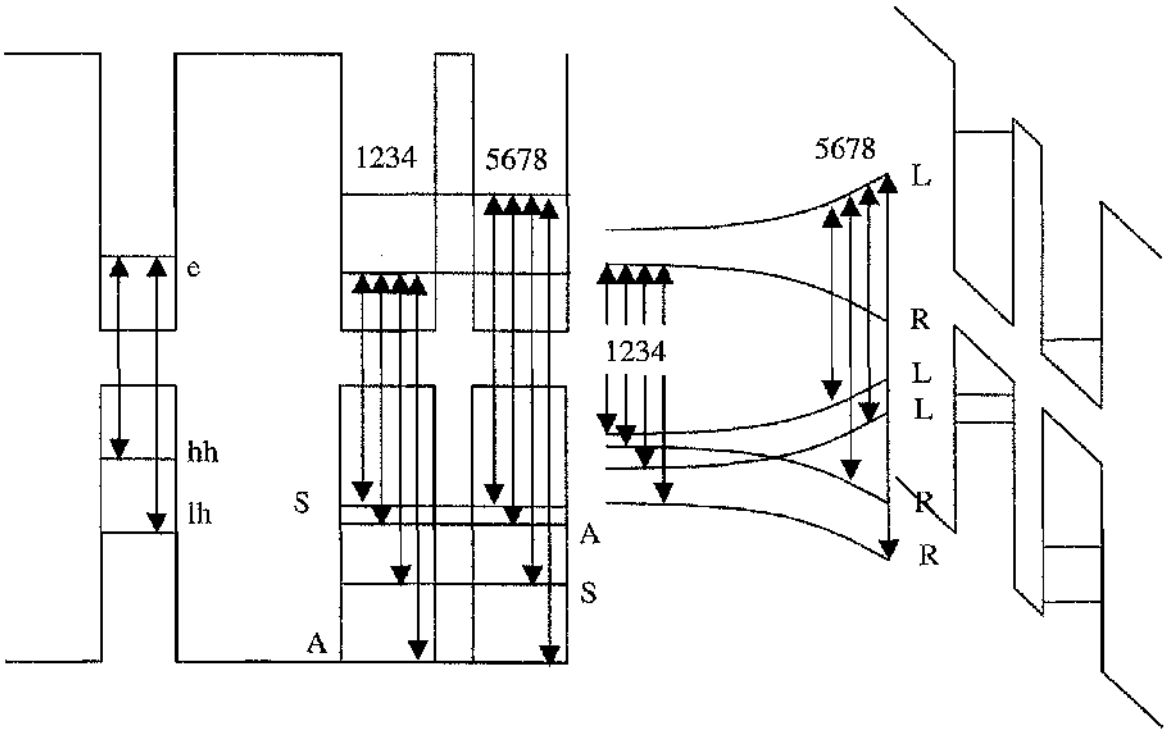

Fig. 6.5. The difference between single and coupled wells is illustrated in the diagram above. When the field is applied the coupling is destroyed.

The coupled well modulators previously designed and tested were active between 820 and 830 nm so this was chosen as the design centre wavelength of the mirror. The simulations performed with the Reflectance Analysis program indicated that a 20.5 period stack with 583 Å $Al_{0.15}Ga_{0.85}As$ and 713 Å AlAs would give a peak reflectance of 98.1% from 815 to 875 nm as shown in Fig. 6.6. The program used to design the DBR does not take into account the presence of the modulator stack. Previous designs which included MQW structures, showed a reflectance response which was shifted towards shorter wavelength. This design, although centred on 845 nm was thought close enough to be suitable for use behind a modulator structure consisting of 100 pairs of coupled wells. The wells were bound by 50 Å $Al_{0.3}Ga_{0.7}As$ barriers and were made from 50 Å GaAs. The barrier thickness on alternate barriers was reduced to 20 Å to provide the coupling between pairs of wells.

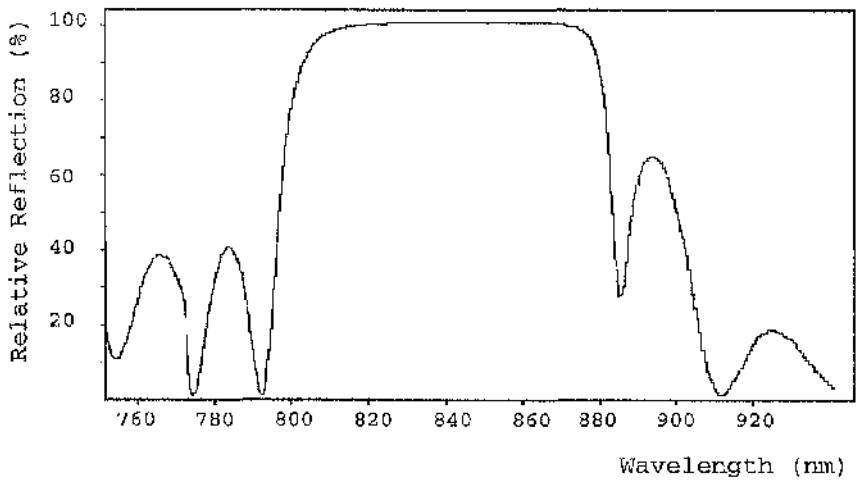

Fig. 6.6. Simulation of the reflectivity of the DBR stack described above.

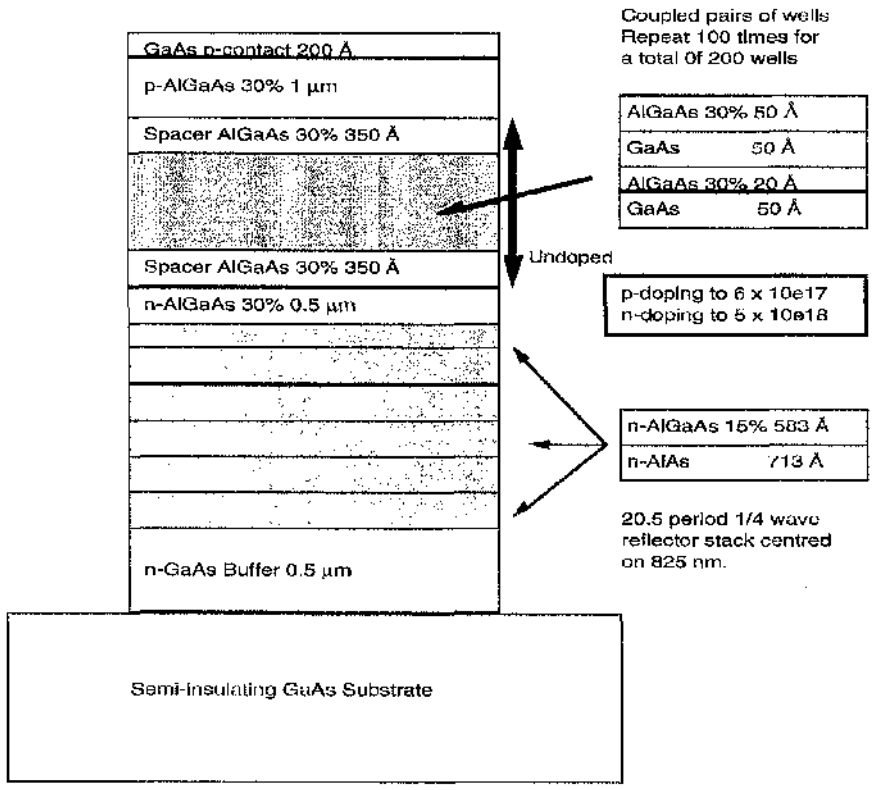

Fig. 6.7. The design for the reflective modulator used in this study.

The modulator has a p-i-n structure and so the reflector stack was grown on the substrate and n-doped. Consequently an undoped spacer layer is needed between the doped region and the well structure to prevent contamination of the wells. A 350 Å thick, undoped $Al_{0.3}Ga_{0.7}As$ layer was used for this purpose. The wells were then grown, followed by another spacer, a p-doped layer of $Al_{0.3}Ga_{0.7}As$ and a 200 Å p-doped GaAs

layer to provide the p contact. The complete layer structure is that shown above in Fig. 6.7.

The structure shown above was grown in a metal-organic vapour phase epitaxy (MOVPE) reactor by John Roberts at the SERC Facility for III-V Semiconductors at the University of Sheffield [107]. Material was grown on two substrates, one semi-insulating and the other an n-doped monitor so that basic characterisation could be carried out. Measurements carried out at Sheffield indicate that the mirror was realised with the correct design parameters, as indicated by the plot of reflectivity in Fig. 6.9. There has been very little shift due to the MQW stack but the pass band has been broadened slightly when compared to the simulation results.

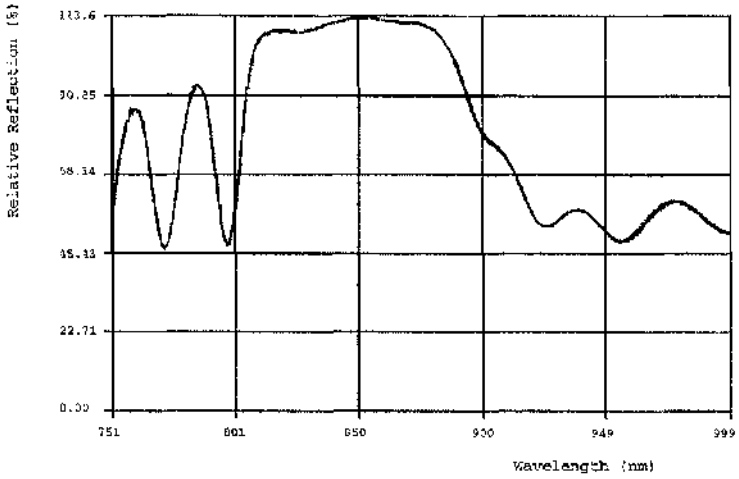

Fig. 6.9. Reflection measurement for the mirror with a peak reflectance at 847 nm. The reflectivity is still very good between 820 and 830 nm where the modulator is designed to operate. The 113% peak reflectivity is due to inaccurate calibration.

The metal pattern for the top contact consists of a 300 μm annulus with a 100 μm aperture for illumination. A 200 μm square pad extends from one side of the ring so that a reasonable bond-pad is available as shown in Fig.6.10. A mask set was designed and written for an array of such contacts and a mesa etch was incorporated in the design to isolate individual devices. The top contact is ohmic to p-type material and so 30 nm Au, 30 nm Zn and 30 nm Au films were deposited in a manual evaporator, (as Zn is not available in the Plassys evaporator.)

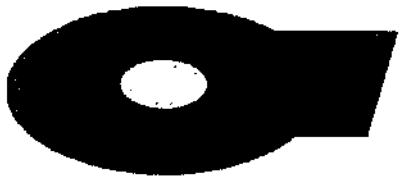

Fig. 6.10. The pattern used to make the ohmic contact metallisation to the top (p-side) of the modulator.

The ohmic contact to the back is achieved with an un-patterned mass contact using 10 nm Ni, 30 nm Ge and 80 nm Au. The recipes used for the contacts are based on the results of previous work in the Department to optimise contact performance [108]. Both contacts were then annealed in a single step at 350 °C for 60 seconds. The top side was then re-patterned with a protective film of photo-resist, which covered the contacts and exposed the surface to be etched in order to form the mesa isolation. The etch was done with the following:

$$1 \text{ part } H_2O \quad : \quad 8 \text{ parts } H_2O_2\,(30\%) \quad : \quad 1 \text{ part } H_2SO_4\,(98\%)$$

This is a vigorous etch and proceeds at a rate of about 20 to 25 μm per minute at room temperature. In order to isolate the devices, the mesa-etch needs to be not less than 3 μm deep. It is not a good idea to etch much more deeply as this wet etch is isotropic and considerable undercut would occur for a deep etch. The etch solution was floated in a bath of ice water to reduce the etch rate so that, after a 1 minute immersion followed by an immediate rinse in de-ionised water (D. I.), the mesa was measured to be 9 μm high using a Talystep surface profiler. Devices were fabricated on both types of substrate in the manner described above.

6.4 Modulator Test and Characterisation

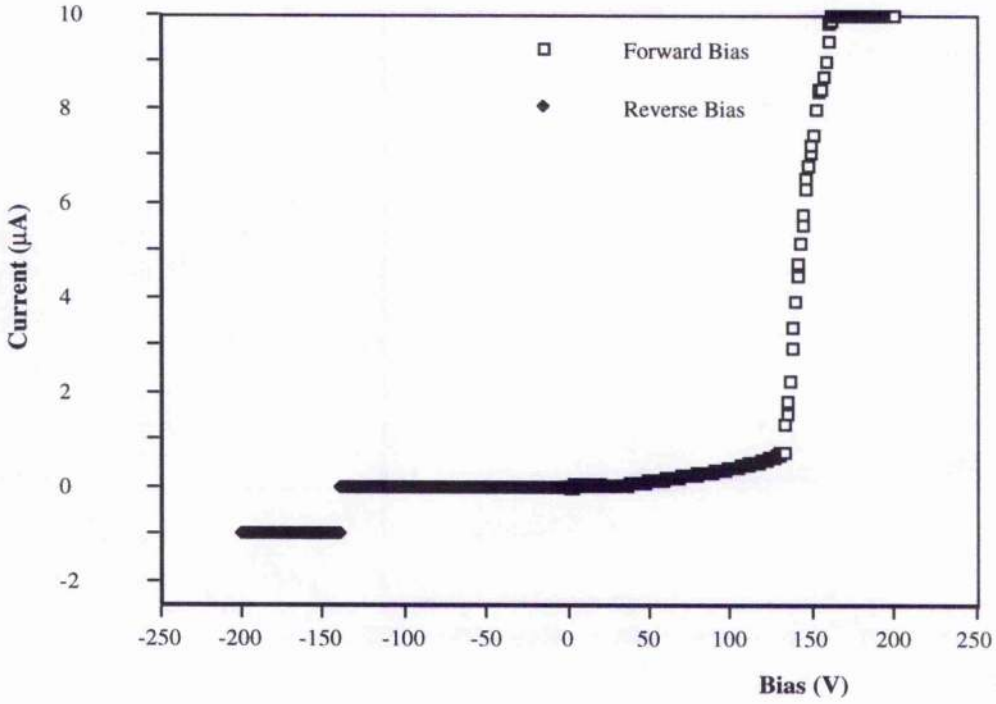

Fig. 6.11. The I-V curve for a device on a semi-insulating substrate.

The array was mounted on a test card and probed to determine the I-V and breakdown characteristics. As can be easily seen from Fig. 6.11, good ohmic contacts to semi-insulating material are difficult to achieve. The characteristic is dominated by the substrate. The behaviour of the devices on the doped substrate, however, exhibits the correct behaviour for a pin diode as shown in Fig. 6.12.

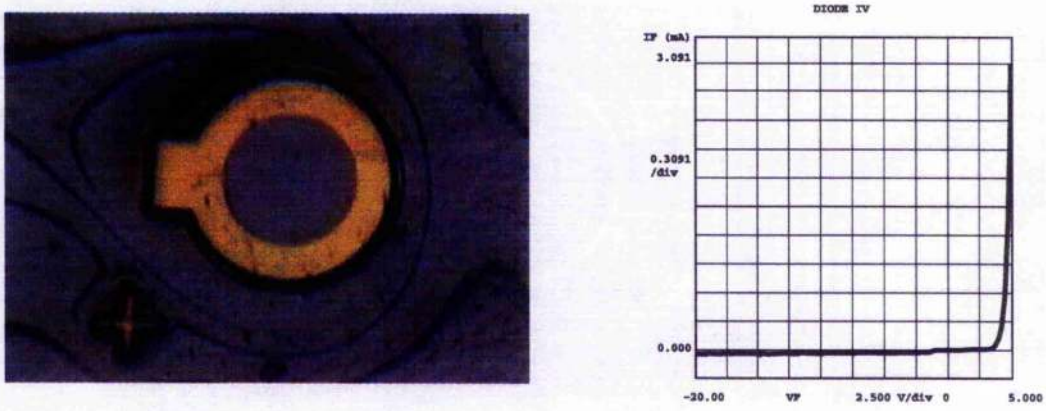

Fig. 6.12. Characteristic taken from the device grown on a doped substrate. On the left is a photograph of the modulator after the isolation etch has been carried out.

The modulators were then tested for their optical properties, using a Titanium Sapphire laser whose wavelength was tunable from 700 nm to 1μm. The crystal was pumped by an Argon ion laser and was capable of giving 0.5 W of continuous output power. The rest of the set-up, shown schematically in Fig. 6.13, consists of test and monitor beams which are split from the primary beams with 50% beam splitters.

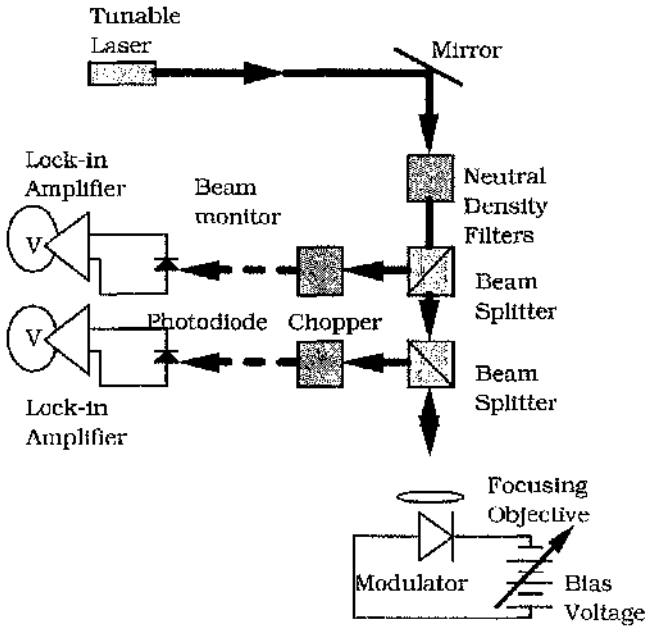

Fig. 6.13. The test set-up used for the optical characterisation of the modulators.

The standard method of obtaining precision measurements with a continuous beam is to chop the input light at a certain frequency and use a lock-in amplifier which has a very high rejection of any signals which do not contain components at the chopping frequency or its harmonics. Provided a suitable frequency is chosen (not 50 Hz), most of the background light and power supply ripple can be eliminated from the measurement. The monitor beam is required as the output power from the laser changes slightly as the laser is tuned and this needs to be accounted for when normalising the results.

The sample is correctly positioned and moved into the focal plane of the objective by placing a CCD attached to a monitor in front of the reflected beam after the splitter. The ring of the top metal can then be imaged and centred in the illuminating field. If this procedure is followed with the light tuned to the sensitive wavelength of the modulator, then the sample changes brightness as the applied voltage is changed. This is quite obvious on the monitor screen.

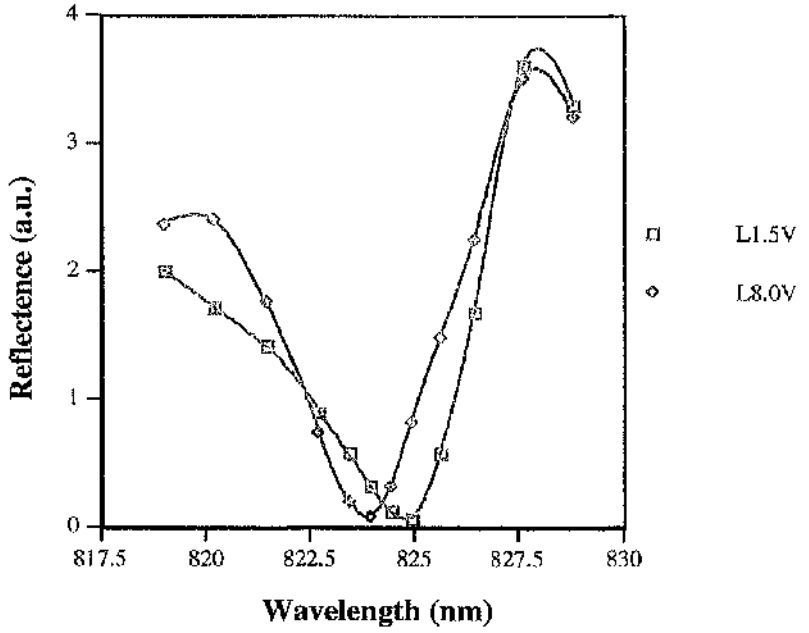

Fig. 6.14. The response of the modulator to applied bias. The shift at about 825 nm is where the largest modulation depth occurs.

When the set-up has been correctly adjusted, a series of scans of the incident laser wavelength is made for a range of applied bias voltages. Fig. 6.14 shows a red shift of about 1 nm in the absorption minimum at 825 nm for a bias of 8 V. A contrast ratio of 14, achieved for this device under the conditions shown, represents an 80% improvement on the performance of transmission modulators made with a similar design [109]. No blue shift was observed for low bias voltages.

The set-up was next modified slightly so that the modulator could be pulsed. The lock-in amplifier was replaced with a charge amplifier in an attempt to see if the electrical impulses modulating the laser beam could be reconstructed.

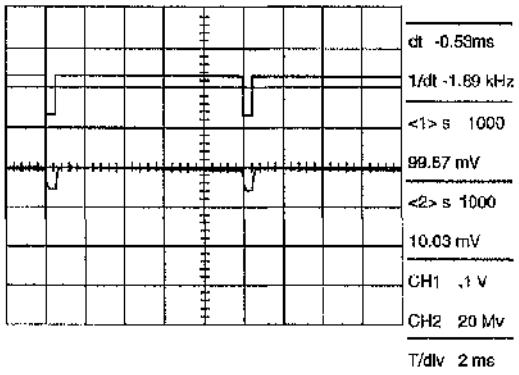

Fig. 6.15 Print out of the oscilloscope trace showing the input pulse to the modulator (upper trace) and the pulse decoded from the reflected laser beam (lower trace).

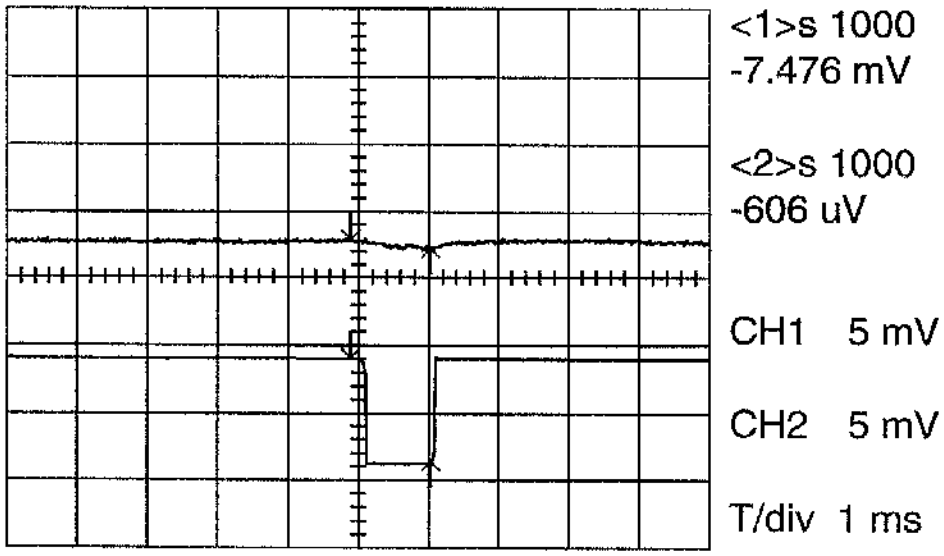

Fig. 6.16. A 7.5 mV drive signal on the modulator (lower trace) is visible on the decoded optical signal from the modulator (upper trace).

The traces shown in Figs. 6.15 and 16 show that the applied signal is easily decoded with the test set-up used. The same measurements were repeated as a function of the power of the incident optical beam to produce the graph shown in Fig. 6.17.

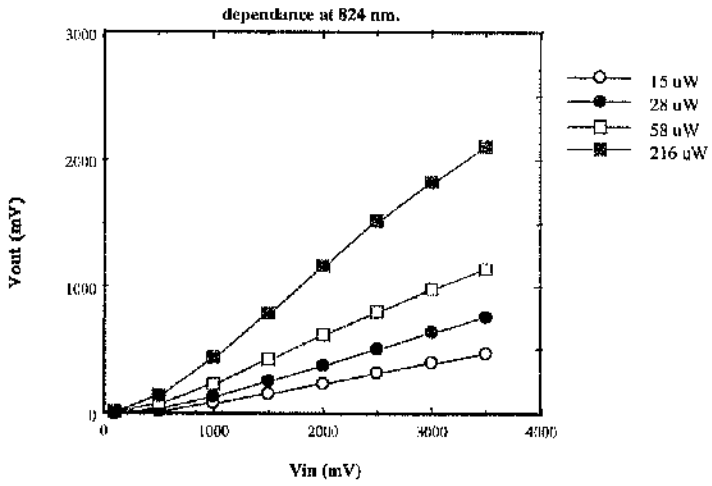

Fig. 6.17. The system response is linear from an input signal greater than 500 mV for a variety of laser powers.

The tests demonstrate that the modulators perform as expected. The drive voltage required by the devices permits the transmission of information with an amplitude of

some milli-volts and, at this level, would satisfy the drive criterion for a radiation detector read-out element. The modulator structure itself worked well at almost the same wavelength as the single pass modulators previously made by the Opto-electronics group in Glasgow. The inclusion of the mirror raised the contrast ratio from 8 (for a single pass) to 14, indicating that the mirror design has a reasonably high reflectivity and thus meets the design criteria.

All of the modulators fabricated on the semi-insulating substrates showed the same shape for reflectance at the same wavelength indicating the presence of the mirror and absorption from the modulator. Tests with biased samples showed, however, that there was no measurable change in the absorption when the bias was changed [110]. On close examination, it is seen that the absorption peak is broader than those seen on the working devices. The fact that there is no change in the absorption indicates that the wells are being screened from the applied bias by some space charge region.

The interface region between the substrate and epi-layer is the most likely source of this space charge. In devices which are fabricated on epi-material, the electronic function is contained within the grown layer – in addition a buffer layer is usually grown to provide a barrier against dislocation diffusion. The interface between the buffer layer and the substrate usually contains a high density of traps as the grown layer does not seamlessly grow from the whole available surface but from a large number of nucleation sites on the surface.

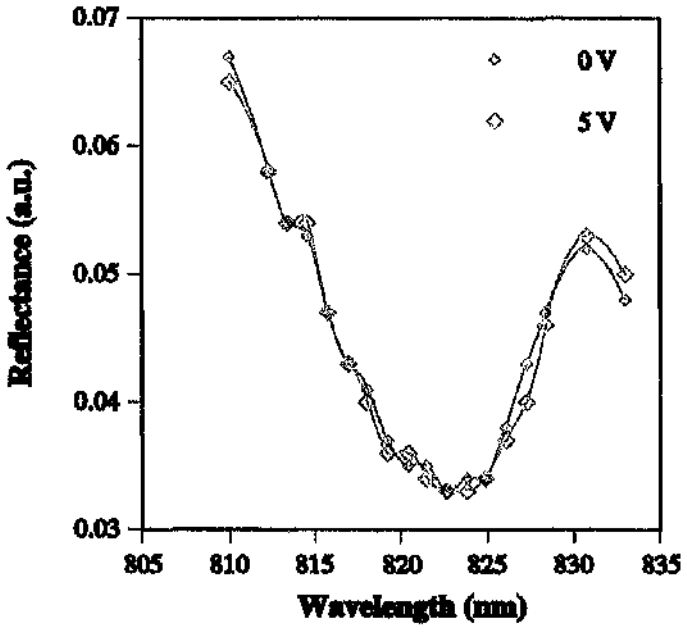

Fig. 6.18. The effect of changing the bias on a modulator made on a semi-insulating substrate. There is no absorption shift and the peak is much broader than that found on the doped substrate.

The fact that the modulator structures work on doped substrates means that this scheme could still be used to read out a detector which has been bump bonded to a modulator array. When these devices were fabricated, the only bonding process available, from GMMT, required a minimum pitch of 50 μm (the finished bond dimension is smaller but a larger surface area is required for metal deposition prior to reflow). The capacitance of a modulator element of this size would render it unsuitable as a read-out element for a radiation detector.

The recent results with indium bump bonding carried out by IMC indicate that a pitch of 15 μm might be possible. This would make another attempt with a modified modulator design an interesting proposition. This would require that the operating wavelength of the modulator be increased to around 950 nm so that the laser light can pass through the substrate material and the device operate with a mirror between the modulator and the detector.

Conclusion

The development of GaAs radiation detectors has still a long way to go in order to reach a performance comparable to that of silicon. The fact that any programme of development was established in the first place was entirely due to the perceived radiation hardness of the material/technology. It has always been true that there is no such thing as the universal detector and this is especially true in the area of X-ray detection. In the author's opinion, the use of GaAs for X-ray detection is reason enough to sustain its continued development, for example to have ~100% detection of X-rays up to 70 keV, for which a 500 μm thick active layer of GaAs would suffice, while several mm of Si is required. The estimate of the ratio of total cross-sections in Fig. 5.6 is much lower than that for the photoelectric cross-sections. As illustrated in Fig. 1, the value is closer to 30, taking into account 10 times more counts in the photopeak for a GaAs detector which is a third of the thickness of the silicon detector.

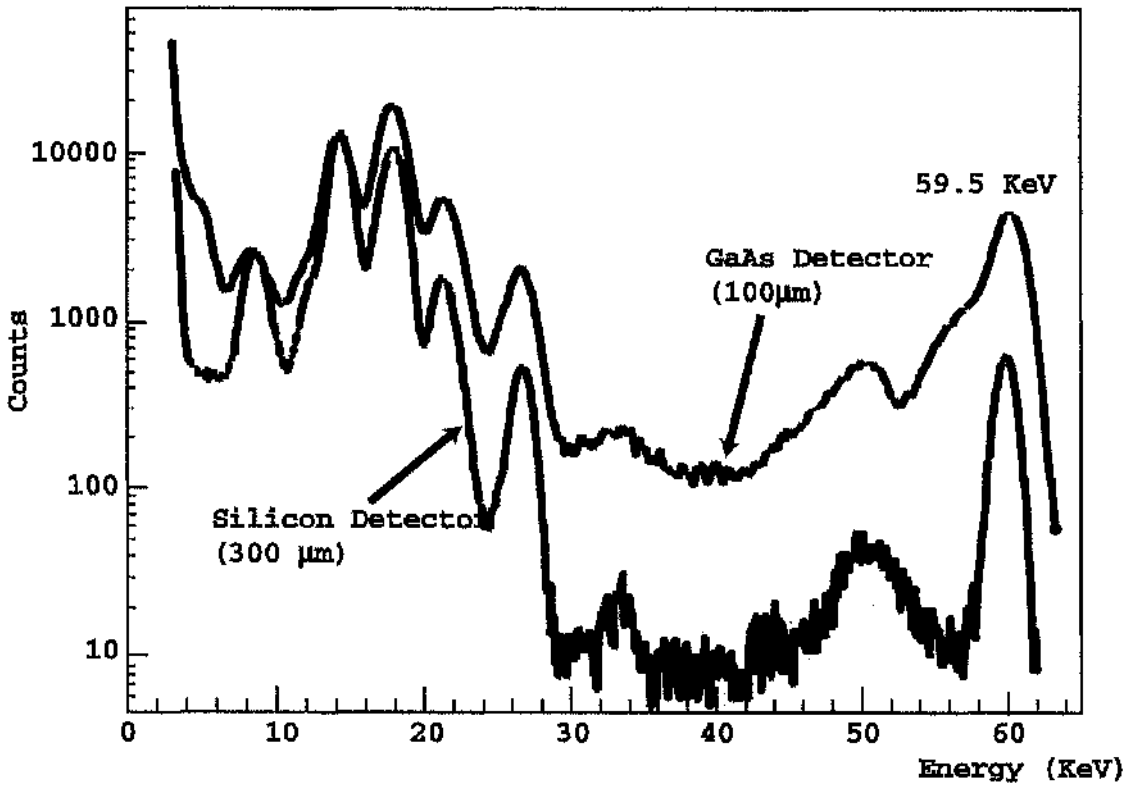

Fig.1. Overlaid Am^{241} spectra from a 300 μm thick Si diode and a 100 μm thick GaAs diode [22]. The diodes have been cooled to -30°C to reduce the noise due to the leakage current. The spectra have been normalised on the energy axis so that the peaks correspond and on the frequency axis so that the first peak (8 keV) has the same number of counts.

While the detectors developed for high energy physics performed to their design specification, the improvement of the radiation resistance of comparable silicon detectors has effectively relegated the further development of GaAs radiation detectors to other niche applications. The devices fabricated to investigate their performance as X-ray detectors are already pointing to possible improvements in the material that may be required before it could be classed as detector grade. The measurements with the small area charge integrating pixel detectors show evidence that the substrate material is highly irregular, with its detection properties varying considerably over a very localised area. This type of read-out could also be used to measure the thermally stimulated current (TSC) response for very localised areas and may have applications in the study of radiation damage effects in Si as well as in GaAs. Silicon detectors, compatible with the IMC read-out have already been designed and will be included in the mask-set for Medipix compatible detectors on silicon to be fabricated this summer.

The development of commercially viable methods of epitaxial growth may provide the most uniform material if the purity and thickness issues can be resolved. The most recent sample supplied from Aixtron plc. has an epi-layer thickness of about 50 μm and a free carrier concentration of about $1.5x10^{14}$ cm^{-3}. All the epi samples previously tested were unable to resolve signals from MIPs due to insufficient active thickness at the highest sustainable bias. As shown in Fig.2 devices produced with the most recent material easily resolve the signal and provide us with an independent method of measuring the active thickness of the detectors.

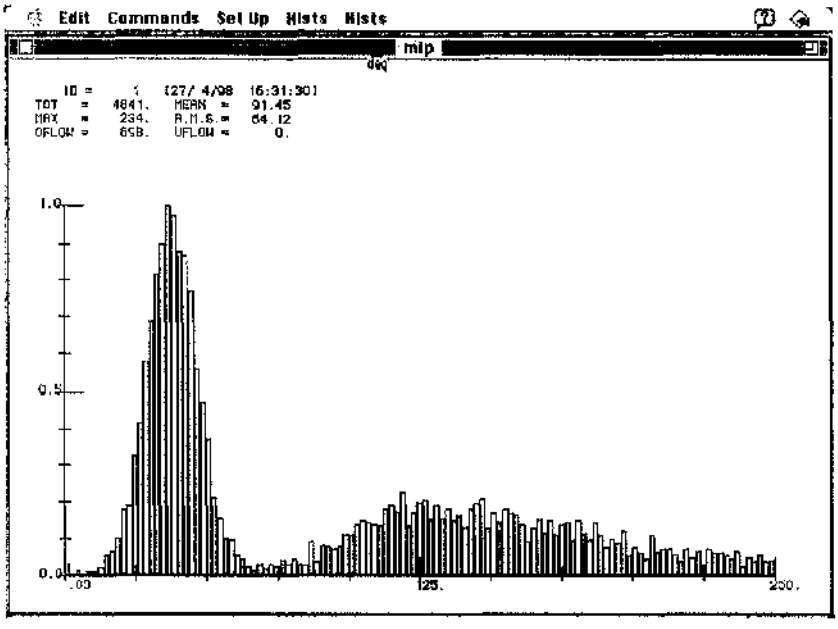

Fig. 2. A spectrum from a Sr^{90} beta source with a 3 mm diameter pad on a 50 μm thick layer of epitaxially grown GaAs. The data were taken at a temperature of - 20°C and a bias of 200 V with a 1.5 μs shaping time. The Landau peak is clearly resolved from the Gaussian noise pedestal.

The advent of true single photon counting read-out opens up a whole new world in imaging techniques. With sufficient stability and repeatability in X-ray tubes, it should be possible to operate them as line sources by windowing the threshold in successive exposures. The elimination of Compton scatter should provide images of unparalleled quality. Many applications involving, for example, experiments with Synchrotron radiation sources will benefit as a result. Initial tests of this type of application are scheduled at the Daresbury S.R.S. this summer.

There is renewed interest at CERN in the radiation hardness provided "free" by the migration to smaller design feature sizes. This trend towards deep sub-micron technologies will provide the designers of pixel electronics with much more freedom, as the new technologies provide simultaneously for the much denser designs which are critical when designing for pixel detectors.

Successful implementation on a 12.5 μm pitch of indium bump bonding means that optical modulator arrays with 9 fF/ pixel element could be made and bump bonded to an epitaxially grown thick detector. Modulators with a similar performance to those already described in this work would be perfectly adequately driven – 1 fC of charge (6250 electrons – 26 keV) produces 100 mV on 10 fF. Such an array of modulators would produce optical signals which could be remotely processed in a variety of ways, creating a wide range of new applications for pixel detectors.

References

[1] C. Kittel, *Quantum Theory of Solids*, Wiley, New York, 1963.

[2] J. R. Chelikowsky and M. L. Cohen, "Nonlocal Pseudopotential Calculations for the Electronic Structure of eleven Diamond and Zinc-Blende Semiconductors," *Phys. Rev.* **B14**, 556 (1976).

[3] C. D. Thurmond, "The Standard Thermodynamic Function of the Formation of Electrons and Holes in Ge, Si, GaAs and GaP," *J. Electrochem. Soc.*, **122**, 1133 (1975).

[4] R. A. Smith, *Semiconductors*, 2nd ed., Cambridge University Press, London, 1979.

[5] W. Shockley, "The Theory of p-n Junctions in Semiconductors and p-n Junction Transistors." *Bell Syst. Tech. J.*, 28, 435 (1949).

[6] W. Schottky, "Halbleitertheorie der Sperrschicht," *Naturwissenschaften* **26**, 843 (1938).

[7] S. M. Sze, "Physics of Semiconductor Devices," 2nd ed., John Wiley & Sons, New York, 1979.

[8] R. S. Muller, T. I. Kamins, "Device Electronics for Integrated Circuits," John Wiley & Sons, New York, 1977.

[9] E. H. Rhoderick, "Metal Semiconductor Contacts," Clarendon Press, Oxford, 1978.

[10] J. Millman, A. Grabel, "Microelectronics," 2nd ed., McGraw-Hill, Singapore, 1987.

[11] W. R. Leo, " Techniques for Nuclear and Particle Physics Experiments, Springer Verlag, 1987.

[12] S. Hancock et al, " Energy Loss and Energy Straggling of Protons and Pions in the Momentum Range 0.7 to 115 GeV/c" *Physical Review* A28(2), 1983.

[13] G. F. Knoll, " Radiation Detection and Measurement," 2nd ed., John Wiley & Sons, New York, 1989.

[14] S. P. Beaumont et al., " Charge transport properties of undoped SI LEC GaAs solid-state detectors," *Nucl. Instr. Meth.*, **A326,** (1993), 313.

[15] L. Landau, *J. Phys. (USSR)* **8**, p 201, 1944

[16] R. D. Evans, "The Atomic Nucleus," Kreiger, New York, 1982.

[18] V. Radeka, " Signal, noise and resolution in position sensitive detectors," IEEE *Trans. Nucl. Sci.*, **NS-21**, No. 1 (1974), 51.

[19] A. Van der Zeil, " Noise in measurements," John Wiley & Sons, New York, 1976.

[20] D. McGregor et al., IEEE *Trans. Nucl. Sci.*, **NS-43**, (1996), 1397.

[21] F. Nava et al., "Radiation Hardness of LEC Si GaAs detectors to proton irradiation," *Nucl. Instr. Meth.*, **A410**, (1998), to be published.

[22] Bertuccio G. et al., " Performance of SI GaAs detectors at 20°C and -30°C for X- and gamma-ray spectroscopy," *Nucl. Instr. Meth.*, A379, (1996), 152.

[23] Private Communication, F. Cindolo, Universita di Bologna.

[24] E. Heijne et al., " A low noise CMOS integrated signal processor for multielement particle detectors," *Proc. 14th European Solid State Circuits Conf.* (1988), Manchester, UK, (ESSIRC1988), p66.

[25] M. Turala et al., " A silicon inner tracker/vertex for the EAGLE spectrometer at the LHC," Eagle Internal note, **INDET-NO-004**, March 1992.

[26] P. Allport et al., " A low power VLSI multiplexed Amplifier for silicon strip detectors," *Nucl. Instr. Meth.*, **A273**, (1988), 630.

[27] G. Hall, "Ionisation energy losses of highly relativistic charged particles in thin Silicon layers", *Nucl. Instr. Meth.*, **A220**, (1984), 356-362.

[28] D. S. McGregor and J. Kammeraad, *Semiconductors and Semimetals*, Vol. **43**, (1995), 383-442.

[29] G. Lutz et al., " Low noise monolithic CMOS front end electronics," *Nucl. Instr. Meth.*, **A263**, (1988), 163.

[30] Private Communication, Armin Wagner, CERN.

[31] O. Toker et al., " Viking, a CMOS low noise monolithic 128 channel front end for Si strip read out," *Nucl. Instr. Meth.*, **A340**, (1994), 572.

[32] A. Zichichi, " Perspectives for a new detector at a future supercollider: The LAA project," Heavy Flavours and High Energy Collisions in the 1-100 TeV Range, edited by A. Ali and L. Cifarelli, Plenum Publishing Corp., 1989.

[33] M. Campbell et al., " Development of a pixel read out chip compatible with large area coverage," *Nucl. Instr. Meth.*, **A342**, (1994) 52.

[34] J. Franka et al., " Solder bump technology: present and future," *Semiconductor fabtech*, 289.

[35] D. Pedder, " Flip-chip solder bonding for advanced service structures," *Plessey research and technology, research review* 1989.

[36] F. Anghinolfi et al., " A 1006 element hybrid pixel detector with strobed binary output," IEEE *Trans. Nucl. Sci.*, **NS-39**, (1992), 654.

[37] L. Evans, " The Large Hadron Collider," CERN/AC-95-002.

[38] J. Andersson et al., " 320 x 240 pixel quantum well infrared photodetector (QWIP) array for thermal imaging: fabrication and evaluation," *Proc.* SPIE., vol. **3061**, 1997, 740.

[39] Wavemaker ver.X.7. Barnard Microsytems Ltd., 134 Crouch Hill, London N8 9DX, United Kingdom.

[40] Private communication, Scott M'Meekin, Electronics Division, Cardiff School of Engineering.

[41] Private communication, Paul Sellin, University of Surrey.

[42] Private communication, Lois Hobbs, University of Glasgow.

[43] D. Marder et al., " Noise in GaAs detectors after irradiation," *Nucl. Instr. Meth.*, **A395**, (1997) 141.

[44] Bergoz MacVee. Julien Bergoz, Thoiry, France.

[45] J. Eberhardt, *Appl. Phys. Lett.*, **17**, (1970), 427.

[46] A. Zichichi, " Report on the LAA project," Volume 5, CERN-LAA/88-02, 1988.

[47] National Micro-electronics Research Centre, Lee Maltings, Cork, Ireland.

[48] R. Bertin et al., " A preliminary study of GaAs solid state detectors for high energy physics," *Nucl. Instr. Meth.*, **A294**, (1990), 211.

[49] Particle Physics Data Book.

[50] M. Squillante et al., Semiconductors and semimetals, Vol. **43**, (1995), 470.

[51] E. Heijne, " Muon flux measurements with silicon detectors in the CERN neutrino beams," CERN-EF/83-06 1983.

[52] S. Beaumont et al., " Gallium arsenide charged particle detectors: trapping effects," *Nucl. Instr. Meth.* **A342**, (1994), 83.

[53] K. Berwick et al., *MRS Proc.* 302, (1993), 363.

[54] S. Manolopoulos, PhD. Thesis, University of Sheffield, 1997, RAL-TH-97-006.

[55] T. Kubicki et al., " Calculation of the electric field in GaAs particle detectors," *Nucl. Instr. Meth.*, **A345**, (1994), 468.

[56] D. M°Gregor et al., IEEE *Trans. Nucl. Sci.*, **NS-39**, (1992), 1226.

[57] D. M°Gregor et al., " Present status of undoped semi-insulating LEC bulk GaAs as a radiation spectrometer," *Nucl. Instr. Meth.* **A343**, (1994), 527.

[58] GMMT plc., Caswell, Towchester, Northants NN12 8EQ.

[59] Micron Semiconductor Ltd., Lancing.

[60] G. Hallewell et al., " The Atlas Silicon Inner Tracker and Vertex Detector: Design Considerations and Related Technologies," ATLAS internal note **INDET-NO-014**.

[61] M. Alietti et al., "Performance of a new ohmic contact for GaAs particle detectors," *Nucl. Instr. Meth.*, **A362**, (1995), 344.

[62] S. P. Beaumont et al., " First results from GaAs double-sided detectors," *Nucl. Instr. Meth.*, **A348**, (1994), 514.

[63] Alenia S.p.A., Direzione Ricerca, Via Tiburtina Km 12.400, I-00131 Roma, Italy.

[64] R. Brenner et al., " Measurement of the spatial resolution of double-sided double metal AC-coupled silicon microstrip detectors," *Nucl. Instr. Meth.*, **A326**, (1993), 189.

[65] Stephen Gowdy, PhD. Thesis, University of Glasgow, 1996.

[66] I. Kipnis et al., "An Analog Front-End Bipolar-Transistor Integrated Circuit for the SDC Silicon Tracker," IEEE *Trans. Nucl. Sci.*, **NS-41/4**, (1994), 1095.

[67] J. DeWitt, "A pipeline and bus interface chip for silicon strip detector read-out, IEEE Nuclear Science Symposium, San Francisco CA, Nov. 1993, SCIPP 93/37.

[68] J. DeWitt, "The Header Adder Chip". SCIPP Preprint.

[69] J. Ludwig et al.,"Test beam results of GaAs strip detectors," *Nucl. Instr. Meth.*, **A410**, (1998), to be published.

[70] P. Allport et al., " ATLAS silicon strip beam test results," 2nd. Intern. Symp. On Development and Application of Semiconductor Tracking Detectors, Hiroshima, Japan, Oct. 10-13, 1995.

[71] Thilo Schmid, PhD. Thesis, University of Freiberg, 1996.

[72] M. Edwards et al., " The Radiation Hardness Test Facility." Rutherford Appleton Laboratory, Technical Report RAL-90-065, 1990.

[73] S. Beaumont et al., " GaAs solid state detectors for particle physics," *Nucl. Instr. Meth.*, **A322**, (1992), 472.

[74] S. P. Beaumont et al., " GaAs solid state detectors for physics at the LHC," IEEE *Trans. Nucl. Sci.*, Vol **40**, No. 5, 1993.

[75] Thierry Mouthey, "Radiation dose expected in the LHC inner detectors," Eagle internal note, **INDET-NO-012**, July 1992.

[76] A. Chilingarov et al., "Radiation damage due to NEIL In GaAs particle detectors," *Nucl. Instr. Meth.*, **A395**, (1997), 35.

[77] M. Rogalla et al., "Radiation studies for GaAs in the ATLAS inner detector," *Nucl. Instr.Meth.*, **A395**, (1997), 45.

[78] D. J. Warner et al., " Flip chip bonded GaAs MMICs compatible with foundry manufacture," *IEE Proceedings-H*, **Vol. 138**, No. 1, February 1991.

[79] E. Heijne et al., " LHC1: A semiconductor pixel detector read-out chip with internal, tunable delay providing a binary pattern of selected events," *Nucl. Instr. Meth.*, **A383**, (1996), 55.

[80] Private communication, Giles Humpston, GMMT Caswell.

[81] E. Heijne et al., " First operation of a 72k element hybrid silicon micropattern pixel detector array," *Nucl. Instr. Meth.* **A349**, (1994), 138.

[82] S. Gowdy, PhD. Thesis, University of Glasgow 1996.

[83] H. Hirayama et al., " The EGS4 System Code," SLAC Report 265, 1985.

[84] D. Heidtmann et al., " CCDs propel medical diagnosis into digital format," *Laser Focus World*, Biomedical Imaging, 1991.

[85] U. Welander et al., " Absolute measures of image quality for the Sens-A-Ray direct digital intraoral radiography system," *Oral and maxillofacial radiology*, Vol **80**, No. 3, 1995.

[86] Brite Euram Project XIMAGE, New X-ray imaging sensors, Proposal No. BE-1042.

[87] F. Yin et al., " Measurement of the pre-sampling modulation transfer function of film digitizers using a curve fitting technique," *Med. Phys.* **Vol. 17**, 1990, 962.

[88] U. Welander et al., " Resolution as defined by line spread and modulation transfer functions for four intraoral radiographic systems," *Oral and maxillofacial radiology*, **Vol 78**, No. 1, 1994.

[89] M. Campbell et al., " Read out for a pixel matrix with 15-bit single photon counting," submitted to the IEEE Nuclear Science Symposium, Albuquerque, New Mexico, 1997.

[90] C. Da Via', PhD. Thesis, University of Glasgow, 1997.

[91] Private communication, Michael Campbell, CERN.

[92] Private communication, Ubaldo Bottigli, CERN.

[93] IMC – Industrial Microelectronics Center, P. O. Electrum 233, S-164 40 Kista, Sweden.

[94] R. Irsigler et al., " X-ray imaging with GaAs pixel detectors and a ROIC," submitted to IEEE Nuclear Science Symposium in Toronto Nov. 1998.

[95] K. Gruter et al., " Deposition of high quality GaAs filmsat fast rates in the LP-CVD system," J. Crystal Growth **94** (1989) 607.

[96] Epitronics Corporation, 20012 North 19th Avenue, Phoenix AZ 85207, USA.

[97] R. Adams, "Growth of high purity GaAs using low-pressure vapour-phase epitaxy," *Nucl. Instr. Meth.*, **A395** (1997) 125.

[98] R. Adams et al., "Preliminary results for LP-VPE X-ray detectors," ," *Nucl. Instr. Meth.*, **A395** (1997) 129.

[99] J. Marsh, " Optically sampled gallium arsenide particle detectors," in : GaAs Detectors and Electronics for High Energy Physics, eds. C. del Papa, P. G. Pelfer, and K. Smith, World Scientific, Singapore, 1992.

[100] K. M'Ilvaney et al., " Evaluation of MQW structures for use in spatial light modulators," Proc. Gallium Arsenide and Related Compounds, 1990, Jersey, Channel Islands, pp 621-626.

[101] M. S. Robertson, " Fabrication of Two Dimensional Arrays of Surface Emitting Lasers," M.Sc. Thesis, University of Glasgow, 1990.

[102] W. Franz, *Z. Naturforsch*, Number 13a, p 484, 1958.

[103] L. V. Keldysh, "Behaviour of Non-metallic Crystals in Strong Electric Fields," *Soviet Physics JETP*, **Vol. 6**, Number 33, p 763, 1958.

[104] Miller D. A. B. et al., " Electric Field Dependence of Optical Absorption near the Band Gap of Quantum Well Structures," *Phys. Rev. B.*, **32**, p 1043, 1985.

[105] C. Button et al., "Matrix-addressed 4X4 spatial light modulator using the quantum confined stark effect in GaAas/AlGaAs quantum wells," *Electronic Letters*, **Vol. 26**, No. 20, (1990), 1691.

[106] J. Bleuse et al., *Phys. Rev. Lett.*, **60**, p 220, 1988.

[107] J. S. Roberts et al., " MOVPE grown multiple quantum well pin diodes for electro-optic modulators and photodiodes with enhanced electron ionisation coefficient," *Journal of Crystal Growth*, Vol. **93**, p 877, 1988.

[108] Private communication, Karen M°Ilvaney, Dept. of Electronics and Electrical Engineering, University of Glasgow.

[109] K. M°Ilvaney, "Fabrication and Assessment of GaAs/AlGaAs Multiple Quantum Well Optical Modulators," PhD Thesis, University of Glasgow, 1990.

[110] S. D'Auria et al., " MQW Modulators for X-ray Imaging," Presented at 4th International Workshop on Gallium Arsenide and Related Compounds, San Miniato, Italy, 19-21 Mar 1995.

[111] RD-2 collaboration, Status report, CERN/DRDC 93-18 RD2.

[112] M. Rogalla et al., "Radiation studies for GaAs in the ATLAS inner detector," *Nucl. Instr. Meth.*, **A395** (1997) 45.

[113] R. Worner et al., "Electron spin resonance of AsGa antisite defects in fast neutron irradiated GaAs," *Appl. Phys. Lett.* **40**(2), 1982, 141.

[114] A. Chilingarov et al., "Radiation damage due to NIEL in GaAs particle detectors," *Nucl. Instr. Meth.*, **A395** (1997) 35.

[115] H. Bischel, "Straggling in thin silicon detectors," *Review of Modern Physics*, **Vol. 60**, No. 3, July 1988, 663.

[116] S. D'Auria et al., "Gallium arsenide for vertex detectors", *Nucl. Instr. Meth.*, **A386** (1997) 177.

[117] "Imperfections in III/V Materials," *Semiconductors and Semimetals*, Volume Editor Eicke R. Weber, **Vol. 38**, 1993, 91.

[118] P. J. Sellin et al., " Punch through biasing structures for gallium arsenide microstrip detectors," Proc. 3rd Int. Workshop on GaAs and related compounds, World Scientific, Singapore (1996), 41.

[119] Private Communication, P. W. Phillips, Rutherford Appleton Laboratories.

[120] G. Anelli et al., " Total dose behaviour of sub-micron and deep sub-micron CMOS technologies," CERN/LHCC 97-60, 139.

Author's publications relevant to the thesis

1) NEW RESULTS ON GAAS SOLID-STATE DETECTORS FOR HIGH-ENERGY PHYSICS
By C. Del Papa et al., C90-05-28.1. 1990.
In *San Miniato 1990, Experimental apparatus for high energy particle physics and astrophysics* 200-208. (3714217)

2) PRELIMINARY RESULTS FOR LP VPE X-RAY DETECTORS
By R. Adams et al.,
Nucl. Instrum. Meth., A395 (1997) 129-131. (3628051)

3) RADIATION INDUCED DAMAGE IN GAAS PARTICLE DETECTORS
By R. Bates et al.,
IEEE Trans. Nucl. Sci. 44 (1997) 1705-1707. (3638774)

4) RECENT RESULTS ON GAAS DETECTORS - 137
By RD8 Collaboration (R.L. Bates et al.).
Nucl. Instrum. Meth., A392 (1997) 269-273. (3628051)

5) THE EFFECTS OF RADIATION ON GALLIUM ARSENIDE RADIATION DETECTORS
By RD8 Collaboration (R.L. Bates et al.).
Nucl. Instrum. Meth., A395 (1997) 54-59. (3628043)

6) GALLIUM ARSENIDE SOLID STATE DETECTORS FOR HIGH-ENERGY PHYSICS
By C. Del Papa et al., C89-10-17. 1989.
In *Erice 1989, Proceedings, Perspectives for new detectors in future supercolliders* 37-42. (3623335)

7) CHARACTERIZATION OF LOW PRESSURE VPE GAAS DIODES BEFORE AND AFTER 24-GEV/C PROTON IRRADIATION
By R. Bates et al.,
Nucl.Instrum. Meth., A410,1998.

8) TESTS OF GAAS DETECTORS FOR MINIMUM IONIZING PARTICLES IN A HIGH RADIATION ENVIRONMENT
By D.H. Saxon et al., C90-10-15. 1990.
In *Fort Worth 1990, Proceedings, Detector research and development for the Superconducting Super Collider* 169-172. (3583082)

9) MODEL OF CHARGE TRANSPORT IN SEMIINSULATING UNDOPED GAAS MICROSTRIP DETECTORS
By R. Bates et al., GLAS-PPE-95-05. C95-03-21.3. Sep 1995. 11pp. Talk given at 4th International Workshop on Gallium Arsenide and Related Compounds, San Miniato, Italy, 19-21 Mar 1995.
In *San Miniato 1995, Gallium arsenide and related compounds* 92-104..

10) NOISE SPECTRA OF SIU GAAS PAD DETECTORS WITH GUARD RINGS
By RD8 collaboration (R.L. Bates et al.).
GLAS-PPE-95-06. C95-03-21.3. Sep 1995. 10pp. Presented at Workshop on GaAs Detectors, San Miniato, Italy, Mar 19-21, 1995.

In *San Miniato 1995, Gallium arsenide and related compounds* 105-113..

11) GAAS MICROSTRIP TEST BEAM RESULTS

By S.J. Gowdy et al., GLAS-PPE-95-04. C95-03-21.3. Sep 1995. 9pp. Presented at 4th International Workshop on Gallium Arsenide and Related Compounds, San Miniato, Italy, 19-21 Mar 1995.

In *San Miniato 1995, Gallium arsenide and related compounds* 33-40..

12) GAAS SOLID STATE DETECTORS FOR HIGH-ENERGY PHYSICS

By RD8 Collaboration. (C. Buttar et al.).

1992.

In *Dallas 1992, Proceedings, High energy physics, vol. 2* 1709-1713.

(3140318)

13) RD19: STATUS REPORT ON 1994 DEVELOPMENT OF HYBRID AND MONOLITHIC SILICON MICROPATTERN DETECTORS

By RD19 Collaboration (Erik H.M. Heijne et al.).

CERN-DRDC-94-51. CERN-RD-19-STATUS-REPORT-1994. Jan 1995. 22pp. (3086313)

14) GALLIUM ARSENIDE CHARGED PARTICLE DETECTORS: TRAPPING EFFECTS

By RD8 Collaboration. (S.P. Beaumont et al.).

Nucl. Instrum. Meth., A342 (1994) 83-89. (3061582)

15) TEST BEAM RESULTS FROM PROTOTYPES FOR THE UPGRADED ALEPH VERTEX DETECTOR

By G. Bagliesi et al., 13pp. Talk given at 6th Pisa Meeting on Advanced Detectors: Frontier Detectors for Frontier Physics, La Biodola, Elba, Italy, 22-28 May 1994.

16) GAAS SOLID STATE DETECTORS FOR PHYSICS AT THE LHC

By S.P. Beaumont et al.,

IEEE Trans. Nucl. Sci. 40 (1993) 1225-1230. (2995336)

17) CHARGE TRANSPORT PROPERTIES OF UNDOPED SI LEC GAAS SOLID STATE DETECTORS

By S.P. Beaumont et al.,

Nucl. Instrum. Meth., A326 (1993) 313-318. . (2878186)

18) GAAS SOLID STATE DETECTORS FOR PARTICLE PHYSICS

By S.P. Beaumont et al.,

Nucl. Instrum. Meth., A322 (1992) 472-482. . (2760177)

19) GALLIUM ARSENIDE MICROSTRIP DETECTORS FOR CHARGED PARTICLES

By RD8 Collaboration (S.P. Beaumont et al.).

Nucl.Instrum. Meth., A321:172-179,1992. (2553090)

20) A PRELIMINARY STUDY OF GAAS SOLID STATE DETECTORS FOR HIGH-ENERGY PHYSICS

By R. Bertin et al.,

Nucl.Instrum. Meth., A294:211-218,1990. (2176432)

21) MEASUREMENT OF HIGH-INTENSITY PROTON BEAM PROFILE WITH A GaAs SIU SURFACE BARRIER DETECTOR
By R. Bates et al.,
Nucl.Instrum. Meth., A395,1997, 26-28.

22) FIRST RESULTS FROM GaAs DOUBLE-SIDED DETECTORS.
By S.P. Beaumont et al.,
Nucl.Instrum.Meth., A348,1994, 514-517.

23) RECENT RESULTS ON GaAs DETCTORS
By R. Bates et al.,
Nucl.Instrum. Meth., A392,1997.

24) MICRO-INHOMOGENEITY EFFECTS AND RADIATION DAMAGE IN SEMI-INSULATING GaAs RADIATION DETECTORS
By R. Bates et al.,
To be published in IEEE Trans. Nucl. Sci.

25) DEVELOPMENTS IN GaAs PIXEL DETECTORS FOR X-RAY IMAGING
By R. Bates et al.,
To be published in IEEE Trans. Nucl. Sci.

26) GALLIUM ARSENIDE MICROSTRIP DETECTORS AND PIXEL DETECTOR DEVELOPEMENTS
By R. Bates et al.,
IEEE Trans. Nucl. Sci. Vol 43, No. 3, 1996

27) GaAs FOR VERTEX DETECTORS
By R. Bates et al.,
Nucl.Instrum.Meth.A395,1990, 26-28. (2176432)

28) MEASUREMENT OF HIGH-INTENSITY PROTON BEAM PROFILE WITH A GaAs SIU SURFACE BARRIER DETECTOR
By R. Bates et al.,
Nucl.Instrum.Meth., A386, 1997.

29) GALLIUM ARSENIDE PIXEL DETECTORS FOR MEDICAL IMAGING
By R. Bates et al.,
Nucl.Instrum.Meth.A395,1997, 148-151.

30) USE OF SILICON AND GaAs PIXEL DETECTORS FOR DIGITAL AUTORADIOGRAPHY
By S.R. Amendolia et al,
IEEE Trans. Nucl. Sci. : 44 (3) (1-2) (1997) (929-938).

31) SOME NEW RESULTS ON SEMI-INSULATING GaAs DETECTORS FOR LOW ENERGY X-RAYS.
By W. Bencivelli et al.,
Nucl. Instrum. Meth. A355, (1995) 425-427.

Properties of GaAs, Ge and Si.

Property	*Symbol*	*Units*	*GaAs*	*Ge*	*Si*
Crystal Structure			Zincblende	Diamond	Diamond
Atoms per unit cell			8	8	8
Atomic Number	Z		31/33	32	14
Atomic or Molecular Weight	MW	g/g-mole	144.64	72.59	28.09
Lattice constant	a_o	nm	0.56532	0.56575	0.54307
Density		g cm^{-3}	5.316	5.323	2.328
Energy gap at 300 K	E_g	eV	1.42	0.67	1.124
Relative permittivity	ε_r		13.1	16.0	11.7
Refractive index	η		3.3	3.97	3.44
Melting point	T_m	°C	1237	937	1412
Intrinsic carrier conc.	ni	cm^{-3}	9.0×10^{6}	2.4×10^{13}	1.45×10^{10}
Electron mobility	μ_n	cm^2(Vs)$^{-1}$	8800	3900	1417
Hole mobility	μ_p	cm^2(Vs)$^{-1}$	400	1900	471
Electron affinity	$q\chi$	eV	4.07	4.00	4.05